Characterization of Transport Processes in Packed Fuel Beds for Wildfire Applications

Master of Science Thesis

Juan Pablo Martínez

October, 2025

Faculty of Engineering and Sciences, Universidad Adolfo Ibáñez

Characterization of Transport Processes in Packed Fuel Beds for Wildfire Applications

A thesis submitted for the degree of

Magíster en Ciencias de la Ingeniería

by

Juan Pablo José Martínez Ormazábal

This thesis has been supervised by

Prof Pedro Reszka

The examining committee was integrated by

Prof María Thomsen

Prof Gilles Parent

Abstract

Wildfires have been a threat to human life throughout history, but have become an even more tangible danger due to climate change. Occurrence of these climatological phenomena are present worldwide every year, as increasingly more frequent heat waves and droughts not only favor fire spread but also lead to the destruction of habitats, human life, and wildlife.

In the present work, various physical scenarios were studied to determine, though scientific approaches, the intrinsic characteristics of porous fuels in the context of wildfires and their relevance to this research area. By proposing a characterization of transport processes for this purpose, the study ensures that the retrieved properties were obtained under specific experimental designs and theoretical frameworks, allowing the verification of both the accuracy of the values and their ability to represent the actual physical phenomena under the given constraints and conditions. The investigation focused mainly in fluid flow mechanics and radiative transport in packed fuel beds of elongated artificial wood elements and *Pinus radiata* pine needles, a common wildland fuel that is widely found in forests of Chile and California.

The findings suggest, on the fluid transport part, that permeability of highly porous fuel beds (greater than 89% porosity) at considerable masses from $50 - 170\,\mathrm{g}$ under vertical positions in an acrylic wind tunnel in Forchheimer regimes are both in the order of $10^{-7}\,\mathrm{m}^2$ for pine needles and for wood elements, specifically in the range of $2{,}47 - 4{,}95 \cdot 10^{-7}\,\mathrm{m}^2$ for pine needle fuel beds and $1{,}33 - 1{,}76 \cdot 10^{-7}\,\mathrm{m}^2$ for wood element fuel beds. From these specimens, characteristics of surface to volume ratio were $7.100\,\mathrm{m}^{-1}$ for live pine, $14.418\,\mathrm{m}^{-1}$ for dead and dry pine, $2.008\,\mathrm{m}^{-1}$ and $1.341{,}33\,\mathrm{m}^{-1}$ for both kinds of elongated wood elements. Stemming from these qualities, reflectivity for dead and dry pine needle samples in small fuel beds were $10 - 15\,\%$ in visible spectrum, maximum of $35\,\%$ at mid infrared and lowest in far infrared at $2 - 9\,\%$, whereas for diffuse and direct transmissivity went from 40% to 10% and from 37% to 1%, respectively. Only from direct transmissivity, absorption coefficient ranged between 388,35 − 299,97 m^{-1}, with a mean free path of radiation of 0,0033 − 0,0026 m. Absorption coefficients where also attained with the Bouguer-Beer-Lambert Law and with the geometric optics approach (i.e. $\kappa_\lambda = 1/4 \cdot \sigma\beta$), where from least densely packed at 90% porosity up to 10%, for wood results were 38 − 758 m^{-1} and 37 − 807 m^{-1}, whereas for pine from 90% to 50% were 24 − 173 m^{-1}.

On thermal analyses solely made for dead and dry pine needle fuel beds, specific heat from a microcalorimeter gave results from 20 °C to 60 °C values of 1,550 − 2,014 kJ kg^{-1} K^{-1}, with an average for all five values of 1,761, kJ kg^{-1} K^{-1}. Thermal inertia from a semi-infinite model with slight increases of temperature starting from ambient temperature determined a value of 88,11 W K^{-1} m^{-2} $s^{1/2}$, this result conjoined with the specific heat of 1,550 kJ kg^{-1} K^{-1} gave a conductivity of pine needle fuel bed with natural porosity of 0,074 W m^{-1} K^{-1}. Lastly, in-depth temperature distributions from radiation at 4 kW m^{-2} from a cone calorimeter towards the inside of pine needle fuel bed yielded after nearly three hours long experiments transition from transient to fully stationary temperature distributions at all measured depths (from 5 mm to 50 mm). Based on this and on an ignition and mass loss rate experiment for this same fuel bed, fuel properties were analyzed in these scenarios as transient and stationary one dimensional problem solving, where for a more extreme layout of ignition at 40 kW m^{-2}, thermal inertia increased nearly five times up to 428,84 W K^{-1} m^{-2} $s^{1/2}$, whereas from steady state at 4 kW m^{-2} the absorption coefficient resulted in a value of 54,5 m^{-1} in the temperature distribution resulting from the differential equation.

All results demonstrate that specific bench-scale experiments accurately characterize relevant fuel beds in the context of fire science, supporting further studies and modeling efforts aimed at improving the understanding of fire propagation and advancing fire safety.

Keywords: Porous fuels; radiative transfer; permeability; absorption coefficient.

Acknowledgments

First and foremost, I would like to express my sincere gratitude to my supervisor, Dr. Pedro Reszka, for his constant guidance through my stumbles and endless questions, for his rigor and dedication in always pushing my work to a highest possible standard, and for his kindness and support throughout this long journey, I have the heartiest gratitude to him, because everything good I will do with my career in the future I will owe a core part of it to him.

I must also thank Professor María Thomsen for all extra help and advice in my project and of course all my colleagues at the Combustion Lab, especially those who helped me at the beginning of this challenging path: Nicolás Correa for his unwavering willingness to help me through doubts and difficult moments; Joaquín Ferrer for his good companionship and down to earth talks; Antonia Urbina for making every day brighter with her kindness; Francisco Valenzuela for his spot on advice and humor; and Lucas Fernández for his friendship. I would also like to thank everyone at the Équipe Feux at LEMTA for the time I spent working there, it was a dream come true to immerse myself in such a beautiful country and to work with an even better team. I am especially grateful to Professors Gilles Parent and Zoubir Acem for being not only outstanding professionals but also exceptional people.

The financial support is partially due to ANID FONDECYT regular 1230595 for all the equipment in my research done in Chile, also Universidad Adolfo Ibáñez for supporting my trip to the 10th School on Combustion in Brazil, and Institut Français du Chili for enabling me to research in France with a very generous scholarship and for the french lessons before this trip, I never expected to learn a third language in my research!

On a more personal regard, I would like to thank my family, particularly my parents, Ximena and Francisco, for giving me the best gift besides love: education. I will always value your sacrifices, and you have taught me that all intangible goods are the greatest in life, I will be forever grateful to you, mom and dad. I have always thought how my love for science began, I am not sure extacly when, but I am sure it was because of my grandfather Boanergue, your deep scientific and philosophical talks made me forever see everything differently, you definitely started a fire in me, that once started, it is very hard to put out. I also want to thank the love of my life, Catalina, without you I would have never had the courage to do everything I did in this research, when you are with me I am free, thank you for the perfect love you gave to me. I feel this work affected my social life with all the amount of hours it required, nevertheless, my close friends know how grateful I am for them being always there for me, thank you all.

Finally, a more esoteric acknowledgment goes to all the non-scientific books that have guided me, not only during my master's, but throughout my entire university journey. Without philosophy and literature, I would not be the man I am today. With that said, I leave a paraphrase from *Don Quijote de la Mancha* that represents my scientific quintessence:

"Como no estas experimentado en las cosas del mundo, todas las cosas que tienen algo de dificultad te parecen imposibles. Confía en el tiempo, que suele dar dulces salidas a muchas amargas dificultades"

Contents

List of Tables

List of Figures

Nomenclature

D	Diameter, m
E	Thermal inertia, $\mathrm{W \cdot K^{-1} \cdot m^{-2} \cdot s^{1/2}}$
F_o	Forchheimer number, -
I	Current, A
I_0	Radiation intensity reference value, $\mathrm{W \cdot m^{-2}}$
I_x	Radiation intensity at distance x, $\mathrm{W \cdot m^{-2}}$
I_λ	Spectral radiation intensity, $\mathrm{W \cdot m^{-2} \cdot sr^{-1}}$
$I_{\lambda b}$	Spectral radiation intensity for black body, $\mathrm{W \cdot m^{-2} \cdot sr^{-1}}$
K	Permeability, $\mathrm{m^2}$
L	Length, m
L_c	Characteristic length, m
M_f	Moisture content, -
P	Pressure, Pa
R	Electrical resistance, Ω ; Specific gas constant, $\mathrm{J \cdot kg^{-1} \cdot K^{-1}}$
Re	Reynolds number, -
S	Sutherland constant, K
T	Temperature, K
T_0	Temperature at sea level conditions, K
T_∞	Ambient temperature, K
T_{exp}	Experimental temperature, K
T_f	Fluid phase temperature, K
T_{ig}	Ignition temperature, K
T_{mod}	Model temperature, K
T_s	Solid phase temperature, K
V_{et}	Volume of Ethanol, $\mathrm{m^3}$
V_f	Volume of fuel, $\mathrm{m^3}$
V_T	Total volume, $\mathrm{m^3}$
V_{void}	Total void volume, $\mathrm{m^3}$
Y	Inertial factor, -
a	Aerodynamic lapse rate, $\mathrm{K \cdot m^{-1}}$

c	Speed of light, $\mathrm{m \cdot s^{-1}}$
c_p	Specific heat, $\mathrm{J \cdot g^{-1} \cdot K^{-1}}$
e	Thickness of heating element, m ; Euler's number, -
g	Gravitational acceleration, $\mathrm{m \cdot s^{-2}}$
k	Thermal conductivity coefficient, $\mathrm{W \cdot m^{-1} \cdot K^{-1}}$
k_f	Fluid phase thermal conductivity coefficient, $\mathrm{W \cdot m^{-1} \cdot K^{-1}}$
k_m	Effective thermal conductivity coefficient, $\mathrm{W \cdot m^{-1} \cdot K^{-1}}$
k_s	Solid phase thermal conductivity coefficient, $\mathrm{W \cdot m^{-1} \cdot K^{-1}}$
m	Thermocouple and heating element mass, kg
m_{et}	Ethanol mass, kg
m_f	Fuel mass, kg
m_{py}	Pycnometer mass, kg
p	Laplace variable, -
$\dot{q}''_{rad}$	Radiative Heat, $\mathrm{W \cdot m^{-2}}$
s	Contact surface heating element, $\mathrm{m^2}$
u_D	Space averaged streamwise velocity: Darcy velocity, $\mathrm{m \cdot s^{-1}}$
x	Direction or distance, m
z	Vertical distance or depth, m
$\mathcal{L}$	Laplace transform, -

Greek symbols

β	Packing ratio, -
β_F	Forchheimer coefficient, $\mathrm{m^{-1}}$
β_λ	Extinction coefficient, $\mathrm{m^{-1}}$
δ	Mean free path length for radiation, m
φ	Porosity, -
κ_λ	Absorption coefficient, $\mathrm{m^{-1}}$
λ	Wavelength, m
μ	Dynamic viscosity, $\mathrm{Pa \cdot s}$
μ_0	Dynamic viscosity of air at sea level conditions, $\mathrm{Pa \cdot s}$
ρ	Air density, $\mathrm{kg \cdot m^{-3}}$; Reflectivity, -
ρ_0	Air density at sea level conditions, $\mathrm{kg \cdot m^{-3}}$
ρ_b	Bulk density, $\mathrm{kg \cdot m^{-3}}$
ρ_{et}	Ethanol density, $\mathrm{kg \cdot m^{-3}}$
ρ_f	Fuel density, $\mathrm{kg \cdot m^{-3}}$
σ	SVR, $\mathrm{m^{-1}}$; Stefan-Boltzmann constant, $\mathrm{W \cdot m^{-2} \cdot K^{-4}}$
σ_λ	Scattering coefficient, $\mathrm{m^{-1}}$
τ	Transmissivity, -
Ω	Solid angle, sr
Φ_λ	Spectral phase function, -

List of abbreviations

BBL	Bouguer-Beer-Lambert Law
CONAF	Corporación Nacional Forestal
FTIR	Fourier Transform InfraRed
FMC	Fuel Moisture Content
ISA	International Standard Atmosphere
LEMTA	Laboratoire Énergies & Mécanique Théorique et Appliquée
LTE	Local Thermal Equilibrium
LTNE	Local Thermal Non-Equilibrium
MLR	Mass Loss Rate
RTE	Radiative Transfer Equation
SVR	Surface-to-Volume Ratio
UAI	Universidad Adolfo Ibáñez
WPI	Worchester Polytechnic Institute

Chapter 1

Introduction

In recent decades, the global climate has undergone unprecedented changes, marking a stark departure from the environmental stability observed in previous centuries. The accelerating pace of climate change, characterized by rising temperatures, extreme weather events, and ecological disruptions, presents a profound challenge to the sustainability of our planet. Understanding these shifts is not merely an academic pursuit but a pressing necessity for informing policies and practices aimed at mitigating and adapting to the profound impacts of climate change (Di Virgilio et al., 2019). One of the significant challenges that persists on Earth is wildfires, affecting regions like Australia, California, Chile, and various other locations, which contend with recurring blazes annually (Nolan et al., 2020). Nevertheless, while suppressing the occurrence of wildfires is impossible, the application of quantitative approaches rooted in scientific principles can significantly mitigate risks to both people and the environment (Moritz, 2014).

Consequently, it is anticipated that these scientific approaches can effectively contribute to reducing the substantial impact of wildfires. A thorough understanding of the complex phenomena underlying wildfires will serve as a solid foundation for building a fundamental comprehension of this phenomena (IAFSS, 2023). Fire research primarily investigates combustion processes that alter both solid and gaseous phases, initiating a chain reaction that allows wildland fuels to burn when exposed to external heat sources. The study of fuel properties directly influences combustion behavior factors, revealing predominant patterns that elucidate trends in this dynamic phenomenon (Yang et al., 2005). Furthermore, additional studies have attested the heat and mass transfer processes in wildfires, examining various areas such as ignition theory of fuels in forest fires (J. L. Torero and Simeoni, 2010), modeling of fuel bed combustion (Peters and Raupenstrauch, 2010), mechanisms of biomass pyrolysis (S. Wang et al., 2017), and more.

While heat transfer and thermodynamics have been studied since the early nineteenth century, the specific area of combustion has transitioned from its nascent stages to a more intermediate phase of research development in the past decades. This indicates that there is still a substantial amount of work that remains to be undertaken (McNamee, 2019). One of the main subfields that requires further development, in addition to those mentioned earlier, pertains to transport theory. This encompasses addressing gaps in the understanding of energy and molecule transport in combustion research. Porous materials, including forest floors in wildland and biomass settings, like packed fuel beds. During combustion, energy and gases permeate through the porous medium. Afterward, a comprehensive study of flow and transport in porous media is necessary to construct and solve mathematical models capable of accurately describing this transport (Leal, 2007). While combustion in packed beds has increasingly captured researchers attention, there are still unresolved issues related to combustion and transport in porous media for predictive capabilities in the context for wildfires.

To explore the complex transport processes critical to wildfire behavior, this study focuses on permeability and extinction coefficients within packed fuel beds. Understanding these properties is essential for comprehending both airflow dynamics and radiation extinction mechanisms. Thus, an experimental investigation will be conducted to systematically assess permeability and extinction coefficient values across various characteristics of porous media. These characteristics include porosity, packing ratio, surface to volume ratio, and bulk density, each playing a crucial role in the transport of fluids and heat within fuel beds. By examining these parameters, this study aims to enhance our understanding of how these media configurations influence transport phenomena, crucial for wildfire spread dynamics.

1.1 Thesis Objectives

1.1.1 Overall Aim

The objective of this thesis investigation is to characterize transport processes within bench-scale fuel beds in the context of wildfire behavior, particularly by studying fluid mechanics and radiative transfer, with specimens of *Pinus radiata* pine needles and elongated wood elements within these fuel beds. The primary aim is to examine how fuel bed properties such as porosity, packing ratio, geometry, surface-to-volume ratio, and moisture content affects relevant properties of the fuel bed. This will be achieved through a combination of experimental and analytical approaches to determine permeability, absorption coefficients, transmissivity and reflectivity from visible to far infrared spectrum, thermal inertia and in-depth temperature distributions combined with one dimensional models. Through this work, diverse properties and qualities of these particular fuel beds, once characterized, will reveal the behavior behind flame propagation and wildfire contexts.

1.1.2 Supporting Objectives

The subordinate objectives based on the previous statement are aimed to obtain a comprehensive characterization of detailed transport processes, these are detailed as follows:

Achieve a full characterization of dead and dry *Pinus radiata* pine needles and also elongated wood elements at UAI, in Chile:

- Construction of an acrylic vertical wind tunnel to carry out an experimental study with a sealed system which allows air flow through it to detect pressure drops in porous fuel beds to measure permeability and other accurate fluid mechanics parameters.

- Design and implementation of a vertical experimental setup comprising a light-emitting source directed towards porous fuel beds, with detection facilitated by a photodiode in the visible spectrum for absorption coefficient determinations.

Complementarily, Achieve a full characterization solely of dead and dry *Pinus radiata*, at an international internship at LEMTA, in France:

- Study from visible to far infrared spectrum the radiative responses of small pine needle fuel beds for: reflectivity, direct and diffuse transmissivity with an FTIR equipment.

- Thermal inertia model and microcalorimeter measurements to obtain conductivity and specific heat of dead pine needles.

- In-depth temperature behavior in dead pine needle fuel bed for transient and steady state distributions for one dimensional analyses.

Chapter 2

Background

2.1 Porous Materials

Porous materials are characterized by the presence of internal voids and cavities that facilitate the absorption or movement of fluids (Kaviany, 1995). This intrinsic network of empty spaces within their structure allows for the transport of various substances. The volume that contains the solid sections of the material is denominated the "solid matrix" which logically does not contemplate the void volume. Porous materials can be found nearly everywhere, some common examples include: metal foams, rocks, bricks, soil, sand, coal, and, more importantly for this investigation, wildland fuels found in forests. Naturally, what can be found in forests is basically wood, leaves, grass, and many other. Although the bulk porosity is quite different for each substance, the principles for porous media follow similar basic physical laws. To classify a material as porous, it must satisfy two essential criteria according to (P. Liu and Chen, 2014):

- The structure must exhibit high porosity, indicating the presence of numerous voids throughout the material.
- It must allow the transport of fluids through the material, meaning that the pores must be interconnected to allow fluid flow (although, there can be porous materials with isolated pores, but these are rare and used for specific applications).

In the context of a scientific thesis, the categorization of porous materials based on pore size is crucial for distinguishing between the primary groups according to pore diameter. This classification depends on the type of porous material under consideration. For instance, in rocks, concrete, or materials with similar characteristics, the pores can typically be in the nanometer range.

Conversely, for other types of porous materials, the pore sizes may fall within the micrometer range. Accordingly, pore structures can be broadly classified into two categories: those with very large pores, often referred to as caverns, and those with very small pores, commonly known as micropores (Kaviany, 1995). For this investigation, for packed fuel bed configurations, big pores are encountered and the study will follow compositions with cavern pore structure.

Porous materials hold remarkable properties with their complex structures and the attributes for this kind of materials are transcendental to many fields. Chemical processes need porous materials for better efficiency of chemical reactions, an example of this is the recent development of zeolites and metal organic frameworks for the study of catalysis (Yu and Williams, 2022). In mechanical engineering porous materials offer versatility and performance for various systems and designs that require the properties of these materials. New applications are appearing with new innovations such as lightweight porous metals extensively used in aerospace industry. Other application is the usefulness of aerogel in today's designs because of their super insulation properties for thermal processes (Koebel et al., 2012). Another field that studies porous media is biology since the human body is made up of porous materials (e.g. the largest organ of the human body is the skin which regulates the temperature of the body, among others). In line with the proposed investigation, the environment is an extremely relevant area for the study of porous materials (i.e, natural fuels such as trees, leaves, and everything that can be burned in a wildfire) where the main scenario for wildfires occurs in places like forests with vast wildlife. Therefore, these relevant applications can be expressed succinctly in the following Table 2.1:

Table 2.1: Applications of porous materials to different areas.

Area	**Applications**
Chemicals	Studies such as catalysis for chemical reactions. These materials provide tailored environments for chemical processes.
Mechanical	Lightweight structures are transcendental for engineering. Porous metals are widely present with increasing applications.
Biology	Intrinsic porous behavior of the human body. Transport through porous media such as tissue.
Environment	Natural materials and fuels compose part of the porous materials found in nature. Characterizations for these porous media can help better understand the behavior and transport through them.

2.2 Biomass

By definition, biomass is all that makes up the biological material on Earth, which means that it is conformed by plants, animals, and bacteria. The plants in this context (i.e, Plantae Kingdom for its scientific name) refer to all that is not animal nor bacteria. Therefore, from an energetic standpoint it refers to all organic matter that is usable in a renewable and recurrent manner. In this context, this specific biomass (i.e. plants) is understood as a fuel (Finney et al., 2021).

Nature is a substantial energy producer, in the case of photosynthesis the output power it produces is tremendous, in the vicinity of 100 TW according to (Nealson and Conrad, 1999). To put this into perspective, energy use by humanity is in the range of $15 - 20$ TW, so roughly one fifth of the previous value of photosynthesis. For centuries human civilization has been using this inherent form of energy that our planet offers and with the development of technology this consumption has been increasing drastically.

In the context of wildfires, the accumulation and characteristics of these fuels play a critical role. Forests contain a vast array of fuels; however, the critical characteristics of these fuel particles are their size, shape, moisture content, and material properties. Therefore, the distinction between fuel particles and fuel beds is that if the fuel particle is known, then the fuel bed just refers to: quantity (i.e. how many fuel particles are loaded onto the bed), depth, compactness, and continuity (Finney et al., 2021). Dry conditions and an abundance of fine fuels, such as grasses and leaves, can lead to rapid ignition and fast-moving flames. Conversely, larger fuel particles, like logs and branches, burn more slowly but contribute to sustained, intense heat over longer periods. For this reason, small and large fuel particles induce different reactions in these phenomena due to different characteristic lengths, since larger volumes and superficial areas can vary and modify how flames propagate. Evidently, the properties of these fuels further affect combustion processes and flame behavior.

Furthermore, these fuels have a significant role in wildfires, because they serve as the primary material through which ignition and fire spread phenomena occur. Consequently, the understanding of fuel treatment and their several qualities are widely relevant for the wildfire science. Numerous studies have attempted to characterize biomass fuel beds to improve the physical response and effects on wildfires (Prichard et al., 2021; Ager et al., 2021; Walker et al., 2020). In this context, a crucial component of this research is the examination of fuels and their influence on wildfire dynamics.

This research focuses on understanding transport processes in primarily wood and pine needles, chosen as the primary biomass feedstock. This material is selected due to its relevance in wildfires. As illustrated in Figure 2.1, forests contain various types of fuels, allowing wildfires to propagate through different fuel sources. This study focuses specifically on ground fuels within forests, which in this specific context include leaves, needles, and duff materials commonly found in wildland environments, therefore, justifying the selection of wood and pine needles.

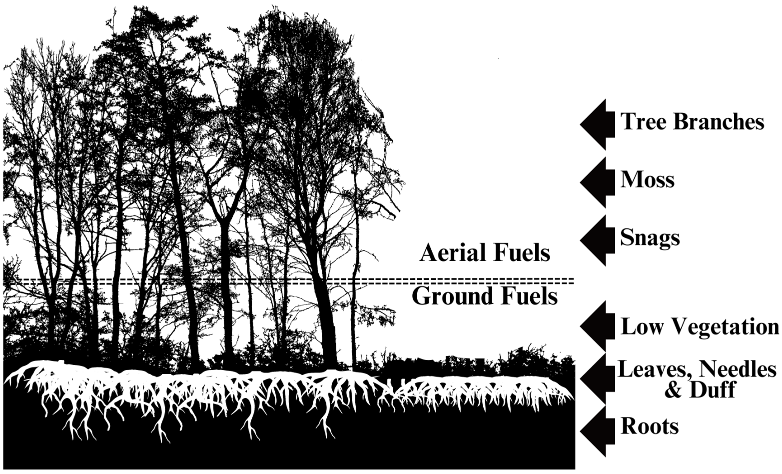

Figure 2.1: Fuel components for different strata of fuel in wildland environments.

To accurately replicate wildland fuels, as depicted in Figure 2.1, surrogate fuel beds are utilized to demonstrate comparable behavior. This particular fuel bed aims to emulate the behavior of ground fuels. Consequently, the novel application of surrogate fuel beds introduces a sample holder designed to contain the specimen within it. The features of this holder can be custom-built for specific experimental requirements (Bartoli et al., 2011). An example is illustrated below, where the specimen within the container is presumed to exhibit properties analogous to those of actual wildland fuels.

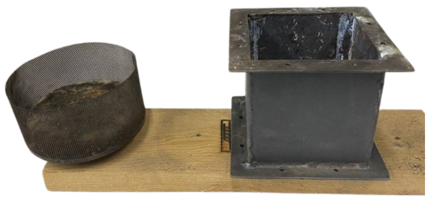

Figure 2.2: Example of sample holders for experimental use for wildland fuels.

While Figure 2.2 suggests a circular steel recipient with holes on the surface, more geometries can be easily built. Surrogate fuel beds will facilitate a systematic and repeatable examination of the chosen fuel, providing deeper insights into the transport processes within porous fuel beds. This study is particularly relevant for understanding how wildland fuels behave, with the aim of developing accurate models to describe the physical processes and validate desired outcomes.

2.3 Characterization of Packed Beds

In this section, several characteristics of packed beds are discussed, focusing on the primary factors that influence the proposed research. These factors are critical for understanding fluid flow and heat transport in porous media and are thoroughly investigated in the subsequent subsections.

2.3.1 Porosity

As was stated before, porous materials are composed by a solid matrix and interconnected voids. In this context, porosity is defined as the total void volume divided by the total volume occupied by the solid matrix and void volumes (Kaviany, 1995). In other words, this statement translates to Equation 2.1, where the total volume is $V_T = V_{SolidMatrix} + V_{void}$, implying that porosity fluctuates between: $0 < \varphi < 1$, zero meaning no pores and one meaning no solid matrix. This is easily mathematically described by the following expression:

$$\varphi = \frac{V_{void}}{V_T} \tag{2.1}$$

Different methods are used in the scientific community to estimate the porosity of porous materials. Some of these methods are geometric dimension, particle and bulk density, volume displacement, mercury porosimeter, micro-CT, and nuclear magnetic resonance (Qiu et al., 2015). Some of the previous methods are not necessary for this investigation, since the porosity of a surrogate fuel bed can be obtained with the simplest of the mentioned methods. With the density estimations, a rigorous value for porosity can be determined, the bulk or apparent density ρ_b is simply obtained knowing the mass of the sample contained in the surrogate fuel bed and the total volume V_T occupied by it. The mass is a given unaltered value, but the total volume can be standardized by compacting the samples leaving them with one height. The mass of the fuel sample is m_f and therefore:

$$\rho_b = \frac{m_f}{V_T} \tag{2.2}$$

Then, once the bulk density is calculated, the density of one particle ρ_f must be measured with the desired method, and through these two values the porosity of the entire sample is obtained. Hence, porosity yields the following equation, which correlates with a dimensionless number representing the porosity characteristics of a fuel bed:

$$\varphi = 1 - \frac{\rho_b}{\rho_f} \tag{2.3}$$

The solid volume fraction for the previous equation (i.e., also described as the packing ratio, $\beta = \rho_b/\rho_f$) is merely defined by the relation between these two aforementioned densities. Afterwards, it will be defined more accurately, since moisture plays a small but important role in determining this volume fraction much more precisely (Bal et al., 2012). Some well known porosities are listed in Table 2.2, ranging from highly porous materials to those with very low void fractions.

Table 2.2: Average bulk porosities for several substances (Mueller et al., 2021; Scheidegger, 1974).

Substance	φ **(-)**
Foams	0,98
Forest Litter	0,90 - 0,98
Fiber Glass	0,88 - 0,93
Leather	0,56 - 0,59
Sand	0,37 - 0,50
Bricks	0,12 - 0,34
Concrete	0,02 - 0,07

In this investigation, it is a fact that the pores of the materials are interconnected, establishing it as the porous medium continuum. Within the free space defined by porosity inside the porous material, fluids can occupy this region. Thus, for the purposes of this research, it is imperative to consider the material as interconnected when fluid flow is in focus. It is essential to note, however, that while this is crucial for fluid transport, heat can also propagate through the solid matrix (i.e. radiation and conduction heat transfer).

2.3.2 Permeability

Permeability is a property that describes the ability of the porous material to allow the passage of a fluid, therefore it is the measure of flow conductance of the matrix (Kaviany, 1995). The flow conductance can be understood as the ability of a porous material to transmit fluids under a pressure gradient. Moreover, the hydrodynamic behavior can be derived with mass and momentum conservation at the pore level. Permeability is denoted with the letter K (some literature use lower case k) and it is the measure of the flow conductance and is expressed in m^2, or, in other words, the capacity of any porous material to allow fluid flow. The definition and characterization are rooted in Darcy's and Forchheimer's Law and it can be described using these laws which will be discussed later in section 2.4.

Nonetheless, this factor is highly dependent on the geometry of the solid matrix, in other words, permeability is strictly dependent on geometry of the media studied. This means that permeability is known for simple and already common structures, but it is an interesting challenge to measure permeability in complex structures (i.e., highly anisotropic media). For the scope of this project, the desired geometries can be designed and established in any way and the permeability can be obtained through different methods. Some methods include: transient methods for small increments of pressure (Brace et al., 1968), dynamic pulses of pressure (Egermann et al., 2003), quasi-steady state methods for unsteady flows for very low permeabilities (Jannot and Lasseux, 2012, Jannot et al., 2007), pore pressure oscillation method (Y. Wang and Knabe, 2010).

Moreover, the need to understand and most importantly to measure permeability is because it is a key aspect that affects heat release in wildfires, where lower permeabilities mean slower burning and longer flame residence times (Finney et al., 2021; Santoni et al., 2014). Other authors measure this value with the same intention, but the data treatment is delivered with tensor calculus since it can give a matrix value for permeability (Huang et al., 2011), but this is beyond the scope of this thesis. A simple way to obtain the permeability of a porous material can be simply with the use of a wind tunnel (i.e. or a similar equipment such as a permeameter proposed in this thesis, which applies the same principle) so that the pressure drop caused by the porous media can be determined (Fehrmann et al., 2017), and, through Darcy's law or a modified Frochheimer's law (also proposed by the same author), calculate the permeability.

One last aspect related to permeability is that there is no general relationship between porosity and permeability (Kaviany, 1995). Limited empirical and semiempirical correlations exist, but can only be applied within the specific constrains under which these were developed for. The only attempts related to this exist only for semiempirical correlations, and to work correctly many restrictions must be applied, meaning that it is not fully representative for what happens in reality. Nonetheless, permeability can be expressed as a function of numerous factors such as degradation and consumption of the material in fire consumption experiments as suggested by (J. L. Torero, 2016). In synthesis, this value of permeability accounts for the interstitial surface area, the path that particles follow with flow movement, and other hydrodynamic qualities, thus can adequately be obtained with the laws mentioned before. A concise but diverse variety of known permeability values is presented in the following table:

Table 2.3: Bulk permeabilities for several substances (Mueller et al., 2021; Scheidegger, 1974).

Substance	K **(m²)**
Brick	$4{,}8 \cdot 10^{-15}$ to $2{,}2 \cdot 10^{-13}$
Leather	$9{,}5 \cdot 10^{-14}$ to $1{,}2 \cdot 10^{-13}$
Fiber Glass	$2{,}4 \cdot 10^{-11}$ to $5{,}1 \cdot 10^{-11}$
Sand	$2{,}0 \cdot 10^{-11}$ to $1{,}8 \cdot 10^{-10}$
Hair Felt	$8{,}3 \cdot 10^{-10}$ to $1{,}2 \cdot 10^{-9}$
Fiber Filters	$1{,}1 \cdot 10^{-9}$
Forest Litter	$6{,}8 \cdot 10^{-7}$ to $1{,}0 \cdot 10^{-5}$

2.3.3 Packing and Surface-to-Volume Ratios

Lastly, packing ratio and surface to volume ratio (often abbreviated as SVR) are two quantities of interest which reveal simple and interesting fuel properties. The fuel bed packing ratio (also known as fuel volume fraction or solid volume fraction) is denoted by β and this ratio is the percentage of fuel bed volume that is occupied by fuel particles (Rothermel, 1972), this value is dimensionless. This value is widely used in the fire research community since it is an important factor in quantifying the behavior of fire. The chosen correlation for the packing ratio for this research is the following:

$$\beta = \frac{m_f / V_T}{(1 + M_f)\rho_f} \tag{2.4}$$

This equation is suggested by (Vaz et al., 2004) and it quantifies the already discussed quantities of fuel mass and total volume, but the density of the fuel ρ_f is to account for the density of all dry samples (e.g. the density of a fuel bed of 30 pine needles would be this value) and m_f / V_T for the bulk density which is the value that directly affects the packing of the sample. The value of M_f refers to the moisture content which is expressed on a dry mass basis, this is measured quite simply by drying and weighing the porous fuel sample and obtaining the water content. Based on the methodology proposed by the authors, the estimation of fuel bed properties allows for the study of any packing ratio, depending on the values selected for the parameters in Equation 2.4. Analogous to Equation 2.1, if the mass fuel occupies a smaller total volume V_T, then porosity and the packing ratio both increase with this volume reduction, implying that volume variations are the same for both.

Consequently, surface to volume ratio is quite straightforward (i.e. SVR= Surface area/Volume) and it is the ratio of the surface area of a particle with respect to the volume of the same particle, it is denoted by σ (i.e. $\sigma = S/V$), and the units of this ratio are m^{-1}. A known method used for calculating this ratio is done by water immersion (Fernandes and Rego, 1998), where a simple correlation between the absorbed water by the fuel particle and the dry volume results in this ratio. A more precise method is with the use of CAD software environments (i.e. such as MicroStation used by (Vaz et al., 2004)) which can be used to obtain digital photographs that show the numerical characteristics of cross section of a fuel particle. This technique correlates the perimeter with the area of the cross section of the fuel, this yields σ = Perimeter/Area, giving the correct units.

Nonetheless, both methods are valid and choosing between them is mainly a matter of precision. The use of the perimeter to area ratio assumes a constant length across all samples, making it a more straightforward representative value for defining this characterization. This simplification is simply justified given that measuring the length of every individual pine needle would be an overwhelming task, and with a considerable sampling this average can be easily determined. Since the geometries of natural biomass fuels follow certain patterns, approximated known values for SVR can be used for specific fuels since some are known and well established in the scientific literature. Some of the surface to volume ratio values for dead pine needle beds are seen in Table 2.4:

Table 2.4: Examples of known dead pine needle beds SVR values (Bartoli et al., 2011; Thomas, 2017).

Species	σ **(m^{-1})**
Pinus Halepensis	7.377
Pinus Pinaster	3.057
Pinus Laricio	4.360
Pinus Rigida	4.776
Pinus Resinosa	7.024
Pinus Strobus	14.173

2.4 Fluid Flow in a Porous Medium

Momentum equations for flow in these cases can adopt different forms for porous medium, these expressions share features with the Navier-Stokes equation. In fluid mechanics for porous media, the flow exhibits linear characteristics at low velocities (i.e. a direct proportionality between the variables), where inertial effects are negligible. However, as the velocity increases, inertial effects become significant and can influence this linearity. These two flow regimes are known as the Darcy and Forchheimer regimes, corresponding to non-inertial and inertial behaviors, respectively, each with a defined formula.

2.4.1 Darcy's Law

The measurement of fluid flow within a solid matrix and the resistance offered by the material can be traced back to Darcy's pioneering work in the nineteenth century (Darcy, 1856). Darcy's experiments involved a straightforward setup using sand as the porous medium and water as the fluid. In this configuration, the mass flow rate of the fluid $\dot{m}$ (i.e. which can be air for other cases and is simply obtained by the density and velocity of the fluid, and with the geometry of the media) can be measured and the filtration or Darcy velocity u_D can be determined by dividing the mass flow by the cross-sectional area of the channel. Darcy velocity represents the flow rate per unit area of the entire cross-sectional area of the porous medium. A distinction is made with Darcy velocity and the actual velocity the fluid has in the pores of the media. The term seepage velocity or interstitial velocity is used to account for the velocity through pore spaces. This velocity is related to Darcy velocity through the Dupuit-Forchheimer relationship (Nield and Bejan, 2013) and it states that seepage velocity times the porosity yields Darcy velocity (i.e. $v\varphi = u_D$). Nonetheless, for the purpose of this research, Darcy velocity will account for the normal velocity at the surface of the porous media where the fluid enters.

Subsequently, by applying a volumetric force balance to the flow, he discovered that the bulk resistance is characterized by the fluid's viscosity μ (i.e. the fluid viscosity in this case is more specifically the dynamic viscosity with units $\mathrm{Pa \cdot s}$) and the solid matrix's permeability K. These fundamental measurements were instrumental in establishing the foundational equation that describes fluid flow through porous media.

$$-\frac{dP}{dx} = \frac{\mu}{K} u_D \tag{2.5}$$

Here, Equation 2.5 shows that the pressure gradient dP/dx along the flow axis movement is negative. The slope for this pressure difference is negative because the governing dynamic of the flow is from a high pressure region towards a low pressure one, therefore, if there is no pressure difference then there is no flow. In the context of fluid dynamics, the relationship between pressure and velocity is directly proportional. In this sense, the proportionality constant is the permeability. Consequently, a greater pressure gradient results in a higher flow velocity:

$$-\frac{dP}{dx} \propto u_D \tag{2.6}$$

In summary, the mass flow through a porous medium with a velocity u_D in an arbitrary geometry experiences pressure drops when measured at two different locations separated by a distance L as is shown in the general schematics for Darcy's law in Figure 2.3. Here, at the entrance of the testing volume the inlet mass flow of air has disordered behavior due to it being a jet of air that at the beginning is inevitable to suppress. Later, once the air travels through the distance, it is possible to obtain a uniform velocity profile where it is reasonable to test the pressure difference between P_1 and P_2, and finally the air flow exits through the outlet.

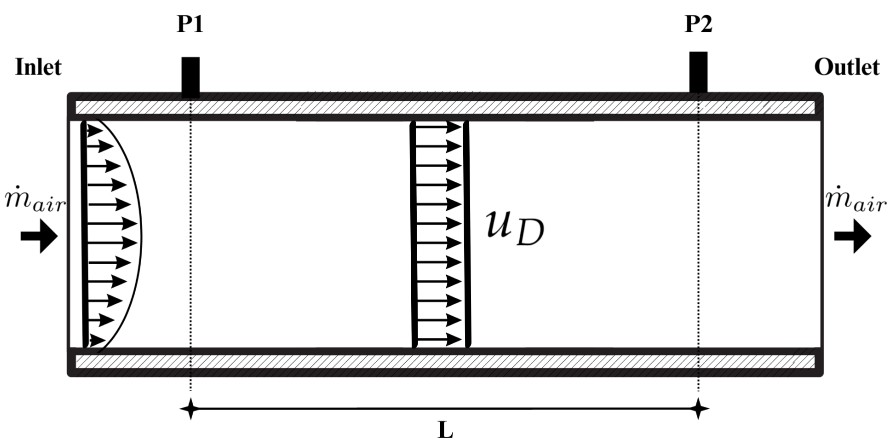

Figure 2.3: Schematics for flow movement for pressure difference measurement.

2.4.2 Forchheimer's Equation

The previous law has limitations, meaning that there are extensions (i.e. exceptions) to the law derived by Darcy. The equation holds linearity for velocities that are relatively small, but for increasing velocities this linearity breaks and it slowly diverges due to inertial effects. The effects are often called non-Darcy, but it can also be understood as inertial effects. Many attempts have been made to define the transition from Darcy to non-Darcy regime, but it is dependent of the porous sample and, of course, the geometry. The general expression for fluid flow with inertial effects is the Forchheimer's Equation (Whitaker, 1996), where an extra component is added to Equation 2.5 to account for inertial effects:

$$-\frac{dP}{dx} = \frac{\mu}{K}u_D + \rho\beta_F u_D^2 \tag{2.7}$$

Some literature express this inertial factor β_F as C_f, but what is relevant from the previous equation is that this arbitrary value denotes how the flow is not necessarily linear. Transition from laminar to turbulent flow is related to the Reynolds number Re, hence, knowing the density and velocity of the fluid directly influences the Reynolds number, where different values of this dimensionless number must indicate how is the general behavior. The usual Reynolds number can be written as follows:

$$\mathrm{Re} = \frac{\rho D u_D}{\mu} \tag{2.8}$$

For the case of packed beds the diameter can be used as a characteristic length of the samples (i.e. $D \equiv L_c$), which is valid and more easily measured in the Reynolds number calculation (Bear, 2018; Zeng and Grigg, 2006). Thereafter, if velocity is much higher and not compatible with Darcy's Law, the Forchheimer regime is used, also known as quadratic drag (due to the squared term of velocity) (Nield and Bejan, 2013). This regime is for when the break in linearity is due to drag induced by obstacles which are comparable to surface drag resulting from friction forces present. The problem with the quantification for this regime is that there is no general way of knowing when non-Darcy regime is present due to lack of consistency of the definitions and critical values. Some of these attempts include a Reynolds number accounting for permeability (Green and Duwez, 1951), others included the porosity value in the Reynolds number (Ergun, 1952), and some use Equation 2.8 for the particles, but for this simple expression the characteristic length is not easily determined. These several attempts are shown in Table 2.5.

Table 2.5: Examples of different criteria for Reynolds number (Zeng and Grigg, 2006).

Researchers	**Re$_{crit}$**	**Context**
Chilton and Colburn	$40 - 80$	Packed particles
Fancher and Lewis	$10 - 1000$	Liquids in sand and rocks
Green and Duwez	$0{,}1 - 0{,}2$	Porous metals
Andrade et al.	$0{,}01 - 0{,}1$	Disordered porous media

Nevertheless, the most recent scientific literature suggests that for the general case (i.e., for arbitrary particles that do not fit the contexts from Table 2.5), it is appropriate to simply use Reynolds expression from Equation 2.8 (Bear, 2018). Since the criterion for the Reynolds number is very diverse and not general because of the specific context of application, another recommended approach that (Zeng and Grigg, 2006) suggest is using the Forchheimer number for a more general and standardized criterion that defines the regime of flow based on characteristics of the fluid and the inertial factor, this number is:

$$F_o = \frac{K\beta_F \rho u_D}{\mu} \tag{2.9}$$

The value β_F is called the Forchheimer coefficient which is also present in Equation 2.7 with m^{-1} units, this is defined by permeability K and a dimensionless inertial factor Y, as shown in the following correlation:

$$\beta_F = \frac{Y}{\sqrt{K}} \tag{2.10}$$

With the previous equations, the Forchheimer number represents a ratio of inertial and viscous pressure losses, the recommended critical value by the authors corresponds to a limit value of $F_o \geqslant 0{,}11$. The implication of a Forchheimer number greater than this limit implies that Equation 2.7 can be used. Besides the theoretical analysis, (Fehrmann et al., 2017) empirically concluded the validity for permeability experiments in non-Darcy regime.

A visual representation of the transition from the Darcy regime to the Forchheimer regime proves helpful in illustrating the departure from linearity. As depicted, the relationship between flow regimes and pressure gradient reveals a noticeable deviation from linear behavior when this difference becomes substantial. Figure 2.4 represents the described behavior obtained from (Bear, 2018). It is important to remark that Pre-Darcy Flow is not mentioned due to the extremely low velocity and pressure gradient for it to happen in the context of this research (Macini et al., 2011).

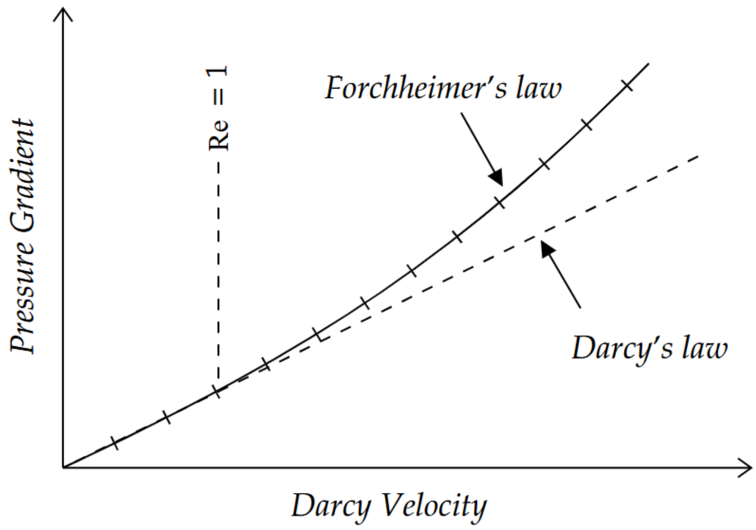

Figure 2.4: Classification of flow regimes in porous media.

2.5 Heat Transfer Within a Porous Medium

The examination of heat transfer properties should describe adequately how interparticle energy interactions are through conduction (i.e. how individual particles within the arrangement interact with one another). Afterwards, how gases flow inside and outside the system, where convection drives this heat transport for flame propagation. Lastly, radiation, the most intricate heat transfer mechanism in the whole system, where appropriate physical description and behavior is crucial for the solution of heat transfer problems and to complement convection for the flame spread. Since the main modes of heat transfer are conduction, convection, and radiation, these will be explained for the context of wildfire applications in the next subsections.

Conducting experiments on transport phenomena in the context of wildfires necessitates a profound understanding of the physical processes occurring during a fire. In particular, gaining insights into the physical mechanisms of flame spread is crucial for explaining these transport processes. The mechanisms governing the movement of energy and molecules are intricately linked to the spread of the flame and the combustion occurring at the forefront of this process. Figure 2.5 portrays the main variables in the physical progression for flame propagation. The figure illustrates the logical pathway of the fire, where the progression is from the already burnt area toward the unburnt region. This flame propagation consistently advances to consume the unburnt fuels. The leading edge of propagation is where the primary heat is transferred to the fuel, involving the mentioned heat transfer modes. Examining a small control volume within this leading edge, as the schematic depicts, provides valuable insights into the behavior of porous medium in this context. For accurate mathematical descriptions of heat transfer in porous media there is an important problem to consider, which is a condition of Local Thermal Equilibrium (i.e., abbreviated as LTE). The theoretical importance of this condition is that for accurate depiction of the energy equation in practical applications it must be determined if fluid and solid temperatures are roughly equal, implying there is LTE (Zhang and Liu, 2008). While LTE may not hold in many real life scenarios, it is often valid for laboratory conditions where constant temperature gradients and appropriate insulation designs, then LTE can be correctly assumed for a more straightforward analysis (Vadasz, 2005). Therefore, in the case of solid and fluid temperatures being different, two equations arise from this discrepancy, this two phase phenomena is:

$$\text{Solid phase}: \quad (1-\varphi)(\rho c_p)_s \frac{\partial T_s}{\partial t} = (1-\varphi)\nabla\cdot(k_s \nabla T_s) + \nabla\cdot\dot{q}''_{rad} \tag{2.11}$$

$$\text{Fluid phase}: \quad \varphi(\rho c_p)_f \frac{\partial T_f}{\partial t} = \varphi\nabla\cdot(k_f \nabla T_f) - (\rho c_p) u_D \cdot \nabla T_f + \nabla\cdot\dot{q}''_{rad} \tag{2.12}$$

Where the subscripts s and f refer to the solid and fluid phases. In this regard, the energy equations for heat transfer in a porous medium are complicated to solve due to the many variables it has and the specific conditions it may require for each phase (Nield and Bejan, 2013). Both Equations 2.11 and 2.12 accurately describe the following fire propagation in a wildfire scenario:

From the previous illustration and information, the relevant heat equation (i.e. energy equation) to study for the heating of a porous medium is given in Equation 2.13. This equation is obtained by setting the problem to one phase, where solid and fluid temperatures are the same, which provides a valid simplification for accurate analysis. It is important to note that this equation is for an inert solid:

$$(\rho c_p)_m \frac{\partial T}{\partial t} = \underbrace{\nabla\cdot(k_m \nabla T)}_{Conduction} - \underbrace{\varphi(\rho c_p)_f u_D \nabla T}_{Convection} + \underbrace{\nabla\cdot\dot{q}''_{rad}}_{Radiation} \tag{2.13}$$

It can be recognized that the term on the left-hand side, which is from the standard form of the first law of thermodynamics, represents the rate of change of internal energy of the control volume. Then, the underbrace terms clearly denote what composes this specific equation for porous media. The subscript m just refers to the properties of the medium, while the rest of the symbols will be explained in their respective subsection. With this, the heat transfer modes for this phenomenon are the following:

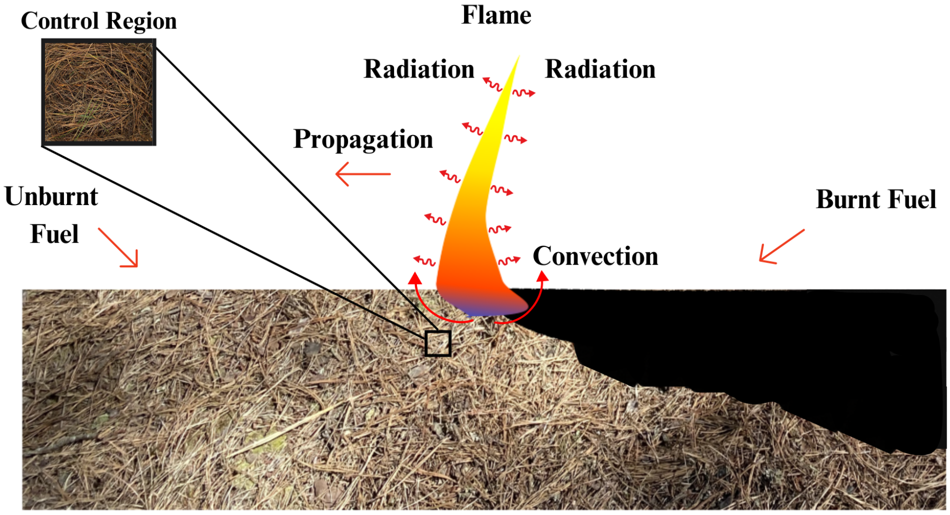

Figure 2.5: Flame propagation in wildland fuels.

- **Conduction:** Effective conductivity of the medium (k_m). The expression refers to the net rate of heat conduction into a unit volume of the medium. This variable comprises solid and fluid conductivity.
- **Convection:** Gas heat flow with velocity through the medium φu_D. The expression refers to the rate of change of thermal energy per unit volume due to convection.
- **Radiation:** External radiation heating up the porous medium. This last expression is the net radiant heat flux towards the region.

Under the assumption of one-dimensional heat transfer, the system can be modeled using the following simplified governing equation:

$$(\rho c_p)_m \frac{\partial T}{\partial t} = k_m \frac{\partial^2 T}{\partial z^2} - \varphi(\rho c_p)_f u_D \frac{\partial T}{\partial z} + \frac{\partial q''_{rad}}{\partial z} \tag{2.14}$$

The previous equation is favorably simplified for in-depth analysis (i.e. in-depth direction is the z axis) where only one spatial axis is studied. It is important to mention that all aforementioned partial differential equations of heat transfer within a porous medium lack boundary conditions, as these must be specified according to the particular experimental or modeling problem under study.

Now, considering solely the control region (i.e. control volume) from Figure 2.5, a generalized heat transfer scenario can be established in a small designated volume for analysis. Hence, this heating of this small fraction of unburnt fuel is shown by Figure 2.6 based on known behavior for lignocellulosic material in wildfires and the distinctive temperature distribution that is expected for these kind of biomass porous materials (Reszka and Torero, 2016).

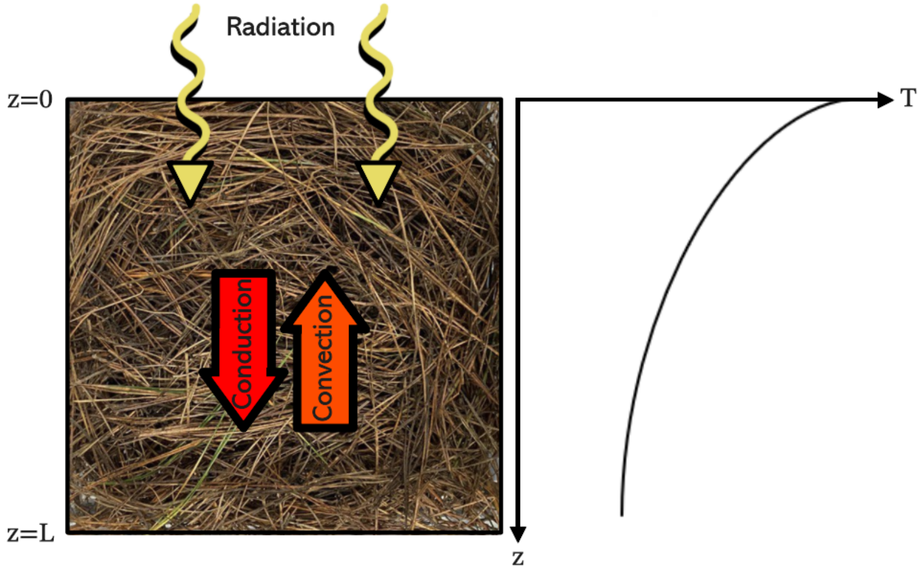

Figure 2.6: All modes of heat transfer in the control region for lignocellulosic material (from Figure 2.5) along with the expected in-depth temperature distribution decay profile.

Taking this into consideration, the events occurring in the control region depicted in Figure 2.5 and 2.6 primarily involve the addition of thermal energy through heat conduction and radiation to the region and convective heat flowing outwards due to air movement as a result of the flame that is spreading. Research on porous materials in wildfires indicates that, under conditions of LTE (i.e., fluid temperature $=$ solid temperature $\equiv T$), the temperature distribution is directly linked to the permeability of the medium (Kaviany, 1995). This relationship is reflected in the behavior shown in Figure 2.6, alongside the corresponding temperature distribution along the z-axis of the graph, where, the deeper the distance from the surface, the greater the decrease of the temperature. In summary, this represents the primary mechanism by which energy and mass are transported in such events. Although the assumption of LTE is idealized, it remains valid for controlled laboratory studies. In contrast, deviations from thermal equilibrium (known as Local Thermal Non-Equilibrium or LTNE) must be expected under real wildfire conditions.

2.5.1 Conduction

First and foremost, it is essential to recognize that thermal conductivity is a property influenced by temperature, bed material, and structure. However, the most challenging aspect affecting conduction in porous media is associated with structural modeling (Kaviany, 1995). Specifically, interparticle conduction remains ambiguously defined for porous materials. A thorough understanding of the structure and model is crucial for developing more accurate expressions that properly explain how conduction is developed.

The fundamental physical explanation for this behavior is succinctly captured by Fourier's Law of heat conduction, which describes the heat transfer process in the context of a one-dimensional temperature distribution $T(x)$ along a distance x (I.-S. Liu, 1990). Henceforth, Fourier's Law carries the proportionality coefficient k for conductivity, an inherent property of the material of study, since different media conduct heat at different rates.

However, in the case of porous materials, a practical approach to assess their thermal conductivity is through the measurement of the thermal inertia (Jannot et al., 2005). In this context, thermal inertia (i.e., also found in scientific literature as thermal effusivity) is defined as the ability of a material to exchange thermal energy with its surroundings, and it is defined as:

$$E = \sqrt{k\rho_b c_p} \tag{2.15}$$

For porous media, the thermal inertia can be obtained through two ways: a simplified estimation or a more rigorous method that has a higher accuracy. The simplified method is done by tracing a temperature slope over a time interval and by performing a simple linear regression, afterwards a residue is calculated between the temperature slope with respect to the linear regression.

In contrast, the complete model for thermal inertia estimation is based on several assumptions: one dimensional heat transfer, the heating element is with a uniform temperature, and an electrical resistance is considered with heat emanating only through its surfaces and not the sides. Under these assumptions, the expression for the temperature evolution that is modeled for the study of thermal inertia of a porous material is defined by the following equation:

$$T(t) = \frac{R}{s} I^2 \mathcal{L}^{-1} \left\{ \frac{1}{p} \frac{1}{\frac{\frac{mc_p}{s} p + (1 + R\frac{mc_p}{s} p) E\sqrt{p}}{1 + RE\sqrt{p}} + E_i\sqrt{p}} \right\} \tag{2.16}$$

Here, m and c_p is the mass and specific heat of both the thermocouple plus the heating element, I denotes electrical current used to heat up the material, and R represents electrical resistance. The variable s corresponds to the contact surface area of the heating element, and p is the Laplace variable. The final model for the temperature $T(t)$ thus depends on the known insulant thermal inertia, E_i, and hence the desired thermal inertia of the material under study, E. The following illustration represents how these variables are used in a device.

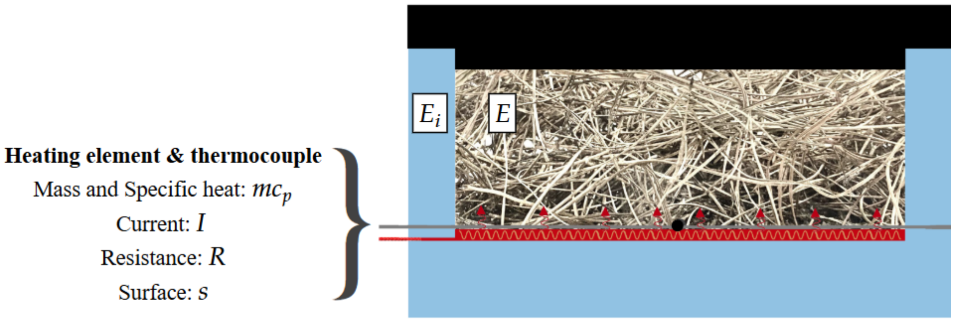

Figure 2.7: Illustrative side view sketch for temperature evolution variables involved for thermal inertia model.

This model can then be implemented in conjunction with a parameter estimation algorithm to iteratively determine the unknown parameters in Equation 2.16. Since the model assumes that the material under study behaves as a semi-infinite medium, the time interval should be at least 400 to 500 seconds to ensure this condition is satisfied (Bal et al., 2013).

In summary, once the thermal inertia E is determined with high precision, and combined with independent measurements of bulk density ρ_b and specific heat c_p, the effective thermal conductivity k of the porous material can be reliably inferred, with an uncertainty as low as 3% under ideal conditions (Jain, 2023).

2.5.2 Convection

In wildland environments, such as fuel beds of pine needles, heat transfer in porous media is governed by natural convection coupled with radiation and phase change effects. The porous structure acts as an unsaturated fibrous medium where airflow and heat transport obey generalized Darcy and non-Darcy type models that were discussed before. Due to low permeability and high anisotropy, buoyancy-driven flows and surface evaporation play a significant role, making classical saturated models only partially applicable (Nield and Bejan, 2013).

Nevertheless, convection occurs due to the bulk motion of fluids inside the fuel bed; in many cases, this fluid is naturally air. This behavior depends on porosity, since a greater void volume allows fluids to move more easily, affecting both the average and seepage velocity. This mode of heat transfer is of great importance alongside radiation, these mechanisms are responsible for producing the gasification of the solid in wildfire flame propagation (Fernandez-Pello, 1994). Conversely, convection can have two widely different influences in fires: it can either act as a cooling factor by counteracting radiative heating, or it can supply additional heat to the fuel bed. Therefore, variations in convection mechanisms can directly affect the heating processes in fuel beds (Niioka et al., 1981), impacting how heat propagates and potentially leading to auto-ignition phenomena.

In porous materials, the small distance between particles, attributed to the voids in the porous medium, impedes heat conduction significantly. Hence, convection plays a significant role due to the permeability of the medium, which is crucial for fire spread (J. L. Torero, 2016). Additionally, radiation contributes to heat transfer through the absorption and scattering properties of the porous medium. Therefore, it can be discerned that convection and radiation are the predominant mechanisms of heat transfer. In this sense, common properties such as SVR influence cooling due to increased surface area, while higher radiation can be absorbed more effectively, hence, cooling can occur on one side of the fuel bed while radiant heating affects the opposite side (Thomas et al., 2017).

In wildfire scenarios, convective heat transfer and the development of boundary layers within both the solid and fluid phases play a central role in governing flame spread. These mechanisms drive the local heating, ignition, and transition to flaming combustion within porous fuel beds. However, under the assumption of LTE, where the temperatures of the gas and solid phases are considered equal, the energy exchange between phases is inherently simplified (Grishin, 1997). As a result, the thermal transport is primarily represented by advection and radiation, while phase specific convective contributions are no longer explicitly resolved.

This modeling approach assumes a homogenized temperature field within the porous domain, which is most valid at moderate heating rates or near critical external heat flux conditions. In such cases, detailed modeling of phase dependent boundary layer behavior becomes unnecessary, and advection becomes the dominant convective mechanism considered (Simeoni et al., 2012). This simplification has been shown to hold particularly in experiments where increased airflow leads to a reduction in the heating rate, thereby supporting the LTE assumption and emphasizing the role of advective transport over more complex convective flow structures.

2.5.3 Radiation

The last mode of heat transfer within a porous medium is radiation. The goal here is to present the ideas that are based in this field, but the mathematical approach will be in regular notation and not in the notation used in continuum mechanics (Lai et al., 2010). Radiation is the heat transport by electromagnetic waves, and it does not necessarily need a medium to travel, so it can move through empty space (e.g. in a vacuum). Therefore, radiation in porous media consists in how this electromagnetic radiation moves through a media that consists in materials with pores, or voids, and, in this sense, this collection of energized particles interact with these kind of arrangements (e.g. solid matrices) (Kaviany, 1995). The interaction of this heat transfer mode with this medium is with the collection of elements in the solid matrix and the effects it has with fire phenomena, this has had a huge impact in several studies for combustion and ignition. The energy balance on radiative energy consists of an integro-differential equation which has the following general behavior of conservation principles according to (Modest and Mazumder, 2022):

$$\begin{aligned}\Delta \text{ Radiative Energy} &= \text{gain due to emission} - \text{loss due to absorption} \\ &\quad - \text{loss due to outscattering} + \text{gain due to inscattering}\end{aligned}$$

This energy balance can then be mathematically proposed with the general equation for radiative transfer, this is the Radiative Transfer Equation (abbreviated as RTE) and is defined as:

$$\frac{\partial I_\lambda}{c\partial t} + \frac{\partial I_\lambda}{\partial x} = \kappa_\lambda I_{\lambda b} - \kappa_\lambda I_\lambda - \sigma_\lambda I_\lambda + \frac{\sigma_\lambda}{4\pi}\int_\Omega I_\lambda \Phi_\lambda d\Omega \qquad (2.17)$$

Here, not only both extinction coefficients are present, but also the very important scattering phase function Φ_λ, therefore the RTE correlates variables that depend on: time, position, wavelength, and solid angle Ω, making it an extremely difficult problem to solve analytically. Further can be done to the previous equation (i.e., for biomass in wildland such as pine needles) and this changes the general RTE towards the more specific form of the RTE. For most engineering applications, the differential term consisting of the speed of light and the time derivative, $(1/c)(\partial I_\lambda/\partial t)$, can be neglected due to the large magnitude of the speed of propagation c in $dx = c\,dt$ (Özisik, 1973). Moreover, the emission $\kappa_\lambda I_{\lambda b}$ can also be disregarded considering that the sample is an opaque material that does not emit a black body radiation. These changes and simplifications yield the RTE in the form of:

$$\frac{dI_\lambda}{dx} = -\kappa_\lambda I_\lambda - \sigma_\lambda I_\lambda + \frac{\sigma_\lambda}{4\pi}\int_\Omega I_\lambda \Phi_\lambda d\Omega \qquad (2.18)$$

Therefore, to solve the RTE, the optical properties of the material under investigation must be known. These properties, usually transmissivity and reflectivity, are analyzed to retrieve relevant information for the RTE based on the underlying radiative phenomena specific to the system (Acem et al., 2010; Dombrovsky et al., 2018). In addition, for both Equations 2.17 and 2.18, the phase function can either be omitted with the convenient assumption of the entire intergal equal to one for isotropic scattering, which is an approximation that is not representative in most cases, or it can be explicitly modeled for the case under study. Therefore, the use and form of the phase function strongly depends on the nature of the sample, as this function is particle specific. Several phase functions exist, a commonly used phase function is the Henyey-Greenstein phase function, where inscattering and outscattering can be characterized for solving the RTE. This emphasizes the idea found in scientific literature that for solving the RTE in anisotropic media this value is widely unknown for several studies (Hendricks and Howell, 2006)

Radiant heat transfer in porous media propagate and strictly depend on porosity of the media and the intrinsic geometrical qualities (Vaz et al., 2004). Nowadays, this has been applied to porous media, specifically in wildland fuels (Parot et al., 2022). Despite this, the most intricate part of Equation 2.13 is the divergence of the radiant heat flux, $\nabla \cdot \dot{q}''_{rad}$, where, to get it, the RTE must be solved. Conversely, this heat flux vector (which represents the net emission or net absorption of radiation) and the aforementioned RTE are mathematically related to one another by the following equations:

$$\nabla \cdot \dot{q}''_{rad} = 4\pi \int_0^\infty \kappa_\lambda I_{\lambda b}\, d\lambda - \int_0^\infty \kappa_\lambda \left[\int_{4\pi} I_\lambda d\Omega \right] d\lambda \tag{2.19}$$

$$\nabla \cdot \dot{q}''_{rad} = - \int_0^\infty \kappa_\lambda \left[\int_{4\pi} I_\lambda d\Omega \right] d\lambda \tag{2.20}$$

Equation 2.19, where the gradient represents net emission and absorption of radiation (i.e., per unit volume or per unit area depending on the context), is referred to as the equation for the conservation of radiative energy, which does not depend of scattering (Özisik, 1973). This is not a surprising fact since scattering only redirects the stream of electromagnetic waves, it does not affect the energy within any volume of control. Thus, for a non emitting medium the mathematical relation is reduced to Equation 2.20, where only absorption accounts for the conservation of radiative energy. For further simplification of the previous equations, for purely radiative heat transfer, the gradient in one dimension is simply equal to $C(z)$ which is a function of position and time that contains distributed energy. For radiative equilibrium, then again in one dimension, implies that the heat flux remains constant at all depths. Both equations are shown bellow:

$$\frac{d\dot{q}''_{rad}(z)}{dz} = C(z) \tag{2.21}$$

$$\frac{d\dot{q}''_{rad}}{dz} = 0 \tag{2.22}$$

Underlying much of the preceding discussion on radiation is the fact that most attempts to solve the RTE rely fundamentally on approximations of some kind, particularly through expressions in the form of exponential functions with effects in overall thermal conductivity of the porous medium (Simeoni et al., 2012). Moreover, various research studies over many decades have carried out methods to solve for the RTE problem and have used procedures such as: spherical harmonics, discrete ordinates, Schuster-Schwarzschild approximations for Cartesian geometries (Hernández et al., 2019; Parot et al., 2022), and Monte Carlo simulations (Modest and Mazumder, 2022). Furthermore, an interesting but ill-posed attempt to solve RTE problems is with inverse techniques to retrieve information to then give a comprehensive solution for the general equation (Baillis and Randrianalisoa, 1996). The inverse problem techniques in engineering are considered ill-posed since it does not fulfill: existence, uniqueness, and stability of the solution (Beck et al., 1985). This implies that these solutions are highly unstable and small errors can lead to large miscalculations that lack physical meaning.

Nonetheless, while solving the full RTE remains a complex task, one aspect that can be addressed with high accuracy is the definition of appropriate boundary conditions and the use of simplified fuel bed structures to characterize specific features of the problem under study. A key advancement in this regard is the observation of an exponential decay in radiant heat flux, which is well understood. Focusing on this aspect of the RTE is particularly relevant in wildfire studies, so that radiation influence, absorption and scattering coefficients for the biomass involved in fires is fully known. Understanding and quantifying extinction coefficients allows for more accurate estimation of radiative attenuation, a key factor in the pre-heating and ignition of fuels in wildfire scenarios that is not fully known for biomass porous materials involved in wildfires.

2.5.3.1 Extinction Coefficients

The light that moves through the medium experiences perturbations when interacting with solids and gases, leading to attenuation phenomena. This is denominated in many scientific literature as radiative transfer in participating media (Modest and Mazumder, 2022; Özisik, 1973). Most importantly, these perturbations result in a reduction of radiation intensity as it encounters particles belonging to the media along its path. Thus, any incident light beam that participates in the medium will be attenuated by absorption and scattering in it. In consideration of this aspect, the attenuation of the light beams in this direction travels in beams of electromagnetic waves with a well defined straight direction that is with a negligible divergence. This beam of collimated light is also known as a pencil of rays, which are approaching the media following a single solid angle direction (Modest and Mazumder, 2022). This general concept for the radiative travel is firstly considered for constant refractive index, at stationary conditions, and in a LTE. Then, the absorption of light beams is directly proportional to the incident energy and also to the infinitesimal distance dx, if the direction in which photons move towards the media is denoted as the vector $\hat{x}$, then Equation 2.23 shows the attenuation according to the theory suggested by (Modest and Mazumder, 2022).

$$dI_x = -\kappa_\lambda I_x dx \tag{2.23}$$

Here, κ_λ is the linear absorption coefficient of the media, and the right-hand side denotes a negative sign which means that the radiation intensity of photons decreases as it penetrates the media. Therefore, as the media is with more particles (i.e., with a higher packing ratio or with a lower porosity), the light has an attenuation according to this and the bigger the thickness of the media the more difficult the passage. Alternatively, integration of Equation 2.23 yields the intensity as a function of distance, the exponential factor denotes the general behavior for the linear absorption implying that the function is in the form of Equation 2.24. This was originally known as Beer's Law, consequently the law suffered some alterations which led to this actual form, now carrying the name of Bouguer-Beer-Lambert Law (Mayerhöfer et al., 2020).

$$I_x = I_0 e^{-\int_0^x \kappa_\lambda dx} \tag{2.24}$$

Alternatively, this law can be expressed in terms of the radiative property of transmissivity, this accounts for the fraction of incident electromagnetic waves that is transmitted across the interface. Hence, this is just a ratio of the detected intensity I_x with respect to the reference intensity I_0 and it is denoted with the variable τ as Equation 2.25 shows (Howell et al., 2015).

$$\tau = \frac{I_x}{I_0} \tag{2.25}$$

Then, attenuation can also occur due to scattering in a very similar behavior as absorption, the only difference between both is that absorbed energy is transformed into internal energy, whereas scattered energy is quite simply redirected (Modest and Mazumder, 2022). Thus, the scattering coefficient is considered by the physical constant of σ_λ towards all other possible directions. This implies that the compatibility among the two coefficients are correlated by a total attenuation, this is known as extinction, where all variables in the following equation are in m^{-1}:

$$\beta_\lambda = \kappa_\lambda + \sigma_\lambda \tag{2.26}$$

The fundamental schematic for the phenomena of absorption and scattering is shown in Figure 2.8, where also the components of Equation 2.24 can be appreciated as light is emitted towards the participating media and traverses an arbitrary length until it is either attenuated or not.

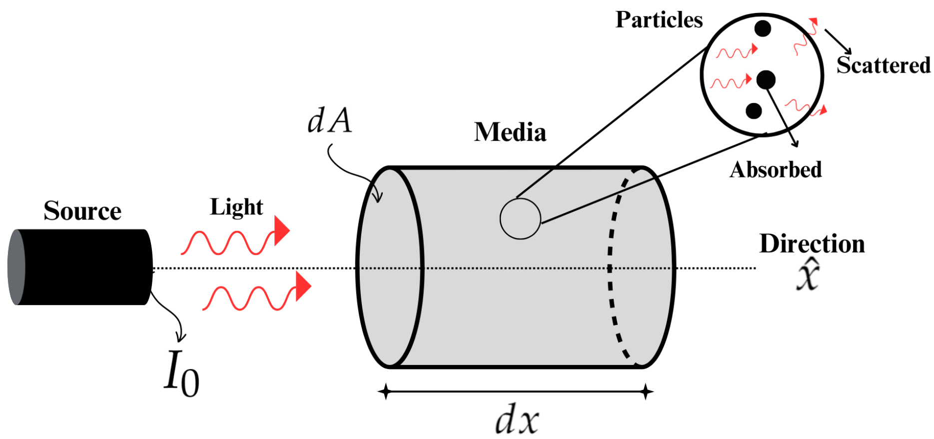

Figure 2.8: Attenuation schematics of radiative intensity.

Radiative transport theory predates the formal development of fire safety engineering, which began to evolve significantly in the mid-twentieth century. A foundational contribution to the characterization of radiation in fire problems was made by chemical engineer and co-founder of the Combustion Institute Hoyt Clarke Hottel. His early work on heat transfer laid the groundwork for the definition of extinction coefficients relevant to combustion and wildfire applications used in many practical calculations (Hottel, 1954).

In particular, Hottel derived analytical expressions for radiative absorption based on geometric optics principles, applied to particles of various idealized shapes commonly encountered in fire scenarios (Committee on Fire Research, 1961). His findings demonstrated that several geometries, such as spheres, long circular rods, square rods, thin flat plates, and strips, share a common factor: the effective radiative area corresponds to one fourth of their random projected surface area with respect to their surface area. This correlation stems from the treatment of radiative interactions purely through geometrical and mathematical means. This is characteristic of the geometric optics theory for electromagnetic wave behavior for heat transfer (Fu and Hsu, 2008; Tang et al., 1996). The findings for the analytical expressions are seen in the next table:

Table 2.6: Radiation geometry of different shape particles

Shapes	**Surface Area (a)**	**Random Projected Area (A)**	**Ratio (A/a)**
Sphere	πD^2	$\pi D^2/4$	$1/4$
Long Round Rods	πDL	$(\pi/4)DL$	$1/4$
Long Square Rods	$4DL$	$0{,}881DL$	0,22
Long Thin Strips	$2DL$	$DL/2$	$1/4$

Subsequently, Hottel formalized these results in his comprehensive text on radiative heat transfer, where he presented a simplified expression that incorporates both this geometrical factor and the particle number density and cross sectional area of the medium (Hottel and Sarofim, 1967):

$$\text{Absorption or scatter coefficient} = \int_0^{\infty} (\text{number of particles per unit volume}) \cdot (\text{cross section})\ dr \tag{2.27}$$

As a result of Equation 2.27, the final form that created the foundation for future research for extinction coefficient in the mentioned context is defined as a correlation between the surface area and their volume:

$$\text{Extinction coefficient} = \frac{1}{4} \cdot (\text{total surface area per unit volume}) \tag{2.28}$$

Consequently, after the general form to treat radiative absorption in fire research, several authors have extrapolated the investigation done by Hottel and a main source of this was done by De Mestre (de Mestre et al., 1989). Afterwards, the scientific community studying fire phenomena modified the notation into a more modern form and currently use what is known as De Mestre's equation. This notation follows the same logic, but it is now known with the surface-to-volume ratio σ and packing ratio of the particles of the medium, which yields:

$$\kappa_\lambda = \frac{\sigma\beta}{4} \tag{2.29}$$

The previous expression denotes what was described in the characterization of absorption in porous media, meaning that this attenuation coefficient can be interpreted via packing ratio and SVR to account for the porous material as the participating media described in the scientific literature. Several investigations have used this correlation and found this is an underestimation for κ_λ, where the pure geometric optics approach by Hottel indicated an idealized interpretation of nature since geometry of natural fuel bed particles does not behave exactly like this. In this fashion, since the applicability of the aforementioned equations is slightly deviated of exact values, corrections have been applied and the equation complies (Acem et al., 2009; Vaz et al., 2004; Monod et al., 2009).

Lastly, with the knowledge for the absorption coefficient, a simple characteristic of the interaction between electromagnetic waves and the porous media is the length to which the radiation is extinguished once it interacts with it. This is often called the mean free path length for radiation, this is quite simply the inverse of the extinction coefficient β_λ, or, in this specific case of absorption, the inverse of the value of Equation 2.29 or of κ_λ. This quantity is denoted with δ in meters and is given by:

$$\text{Extinction coefficient:} \quad \delta = \frac{1}{\beta_\lambda} \tag{2.30}$$

$$\text{Absorption coefficient:} \quad \delta = \frac{4}{\kappa_\lambda \sigma} \ \text{ or } \ \delta = \frac{1}{\kappa_\lambda} \tag{2.31}$$

Finally, since these expressions depend on both the geometry and the physical characteristics of the fuel, it is essential to assess how well they apply to specific biomass commonly found in wildland environments. This evaluation is particularly relevant for characterizing the behavior of individual vegetation samples, and remains an open research area due to the limited experimental evidence currently available in relevant literature.

Chapter 3

Experimental Work

3.1 Instrumentation Specifications

The investigation primarily focuses on characterizing transport in porous media for wildfire related applications. Hence, this experimental work aims to measuring the following key aspects involved in this theme, including: permeability, absorption coefficients, thermal inertia, conductivity, specific heat capacity, density, transmissivity, reflectivity, and temperature profile distributions with and without pyrolysis. Understanding these physical properties in the selected porous materials is fundamental to comprehend more deeply how are these behaviors related to wildfires.

To reach these goals, a variety of experimental setups were employed to reach these objectives, through the utilization of a permeability measurement device, a radiative transfer bench scale setup, thermal inertia device, an FTIR spectroscopy system, and a cone calorimeter. Each approach follows an specific methodology and experimental design to ensure accurately every desired parameter. Once all experimental procedures are thoroughly understood, the experimental results will be presented in accordance to what was described in the present chapter.

3.1.1 Permeameter Apparatus

In accordance with previous research conducted at Universidad Adolfo Ibáñez (Pessoa, 2019), the same principle was applied in this experiment to design and construct a square cross-section permeameter apparatus aimed at measuring the permeability of porous media. The primary distinction between the earlier research and this study lies in the scale of the new permeameter. The newly built apparatus is significantly larger, allowing for the accommodation of larger porous media and the examination of denser fuel beds. This novel permeameter enables the testing of natural porous media such as *Pinus radiata*, thereby providing the fire research community with more accurate and realistic permeability measurements. The choice of geometry for the apparatus warrants discussion, as alternative geometries could have been selected. However, a square cross-sectional area was chosen because it allows elongated porous elements to fit precisely, facilitating accurate permeability experiments.

The complete setup is integrated with the following; air comes from a general purpose air compressor which compresses air from the outside ambient, where afterwards three Water Separator model AMG from SMC Corporation remove 99 % of the moisture in air. A valve reduces the pressure of air from 8 bar to 2 bar, so that a mass flow controller EL-FLOW Select model F-203AV-M50-RGD-55-V can adequately work with an E-8000 Digital Readout Control system, both from Bronkhorst, which allow to precisely move specific masses of dry air. The Permeameter is equipped with a differential pressure meter PCE-PDA 01L from PCE Instruments with a pressure range of ±200 Pa and a resolution of 0,01/0,1 Pa to obtain the pressure drops within the test zone (which has a higher resolution that the procedures of Pessoa, 2019). All main components of the air flow passage in the setup is shown below:

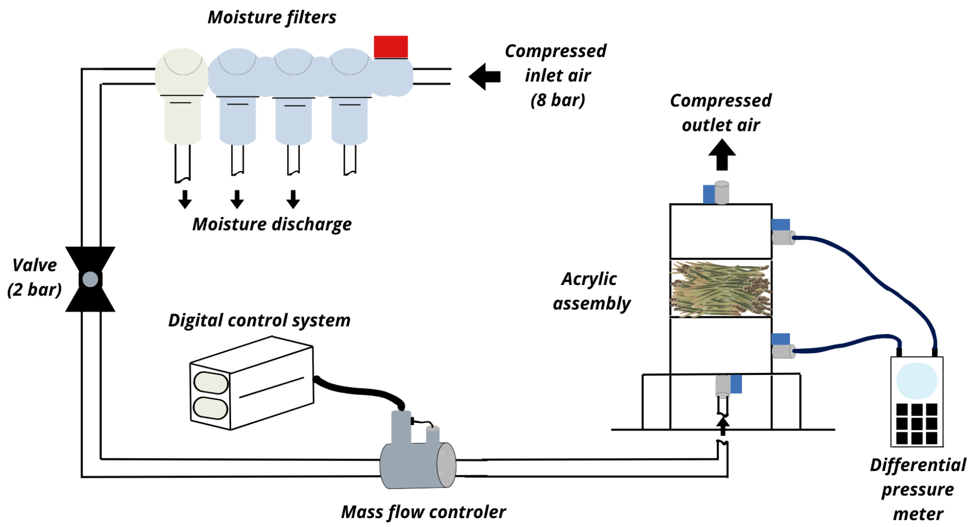

Figure 3.1: Schematic of air flow for the Permeameter Apparatus setup components.

In this setup, samples are carefully positioned within the receptacles to facilitate experimentation. The Permeameter is designed with transparent acrylic material with a 5 mm thickness, where all parts of the apparatus have square cross-sections, and each section consist of flanges with holes for secure fastening of every component using bolts. Therefore, the entire test section of the permeameter is 250 × 250 mm^2 and each structure has 100 mm of height. The device is meticulously assembled to eliminate any potential air leaks with the help of silicone to seal the gaps between the connections of all acrylic walls and also a thick gasket between each section, ensuring accurate measurement of the pressure difference across the samples inside the permeameter. The complete permeameter apparatus is shown in Figure 3.2, where an exploded view of the design depicts accurately each part of the vertical structure.

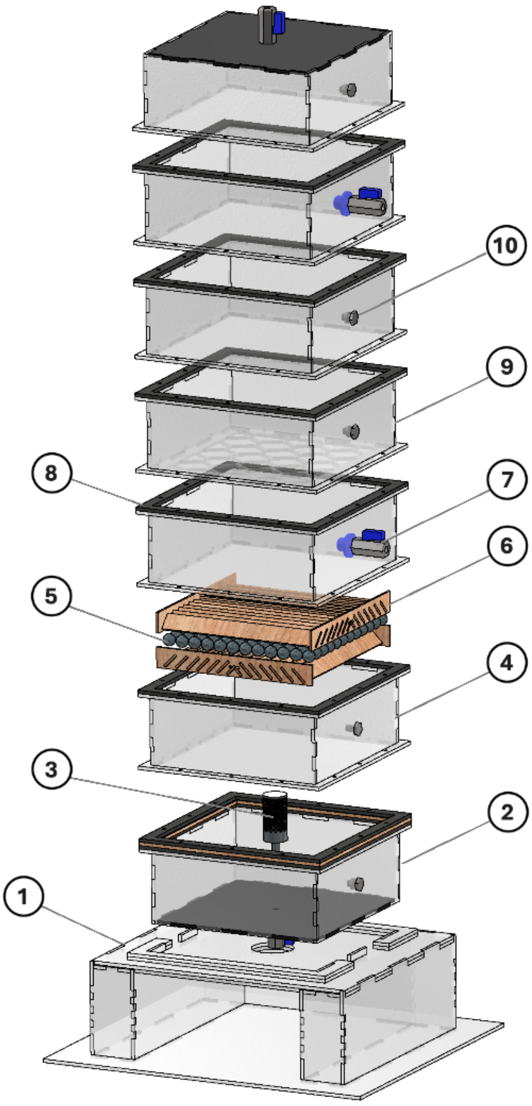

Figure 3.2: Exploded view of the assembled Permeameter Apparatus showing the specific components of the complete design.

The specific components from Figure 3.2 are enumerated as follows: base to hold the vertical sections of the permeameter ①, bottom or top section for inlet or outlet of air flow ②, air filter to dissipate the inlet jet stream of air inside the apparatus ③, intermediate sections of the structure ④, homogenizing layer of spheres for incoming air flow ⑤, wood diffusers to correct small deviations of the dissipation of the air filter ⑥, threaded nipple and valve for air passage or for pressure measurement ⑦, rubber between each acrylic component to avoid air leaks and secure all components to one another smoothly ⑧, acrylic intermediate section with honeycomb mesh with hexagonal cells to support porous samples (i.e. the surrogate fuel bed) ⑨, and finally holes for threaded nipple and valve connections where if not in use a simple bolt secures it ⑩.

The velocity profiles on the square cross-section of the apparatus need to be roughly equal for the entire active area so that it is correctly assumed that air flow strikes the porous media with the same velocity everywhere. Therefore, this was achieved with the mentioned components ③, ⑤, and ⑥. When the filter is positioned right when air enters the bottom section the air jet stream is dissipated and forcefully distributed to the sides. Then, two parallel diffusers are positioned to redirect the previously distributed air so that some fraction of the fluid is again present in the center of the cross section. Finally, in between both air diffusers there is a layer with identical spheres so that the air flow is homogeneous and uniform due to the geometrical characteristic that spheres induce in fluid flow dynamics. In this sense, after air passes through all mentioned obstacles, the stream velocity was found to be of a highly consistent uniformity when it hits the surrogate fuel beds (less than 10 % variability).

The effectiveness of the internal structures was evaluated by dividing the square cross-section into an imaginary grid of 100 points. Air velocity measurements were taken at each point for 10 different airflow rates. These local velocity measurements were then used to determine the corresponding velocity profile relative to the average flow velocity for each air flow. The accumulated error for all local velocities with respect to average velocity at each air flow is shown in Figure 3.3, where the absolute porcentual errors are depicted with their respective color map. As it can be seen, a highly uniform air flow is obtained for when it arrives at the fuel bed, where the most considerable deviation is just 6 % from the average. In this sense, every time an experiment is being carried out the inlet air is assured to be homogeneous.

Finally, the apparatus is completely set for analyzing and experimenting the permeability of porous materials, where all components of this setup work cooperatively for this goal. The final design of the Permeameter Apparatus with the relevant airflow and pressure drop connections is represented in Figure 3.4.

1%	1%	6%	5%	6%	1%	1%	6%	1%	1%
1%	6%	5%	5%	6%	5%	5%	5%	5%	5%
1%	6%	1%	5%	1%	5%	5%	5%	5%	1%
1%	6%	1%	5%	5%	5%	5%	1%	1%	1%
1%	1%	1%	5%	1%	5%	5%	1%	5%	1%
5%	6%	6%	5%	1%	1%	5%	5%	5%	1%
1%	6%	6%	5%	1%	5%	5%	1%	5%	1%
1%	6%	6%	5%	5%	5%	5%	1%	1%	6%
6%	6%	6%	1%	5%	1%	5%	1%	6%	6%
6%	1%	6%	1%	1%	1%	1%	6%	6%	6%

Figure 3.3: Local percentage error of velocity with respect to the average velocity in the square cross-section for all 10 air flows.

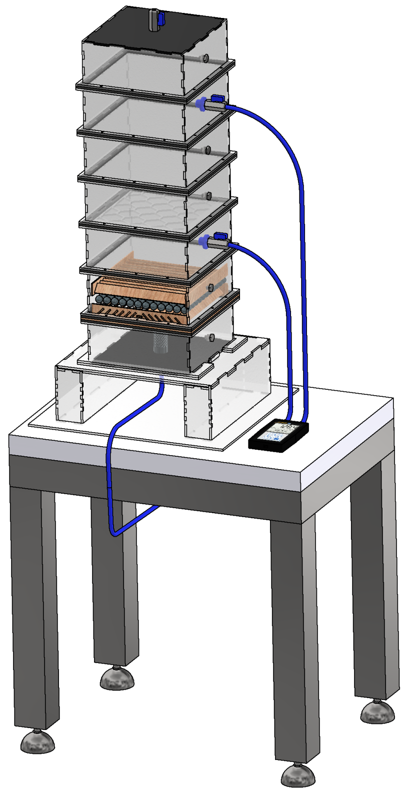

Figure 3.4: View of the Permeameter Apparatus with the specific components of the complete design for permeability experiments.

3.1.2 Radiative Absorption Setup

The simple approach for measuring transmittance of porous media, such as assessing the transmissivity of samples with known thickness, can be employed with a straightforward setup concept. The underlying principle of this experiment is that the attenuation of radiation progressively increases as it penetrates into the medium. Therefore, the basic requirements for this concept are a light source, a sample holder, and a system to retrieve the incoming light. In this context, all equipment components should just be adequately designed to be in accordance with light intensity, wavelength, angle of incidence, and focal distances. The objective is to determine the distance at which the total extinction of radiation occurs (i.e. κ_λ), signifying that the complete system should be capable of obtaining direct transmissivity (i.e. specular transmissivity).

For this aspect of the experimental work, the light absorption of porous media will be assessed with a vertical setup to be able to replicate natural conditions, with the porous sample in a horizontal orientation and subject to the correct gravitational effects. For this purpose, this concept consists of a stabilized light source that is measured once it passes through the medium, allowing to determine the variational decrease in intensity (i.e. attenuation). The intermediate section featuring a honeycomb mesh with hexagonal cells to support porous samples, described in the previous section and illustrated in Figure 3.2, can be applied for this absorption setup to support the porous samples.

The setup is equipped with a tungsten light source SLS201L/M combined with an external collimator SLS201C and a reflective neutral density filter, all attached to the lamp assembly. An achromatic lens AC508-300-AB-ML, mounted with a SM2RC/M lens tube, is used to converge light towards a photodiode DET36A2, which is adjusted with a response-flattening filter SRF15 and connected via a 2249-C-60 BNC coaxial cable to a signal acquisition device. All of the aforementioned optical equipment are mounted to the vertical structure using optical posts TR75E/M and post holders PH75/M-P5. All these components are from Thorlabs. The light detector is connected to a DSOX2012A oscilloscope from Keysight Technologies. The aluminum profiles used in the metallic structure have different lengths, but all share the same cross section of $40 \times 40\,\mathrm{mm}^2$, provided by Bosch Rexroth.

A sturdy structure holds the various components securely in place, with each element positioned to enable the detection of the absorption coefficient and transmissivity. The light source is mounted at the top, directing light beams downward toward the surrogate fuel bed. To ensure reliable attenuation measurements, the experimental conditions should remain consistent across tests. The following figure depicts the intended experimental setup designed, along side the components mentioned above.

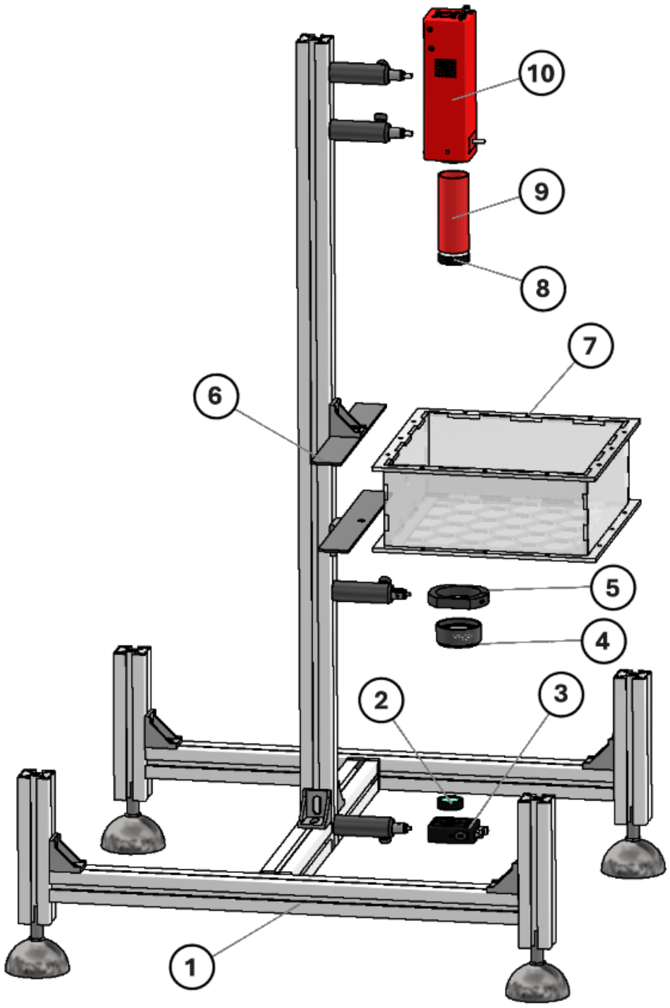

Figure 3.5: Exploded view of the absorption setup with the specific components of the complete design for radiative absorption experiments.

The specific components from Figure 3.5 are enumerated as follows: metallic structure of aluminum profiles, profile connections, adjustable leveling metal feet, and four post holders ①, flattening filter ②, biased detector ③, achromatic lens ④, optical holder ⑤, metal plaques to hold horizontally leveled the surrogate fuel bed ⑥, surrogate fuel bed for porous samples ⑦ (i.e. the same intermediate section with the hexagonal honeycomb, ⑨, from the Permeameter Apparatus in Figure 3.2), optical density filters for the light source ⑧, collimating lens for light source ⑨, and finally the tungsten lamp as the light source ⑩.

Once the radiation setup is activated, the light source requires 45 minutes to reach a stable constant power output. After stabilization, the beam is emitted towards the surrogate fuel bed, and the transmittance is measured with the biased photodetector connected to the oscilloscope. Subsequently, during the radiation absorption phase, the system directs the collimated beam towards the fuel bed, where radiation will pass through the medium, and finally the lens converges the light onto the active area of the sensor with the flattening filter as seen in Figure 3.6:

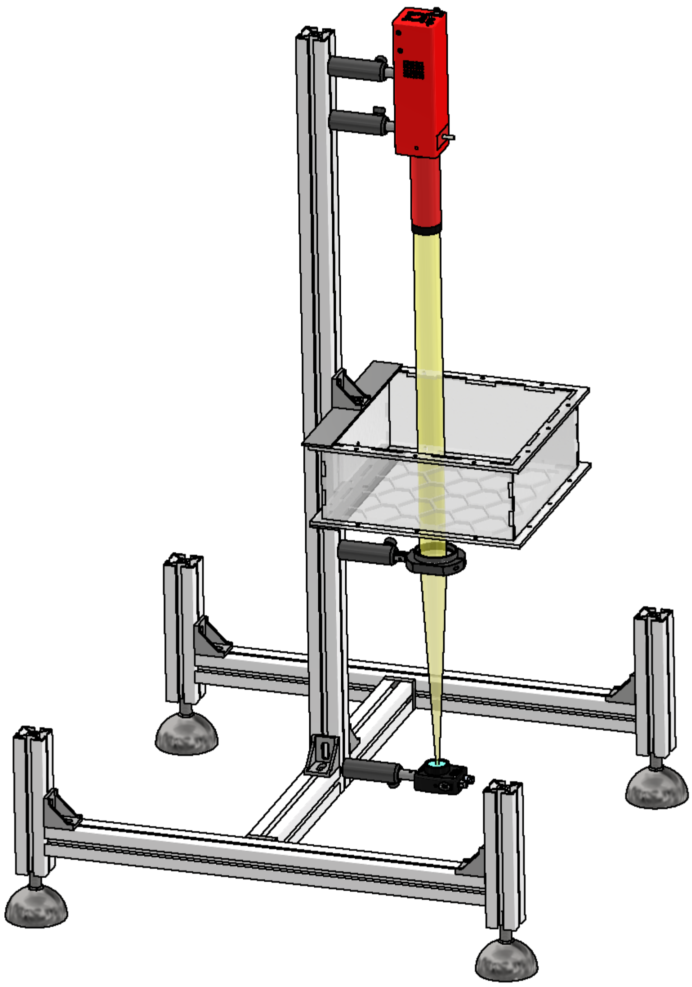

Figure 3.6: Schematic for radiation attenuation measurement of a porous medium, depicting the intended path for light in the setup.

Finally, this setup can be readily used to determine the absorption and transmittance of porous media. Its modular design, combined with the vertical orientation, vertical gravity effects, and stable optical alignments, all ensure flexibility and repeatability for experiments involving various porous samples.

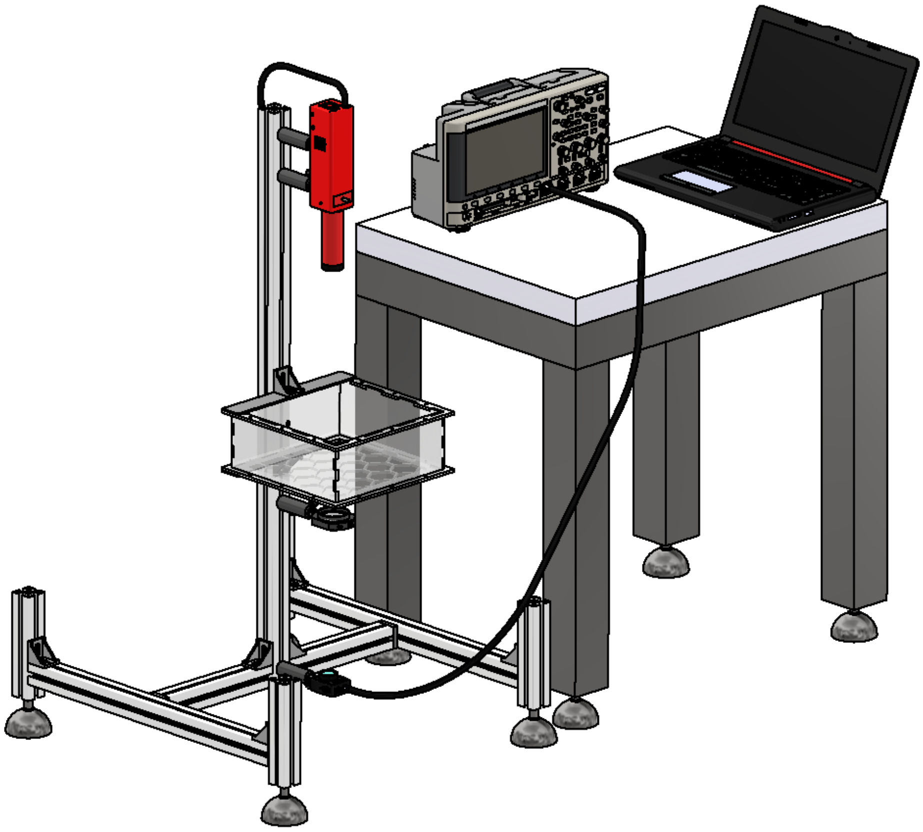

Figure 3.7: View of the Radiative Absorption Setup with all specific components of the complete design for attenuation experiments.

3.1.3 Thermal Inertia Setup

For the thermal inertia of porous samples, these experiments were done in Nancy, France, at Laboratoire Énergies & Mécanique Théorique et Appliquée (i.e., abbreviated as LEMTA) within the framework of mobility to France to complement master studies abroad financed by Institut Français du Chili and Universidad Adolfo Ibáñez. The experiment is based on a transient method to measure this property. Thermal insulators must be applied to fully enclose the sample; materials such as PVC, PEHD, or similar can be used for this purpose. To ensure appropriate dimensions for reliable measurements, the porous sample should have a size of $100 \times 100 \times 20\,\text{mm}^3$ with at least one perfectly flat surface. Therefore, the principle in question is suggested by a side view of the main schematic shown by Figure 3.8, where this small volume with air and dry porous samples interact with the heating element.

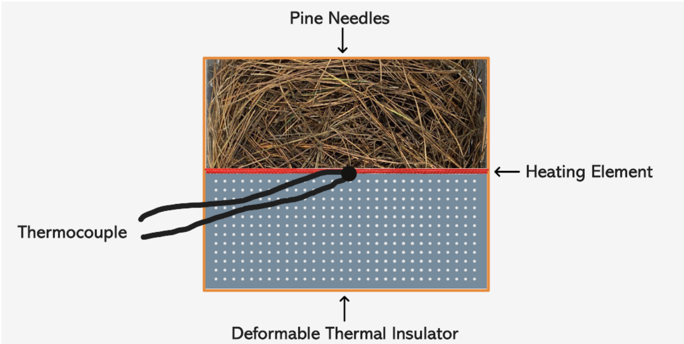

Figure 3.8: Schematic for thermal inertia measurement of a porous medium.

This is how the thermal inertia experiment is usually done, where the heating element consists of a flat asymmetric resistance of a size of $100 \times 100\,\text{mm}^2$ with a semi-infinite sample, a K-type thermocouple, polystyrene blocks of 5 cm thickness as the deformable insulator, a Picolog TC-08 datalogger to record the temperature, and an electrical generator for the stabilized power supply. The thermocouple is fixed at the center of the heating element using a $1 \times 1\,\text{cm}^2$ piece of aluminum adhesive. The side of the heating element where the thermocouple is attached is placed in contact with the (deformable) insulator to avoid creating contact resistance. The heating element can be fixed to the insulator using a very thin double-sided adhesive tape. Figure 3.9 shows a probe and a typical setup ready for experimentation.

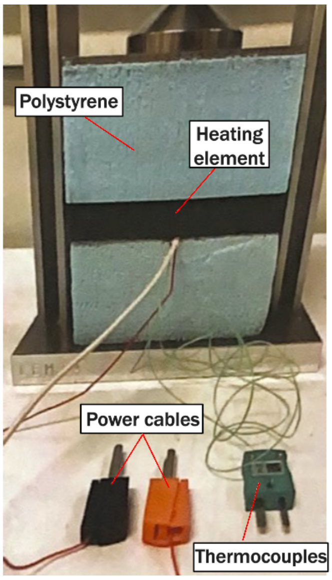

Figure 3.9: Example of probe and device final assembly to carry out thermal inertia experiments.

3.1.4 Heat Capacity Device

For the straightforward measurement of the heat capacity of pine needles, a microcalorimetry device was employed, also done in France at LEMTA. A differential scanning calorimeter, the microDSC3 from SETARAM, was used. This specific model operates up to 120 °C and incorporates a three-dimensional sensor based on the Joule effect to define heat flow.

To ensure proper functioning of the device, the samples needed to be dry; therefore, a vacuum drying process was applied beforehand. The measurement chamber consists of two cylindrical vessels equipped with Peltier elements for precise temperature control: one vessel holds the sample, while the other serves as a reference with known thermal properties. By measuring the difference in heat flow between the two vessels, the system automatically determines the amount of heat required to raise the sample's temperature which is given by a computer calculation done by the same device.

3.1.5 Oven Drying Device

In order to ensure that the samples used in the experiments do not retain significant moisture contents, which could otherwise affect the accuracy and repeatability of the measurements, a controlled drying process must be carried out prior to each testing day. This process involves subjecting the samples to a heating cycle using a laboratory grade drying oven device.

For this purpose, a precision research oven was employed to remove the inherent moisture from the fuel samples in a consistent and reliable manner. Specifically, the universal oven UN55 model manufactured by MEMMERT was utilized, which is designed for scientific and industrial applications requiring uniform and accurate temperature control. This oven allows for the setting of precise drying conditions, ensuring that all samples reach a standardized very low moisture state before undergoing experimental procedures.

3.1.6 Fourier Transform InfraRed Optical Equipment

The optical evaluation of transmissivity and reflectivity was used at Salle Carnot at LEMTA. This evaluation covered for visible and infrared electromagnetic wave spectrum ranging from the $450 - 20.000\,\mathrm{cm}^{-1}$ or roughly $20 - 0{,}5\,\mu\mathrm{m}$. These wider wavelength values are retrieved with the spectroscopy device Fourier Transform InfraRed spectrometer (i.e., FTIR), two integrating spheres and three light detectors. For this kind of measurements, the beam exiting the spectrometer is focused towards the sphere which is located after the spectrometer output where two modifiable mirrors adjust the focal point of light. The samples are either positioned at the inlet or the outlet of the sphere (i.e., for transmission or reflection respectively) where the detectors are connected to the spheres to collect a fraction of the radiative flux of the total radiation going through the inside of the sphere.

The FTIR is an IFSS66v/s apparatus produced by Bruker, where the spectrometer is built around a Michelson interferometer and with a beamsplitter made of germanium on KBr and a globar acting as the light source. One integrating sphere is tailored for mid and far infrared with gold internal coatings for a near perfect reflection of radiation (i.e., known as infragold in literature). For this sphere, the detector is of MCT type, cooled with liquid nitrogen, by Kolmar Technologies. Then, a general purpose integrating sphere from Labsphere that works for visible and near infrared radiation which is designed to directly adjust free space detectors for optical responses. For visible response, a free space biased Si detector DET36A2 is utilized, and for the near infrared one, an InGaAs biased detector APD130C, both produced by Thorlabs. The description for each component can be seen in Figure 3.10. The FTIR is also equipped with an internal sample compartment to evaluate direct transmissivity, where a group of mirrors can be adjusted for different light beam diameters. This is directly measured inside with the spectrometer and the same wavelengths can be obtained.

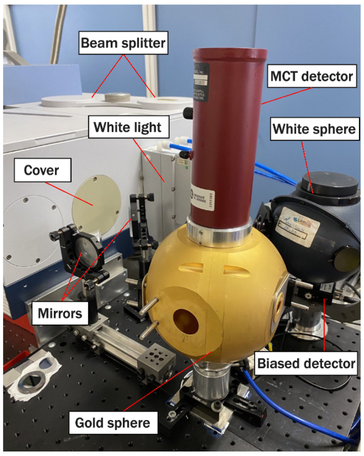

(a) External elements.

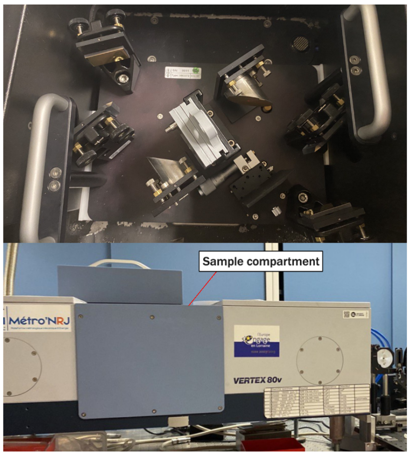

(b) Sample compartment.

Figure 3.10: FTIR setup components.

Therefore, this setup can be operated individually in certain spectral ranges, like: visible ($20.000 - 9.000\,\mathrm{cm}^{-1}$), near infrared ($11.000 - 3.000\,\mathrm{cm}^{-1}$) and finally mid to far infrared ($6.000 - 450\,\mathrm{cm}^{-1}$). Hence, to obtain the complete spectral response, all three values are just simply concatenated to merge the spectrum and reveal the complete physical behavior for the same sample. To hold the porous samples, a small 3D printed box was built to hold the media which were accommodated and compressed with small foams. In this regard, this recipient had to fit both the integrating spheres and the sample compartment of the aforementioned equipment, thus, this sample holder acting as the surrogate fuel bed can be seen in the next figure:

(a) For interior. (b) For spheres.

Figure 3.11: Sample holder for FTIR setup.

For diffuse transmissivity measurements, the entire FTIR equipment had to be operated for the outside compartment with both integrating spheres to cover the desired spectrum. The focal distance was defined for a specific beam diameter since this had to be adjusted for the porous sample that had to be in front of each sphere. This can be appreciated in both figures bellow:

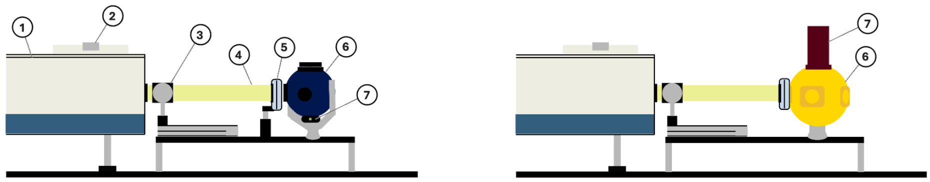

(a) Diffuse transmissivity setup, white sphere and biased detector.

(b) Diffuse transmissivity setup, gold sphere and MCT detector.

Figure 3.12: Diffuse transmissivity components positioning for experiments.

The components in use from Figure 3.12 are enumerated as follows: FTIR functioning as the light source ①, a beam splitter ②, mirrors for the modifiable focal point of the light beam that exits the FTIR ③, the beam moving towards the sample and the spheres ④, sample holder from Figure 3.11b ⑤, white or gold integrating sphere ⑥, the biased or MCT light detector ⑦. For the reference value of transmissivity, no sample is positioned.

For reflectivity measurements, the only two differences with the previous figure is that now the sample holder is in the outlet of each integrating sphere and to achieve the same light beam diameter both spheres are closer to the mirrors (i.e., at the same focal distance than before). The components are exactly the same as in Figure 3.12, hence, the positioning is the only change for these experiments:

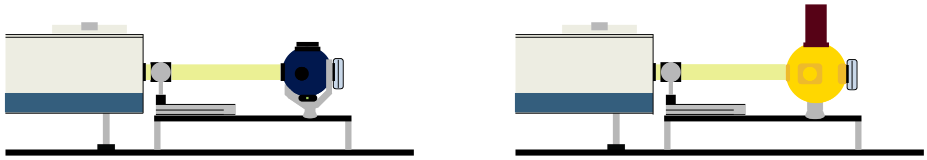

(a) Reflectivity setup, white sphere and biased detector.

(b) Reflectivity setup, gold sphere and MCT detector.

Figure 3.13: Reflectivity components positioning for experiments.

Last but not least, to account for direct transmissivity, the sample compartment had to be used and for these cases the FTIR functioned as the source and spectrometer. Here, the light beam diameter was not exactly the same as for the previous measurements, but it was roughly the same. The compartment was positioned with the sample holder shown in Figure 3.11a, in the same configuration as in Figure 3.10b, and it is illustrated in the following figure:

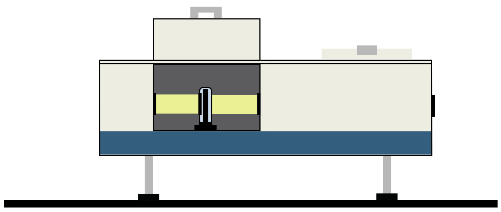

Figure 3.14: Direct transmissivity components positioning for experiments.

In summary, the FTIR setup can be reliably employed for the aforementioned procedures, ensuring that the desired optical properties are accurately measured. This confirms the suitability of the experimental configuration for conducting optical characterization of porous samples such as porous biomass under controlled conditions.

3.1.7 Cone Calorimeter System

The cone calorimeter consists of an experimental setup designed to study the influence of radiant heat fluxes towards different kinds of materials to mainly analyze combustion and decomposition of these. This setup was built and is used at the fire research laboratory at LEMTA, in Nancy, France. The heat flux is generated due to a helical coil shaped heating element, whose temperature of this element can be manually defined to achieve desired heat fluxes ranging from 0 up to $100\,\mathrm{kW\,m^{-2}}$. A Schmidt-Boelter type heat flux sensor from Medtherm (i.e. radiometer) obtains the heat flux measurement. This is placed at a distance from 2 up to 2.5 cm from the cone, and it is aligned with the center of the sample's exposed surface. The cone calorimeter is a standard device for studying a uniform heat flux towards a sample for experimental measurements for fire or thermal measurements (Pinto et al., 2025). At this experimental room there are two different cone calorimeters: one has a fixed vertical position, while the other one has a modifiable angle and can be oriented all the way to a horizontal position.

(a) Vertical position. (b) Horizontal position.

Figure 3.15: Cone calorimeter.

The purpose for the cone calorimeter for this research was focused on studying radiative in-depth penetration towards the porous sample, for this aim an insulated box made of fire resistant refractory bricks from VITCAS was designed to hold samples and it was sealed with cement board adhesive VITCAS at the bottom and along all edges to avoid any convective effects on experiments. Hence, to account for the vertical temperature distribution inside the box, 8 K-type thermocouples were positioned at different arbitrary heights. The dimensions of the designed box are, for the entire volume $14 \times 14 \times 8\,\mathrm{cm^3}$, and the internal volume to hold the sample $8 \times 8 \times 5\,\mathrm{cm^3}$.

The final composition of the insulated box built is as follows:

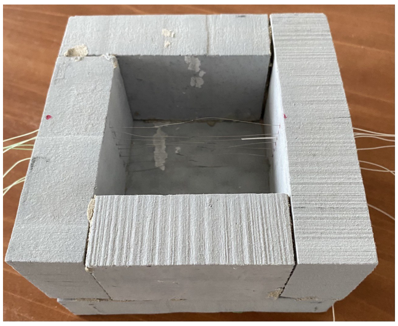

Figure 3.16: Composition of the sealed insulated box before fuel loading and themocouple tightening.

Therefore, the chosen positions for the thermocouples and their measurement points are illustrated in Figure 3.17, where six thermocouples were placed 5 mm apart over the first 3 cm, and the remaining two were spaced 1 cm apart, with the last one located at the bottom.

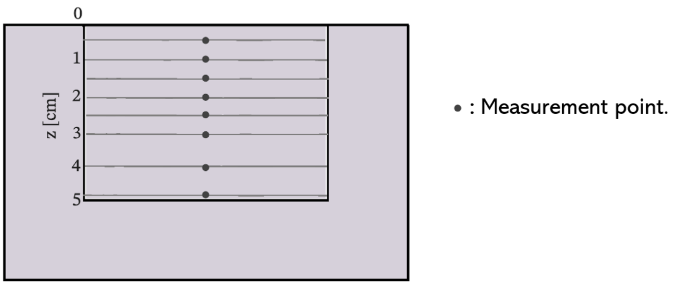

(a) In-depth thermocouple positions.

(b) Insulated box with samples.

Figure 3.17: Thermocouple and fuel positioning.

In this way, the surrogate fuel bed was configured: each thermocouple (starting from the bottom $z = 5$ cm) was first secured, and then the samples were added. This procedure was repeated as the internal volume of the box was filled, ensuring that all thermocouples were properly tightened. Once the box is filled and ready for experimentation it must be well centered and positioned in front of the horizontal cone calorimeter. Hence, the exposed surface of the box and the cone was left at the same height used for the radiometer which was determined for these experiments at 2 cm distance apart. Finally, once the box and the cone are at the desired position, each thermocouple was connected to a Picolog datalogger to register the temperature distribution. Thereafter, the only difference between the radiation penetration experiments and the fire experiment was the use of a balance to measure the mass loss rate, an electronic balance EX4202M from OHAUS was employed.

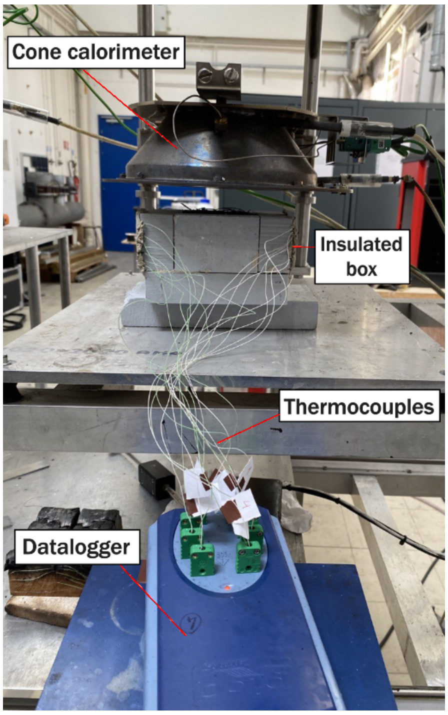

(a) In-depth radiation setup.

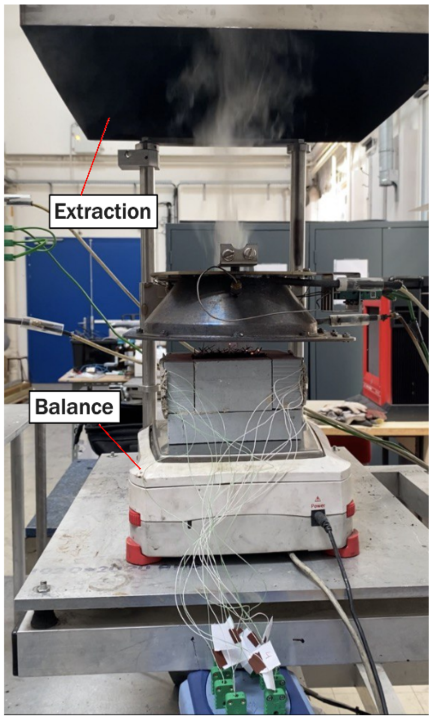

(b) Fire and MLR setup.

Figure 3.18: Cone calorimeter final experimental setups.

3.2 Experimental Design

The design of the experiments relies on all the setups and devices discussed previously. In all cases, the type of specimen remains the same, and for some it is exclusively for one kind of specimen, while various conditions of the samples like masses and bulk densities (to account for different porosities) will be explored. For each case, a methodology based on the aforementioned equipment will be thoroughly described, in order to account for the experimental design and approach that will yield the corresponding experimental results.

3.2.1 Characteristics of the Specimens

Both setups use the same materials to account for the porous media that is considered as the specimen. The specimens that are going to be used for the fuel beds are seen in Figure 3.19. The figure shows the pine needles to be studied, *Pinus radiata*, which were obtained and delivered by the Chilean national forest service CONAF. In this figure, three different conditions are shown for this biomass. Then, Figure 3.19a are the wood elements which have a square cross sectional area, these sticks will have lengths of roughly 25 cm. Only two types of cross sectional area are used, 2×2 mm, and 3×3 mm.

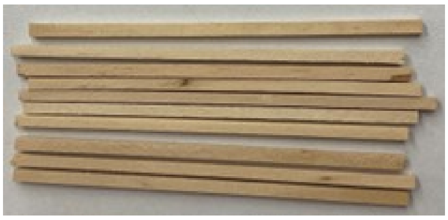

(a) Wood elements.

(b) *Pinus Radiata* experimental array.

(c) Single pine, followed by three needles.

(d) *Pinus Radiata* natural state in wildland.

Figure 3.19: Materials to study.

The choice of materials is based on the unique geometry of these pine needles, illustrated in Figure 3.19c. Each specimen typically consists of clusters of three needles emerging from a common base (i.e., the leaf head), distinguishing them from other pine species that typically feature single needles. This results in a more intricate geometry for wildfire scenarios involving this biomass. Wood elements were selected due to their similar characteristics of being thin and elongated. The varying thicknesses of different wood elements provide an interesting aspect for analysis. Moreover, both materials share comparable thermophysical properties as biomass.

Due to time constraints, the experiments will focus on these three specimens mentioned before. Upon placement in the surrogate fuel bed within both experimental setups, adjustments to porosity, packing ratio, and bulk density are achieved by compressing the medium altering the height of the volume. This flexibility allows for varying these factors, as exemplified in Figure 3.20, where for exactly the same mass the medium is widely different in terms of porosity and packing ratio:

(a) High volume and height of the medium.

(b) Low volume and height of the medium.

Figure 3.20: Different heights and volumes for the medium involved for the same mass of fuel.

The same behavior from the previous figure occurs for the wood elements, for the same mass different bulk densities can be structured, ergo, different porosities and packing ratios can be studied. The sole difference is that natural pine needles such as this one has naturally a high porosity, hence, modifying it beyond a certain threshold is complicated, whereas for wood elements the entire porosity range can be easily explored and manipulated.

The density of the specimens is estimated using a pycnometer with ethanol, where the fuel should be dry and cut into pieces so that the samples could fit inside the pycnometer. The drying process is done in an oven at 65 $^{\circ}C$ for 24 hours so that the FMC is in the range of 0 to 3% value. Therefore, the dry leaf density is done through the following steps:

1. Weight the pycnometer, m_{py}.
2. Fill the pycnometer with the required volume amount of ethanol.
3. Weight the pycnometer filled with ethanol, m_{py+et}.

4. Remove the ethanol and ensure that the pycnometer is dry (residues of ethanol simply evaporate at a quick rate).
5. weight the pycnometer with the fuel content (i.e., wood or pine needles), m_{py+s}.
6. Fill pycnometer with ethanol to obtain $m_{py+sample+et}$, note that the volume required here is less in this case.
7. Final density calculation yields:

$$\begin{aligned}
m_{et,full} &= m_{py+et,full} - m_{py} \\
m_{et} &= m_{py+f+et} - m_{py+f} \\
V_{et} &= \frac{m_{et}}{\rho_{et}} \\
V_T &= \frac{m_{et,full}}{\rho_{et}} \\
V_f &= V_T - V_{et} \\
m_f &= m_{py+f} - m_{py} \\
\Rightarrow \rho_f &= \frac{m_f}{V_f}
\end{aligned}$$

Conversely, the process gives values for more repetitions and the results gives an estimated value for the density of the sample. Note that the density of ethanol is supposed to be known, and it is given as $\rho_{et} = 789\,\mathrm{kg\,m^{-3}}$ for this calculation. A total quantity of 100 repetitions are contemplated for ρ_f.

3.2.2 Permeability Measurements

The main outcome of the Permeameter Apparatus is fundamentally to determine the permeability K of the media studied. This value can be understood as the response of the system, and this response depends on a number of factors. For this setup, the factors involved are the air flow velocity u_D, since for very low velocities Darcy regime is present, but for increasing velocities non-Darcy regime appears. The velocity of the air is controlled with the mass flow controller, therefore, an obvious procedure is to evaluate the lower velocities first and then move to higher ones. The dynamic viscosity μ can be considered as a fixed factor, since the dynamic viscosity is from the incoming air from the test conditions of temperature and ambient pressure. With this, according to the regime in which the flow is being developed, the last measurements are just for different pressure drops at the pressure taps which are at an arbitrary distance from one another. Each time, two pressure values (i.e., for the difference $dP = P_2 - P_1$) are measured by the differential pressure meter. Given this data, the estimation for permeability of the specimens are by a modified Forchheimer equation as suggested by (Nield and Bejan, 2013, Fehrmann et al., 2017), where Equation 2.7 is then expressed as:

$$-\frac{dP}{dx} = \left(\frac{\mu}{K}\right) u_D + (\beta_F \rho)\, u_D^2 \tag{3.1}$$

Subsequently, an experimental run is conducted under specific conditions (i.e., setting the porosity of the sample to a fixed value) and using two pressure taps. The flow rate is initially set to a small value and then incrementally increased to a predetermined maximum to fit Equation 3.1 with the independent variable. This pertains to adequately fixing the air flux in the controlling device to the values of 5, 10, 15, 20, 25, 30, 35, 40, 45, 50, 55, 60, 65, 70, 75, 80 L/min, all with an uncertainty of $\pm$ 0,2 L/min because of small instabilities coming from the external air compressor used. Hence, for the calculation of the values of Darcy velocities this volumetric air flows are just transformed into SI units and divided by the free area of the intermediate section with a honeycomb mesh of the apparatus, consisting of exactly 0,041 m^2. Subsequently, a second-order polynomial fitting method is applied to the scattered data from all of these measurements, and the behavior of the increasing velocity is plotted and fitted to this polynomial. This allows for the mathematical determination of the coefficients of a rewritten Forchheimer equation from the polynomial fit calculated. This is in the form of the following equation which is clearly analogous to Equation 3.1:

$$y = A \cdot u_D + B \cdot u_D^2 \tag{3.2}$$

Thus, the equation is employed to determine coefficients A and B within the second-order polynomial that fits the retrieved data, which are derived from variations in velocity and pressure gradients. Consequently, the identification of these parameters is facilitated through this approach, signifying that the relevant permeability value can be directly solved as follows:

$$K = \mu / A \tag{3.3}$$

Finally, the factors in the experimental design for the response being the permeability are the following: bulk density of the porous medium which controls the porosity of the samples, packing ratio which is controlled with the total volume of the porous medium, different masses for the media used, and increasing velocity. Therefore, the response of the experimental design is shown in Figure 3.21, where all factors that affect permeability are clearly the pressure gradient between each pressure tap dP/dx, velocity variation u_D, bulk density ρ_b, packing ratio β, and the mass of the specimen in use m_f.

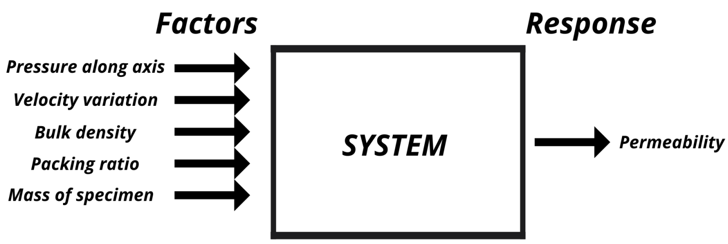

(a) All factors affecting permeability.

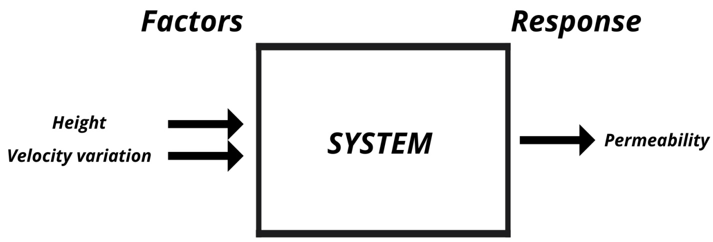

(b) Modifiable factors affecting permeability for fixed runs of experiments.

Figure 3.21: Main factors for the experiment runs for permeability.

Since for the desired response of the system has many factors that affect the outcome, the logical way of understanding the design of the experiment is through only a variation of height of the specimen and the velocity variations for a fixed mass, because bulk density and packing ratio depend on the volume (i.e., more height of the sample means more volume, meaning that ρ_b and β are higher), and quite simply maintaining the other factors constant for each separate experimentation can ensure consistency in other experimental conditions that ensures systematic investigation of the variables.

Conversely, once the pressure gradients are determined with the aforementioned procedure, additional relevant data is considered. For one, the viscosity of air with respect to the ambient temperature can be considered constant, but climate conditions can variate this value. This can be easily approximated with Sutherland's Law shown in Equation 3.4 (White, 2016). For this calculation, standard reference values are obtained through International Standard Atmosphere model (abbreviated as ISA) of the atmosphere of Earth, these values are $1{,}789 \cdot 10^{-5}\,\text{Pa} \cdot \text{s}$ for air viscosity μ_0 at 288,15 K, temperature T_0 of 288,15 K at sea level, and $S = 110$ K for the constant of Sutherland. With this, extremely precise values can be obtained for μ, since it is involved in Equation 3.3 and considering a single value for all experiments (regardless of being done in the same day) can affect this result. In this context, among the two remaining variables, the experimental temperature T is obtained with the differential pressure meter, whose sensors provide both pressure and temperature data. Consequently, Sutherland's Law is given as follows:

$$\frac{\mu}{\mu_0} = \frac{(T/T_0)^{3/2}(T_0 + S)}{T + S} \tag{3.4}$$

Then, to accurately determine the air density at a given temperature and altitude, derivations from the Toussaint formula and the equation of state of gases provide an expression to compute the density (Anderson, 2016). Therefore, the model used is an approximation of the temperature dependent density, as given by Equation 3.5, where $R = 287\,\mathrm{J\,kg^{-1}\,K^{-1}}$, the reference ISA density and temperature is $1{,}225\,\mathrm{kg\,m^{-3}}$ and 288,15 K for ρ_0 and T_0 respectively, local gravity acceleration g is $9{,}80665\,\mathrm{m\,s^{-2}}$, and the lapse rate in the troposphere is $a = 0{,}0065\,\mathrm{K\,m^{-1}}$:

$$\frac{\rho}{\rho_0} = \left(\frac{T}{T_0}\right)^{-(g/aR)-1} \tag{3.5}$$

Furthermore, for an exact value of a Reynolds number, the characteristic length of the samples has to be calculated as an equivalent value given by the hydraulic diameter, this is a straightforward formula given by the widely known:

$$L_c = \frac{4 \cdot \text{area}}{\text{perimeter}} \tag{3.6}$$

Finally, according to each experiment, it will consist of modifying the height of the specimen and the air flow velocity, leaving all other factors constant. This implies that experiments must be done for different: masses for the porous medium, heights of the specimen, and velocities. For the context of this research, three masses will be explored having specimens with low mass, medium mass, and high mass. Each will be with one pressure gradient which is justified due to the high resolution of the manometer in use. Lastly, the velocity increase is going to be for three heights of specimen, meaning three different porosities and packing ratios. This gives a total of three masses, one pressure gradients, and three heights with velocity increase, resulting in 15 runs. For variability, each situation is going to be repeated three times, meaning that a total of 45 runs for each specimen is going to be done, which is 135 experiments on permeability for all specimens involved.

3.2.3 Extinction Coefficient Measurements

The main outcome for the radiative absorption setup is to determine the absorption coefficient κ_λ of the media studied. In this sense, now the response of the system is fundamentally to obtain the value at which no more light can go through the porous medium. The factors involved for this measurement are light source intensity I_0, light intensity that passes through I_x, packing ratio β, surface to volume ratio σ, and the mass of the fuel m_f. In this experimental design, the source intensity, fuel mass, and surface-to-volume ratio remain fixed. The variable under study is the packing ratio, which is determined by the height of the volume. A greater distance between the surfaces at the top and bottom of the volume affects the packing ratio, thereby influencing the measurements. Hence, the modified version of Equation 2.24 from (Modest and Mazumder, 2022) is employed in a consistent manner as utilized by (Vaz et al., 2004, Thomas et al., 2017), which yields the following linearized equation:

$$\ln I_x = -\kappa_\lambda \cdot \Delta x \, + \, \ln I_0 \tag{3.7}$$

In this manner, Equation 3.7 is now just a simple formula without integrals to solve for the extinction coefficient κ_λ with a linear simple equation where the slope directly gives this absorption value. Thus, as the height and volume of the specimen increase, the light intensity measured by the detector decreases. This relationship is directly observed and recorded using an oscilloscope. Thereafter, the simple equation $y = m \cdot x + c$ is solved for the slope, $m = \kappa_\lambda$, determining the absorptivity. Alternately, just using the direct measurement of both intensities mentioned before, the transmissivity is directly determined through Equation 2.25 and directly solve the Bouguer-Beer-Lambert Law for κ_λ. Both procedures are mathematically related, therefore, the same.

Subsequently, measurements using the aforementioned simple equations are complementarily compared with results obtained from the extinction coefficient equation $\kappa_\lambda = \beta\sigma/4$. In this way, two parallel forms of obtaining the same value are done, through which error margins will be obtained and correction factors will be accounted to analyze the divergence between both as previous authors have done (Vaz et al., 2004, Monod et al., 2009). This is in strict relation of the specific specimen used and the correction factors are due to the underestimation mentioned for the theory behind Equation 2.29 in the previous chapter. In this sense, total transmisivity of the media is measured, for different heights and, of course, this means that also for different packing ratios. All data is determined only for visible and near infrared spectrum. Figure 3.22 shows the factors affecting the response of the light absorption system.

Therefore, surface to volume ratio, mass of the specimen, and light intensity are fixed for each run, signifying that the height is the factor to modify when all others are constant. Accordingly, by varying the height, the light intensity must decrease due to an increase in light absorption. In this sense,

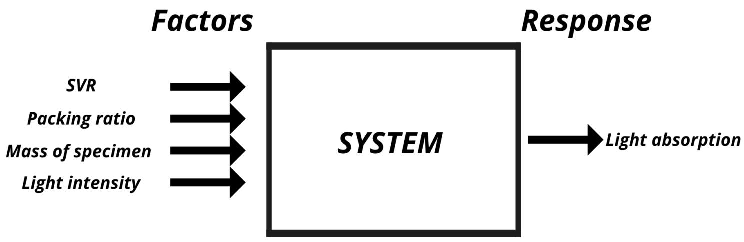

(a) All factors affecting light absorption.

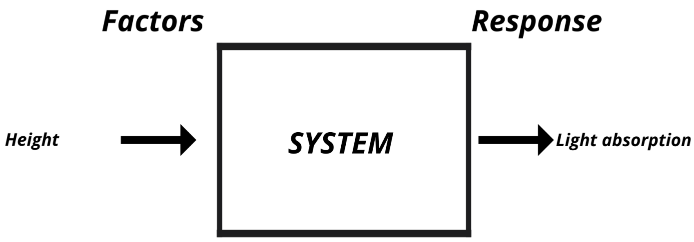

(b) Modifiable factors affecting light absorption for fixed runs of experiments.

Figure 3.22: Main factors for the experiment runs for light absorption.

the design of the experiment consist on performing each experiment with ten different masses where the mass will be increased each time to provide more volume, each mass will have three different packing ratios meaning that three different heights will be tested for each mass. This gives a total of 30 runs for each specimen, therefore, this gives a total of 90 runs of experiments. A note on these experimental runs is that they are much faster than the permeability tests, since it is just compressing the porous media, adding more mass, and obtaining one single result as a value.

3.2.4 Heat Capacity Procedure

The standard procedure with respect to the specific microcalorimetry device is as follows:

1. The initial temperature has to become stable at $15° C$ for at least 25 minutes.
2. The temperature is then incremented at a constant rate for 10 minutes.
3. The temperature from the previous step is held steady for 15 minutes.
4. Finally, steps 2 and 3 are repeated as many times as needed to cover the desired temperatures to determine.

Due to calibration defects of the device, available temperature range to test for the samples was limited to a maximum of 60° C, therefore the testing intervals for the specific heat capacity were: 20, 30, 40, 50 and 60° C. The complete experimental procedure contains a total time of roughly 200 minutes.

3.2.5 Fuel Moisture Content Calculation

The determination of moisture of fuel samples, or simply fuel moisture content (i.e. FMC), is achieved with the use of a heating oven. Before introducing the samples into the oven, these must be measured in a balance to obtain the weight of the samples containing moisture. Then, this oven is set up to a stable temperature of 60 °C, the samples are introduced in it, and during a period of 24 hours the samples are purged of almost all moisture, leaving a sample below 10% FMC. It is known that if the samples are for more than this amount of time the extra loss of moisture is negligible, ergo, not necessary to dry more than that. Finally, for obtaining this value, the dry samples must be placed in a balance to know the mass without moisture, to finally compute the difference to account for the moisture content. This is achieved by the direct calculation:

$$FMC = \frac{\text{mass wet sample} - \text{mass dry sample}}{\text{mass dry sample}} \times 100 \tag{3.8}$$

The drying procedure is simple and standardized, making it a routine step in sample preparation for this type of experiments. In synthesis:

1. Measure the weight of wet fuel samples.
2. Introduce wet samples inside the oven at 60 °C for 24 hours.
3. Retrieve the dry samples and measure their weight.
4. Determination of FMC calculation with Equation 3.8 for the fuel.

3.2.6 FTIR Optical Measurements

The relevant optical properties for transmittance and reflectance were measured using the FTIR equipment. For each measurement, a reference response was acquired without any sample in place (no sample in transmission and a cover of the same internal material for the case of reflectivity). Subsequently, the porous samples were introduced in the defined positions to determine the actual values of specular and diffuse transmittance and reflectance. This study focused fundamentally on the effect of sample thickness, considering three depths: 3, 5, and 10 mm. These optical properties were then compared across the three thicknesses.

For each thickness, three separate experiments were required to capture the complete spectrum under a given condition. Since three individual spectra needed to be measured per case, the process of combining them meaningfully was nontrivial due to the delicate nature of the equipment for small changes in the experiments. In cases of major discrepancies during post processing of the optical responses, repetitions were performed immediately to ensure consistency if necessary, since, if the responses were similar then no further repetitions are needed. Therefore, for a single thickness under one condition, a minimum of three measurements was required (i.e. for the three spectra discussed before: visible, NIR, and MIR).

The FTIR spectrometer was operated using the OPUS software, which handled data acquisition and basic processing right away. The transmission and reflection values were calculated relative to the reference data. The resolution and accuracy of the measurements depend on the number of scans performed by the detector in use. According to the equipment manual, 300 scans provide reasonable accuracy and reduced noise, however, 500 scans were chosen for this study to improve reliability and marginally less noise. While previous experiments at LEMTA used up to 5000 scans, such high number was deemed impractical for this international internship due to time constraints of two months and several other experiments at different places at LEMTA. With 500 scans, each measurement took approximately 7 minutes. Considering repetitions and all experimental conditions, a total of 27 to 81 measurements were planned, which can be roughly done in a week of work.

3.2.7 Thermal Inertia Determination

Following the theory behind the thermal inertia measurement, the temperature obtained at the center of the heating element, $T(t)$, should follow the same mathematical description provided by Equation 2.16. The inverse Laplace transform is solved by Matlab with the function "invlap", which is based on the De Hoog algorithm. Then, with the function "leasqr" from Matlab based on Levenberg-Marquart algorithm the specific parameters: E, mc_p/s, and R are minimized by the following sum (where N is the number of measurements):

$$s = \sum_{i=1}^{N} \left[T_{exp}(t_i) \; - \; T_{mod}(t_i) \right]^2 \tag{3.9}$$

Therefore, the analytical process is through an iterative estimation so it is necessary to set starting values for the parameters. These values are: $R = 10^{-4}\,\mathrm{m^2\,W^{-1}\,K^{-1}}$, $mc_p/s = 1{,}5 \cdot 10^6 \cdot e$, where e is the thickness of the heating element in meters, and $E = \rho_b/2$. Finally, after at least $400 - 500$ seconds, the semi-infinite media should be accurately obtained and, therefore, the thermal inertia measurement through the given Matlab code.

3.2.8 In-Depth Temperature Distribution Determination

For the study of incoming radiation toward the insulated box containing the porous samples, only pine needles were used. Two aspects of the radiative behavior were examined in these experiments. The first was to maintain non-flammable conditions in order to observe how transient and steady-state heat transfer developed under low heat flux. The second aimed to induce pyrolysis using a higher heat flux, allowing the analysis of radiative behavior in the presence of burning material up to a certain final stage with no unburnt material.

Therefore, positioning the radiometer at the center of the cone and at 2 cm from it, the two heat fluxes used were $4\,\mathrm{kW\,m^{-2}}$ and $40\,\mathrm{kW\,m^{-2}}$ for non-flammable and pyrolysis respectively. To achieve these values the temperature of the coil had to be risen up to $265°C$ for low heat flux and $719°C$ for high heat flux.

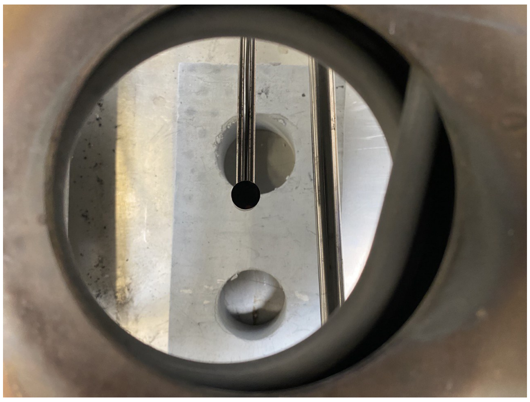

Figure 3.23: Radiometer positioning for cone calorimeter experiment.

For the calculation of the mass loss rate and the smoothing of the experimental data, numerical methods were applied using the central difference scheme for differentiation and the Savitzky–Golay filter for noise reduction and signal preservation (Staggs, 2005).

Finally, for the low heat flux condition, a total of three experiments with a duration of 180 minutes was established for each experiment, so that stationary phase could be ensured with certainty for such a low heat flux across all thermocouples. In contrast, for the fire experiment, solely one experiment could be carried out under the conditions of limited pine needles stock, so that pyrolysis could be reached and allow all material to be consumed. This stock of *Pinus Radiata* was limited due to the fact that these samples were brought from Chile to LEMTA, France.

Chapter 4

Experimental Results

A detailed analysis is presented for the experimental results obtained in this research, encompassing both fluid mechanics and heat transfer phenomena in the studied specimens of wood elements and pine needles comprising the porous fuel beds. Through both phenomena, diverse properties of the fuel beds and the specimens will reveal after full characterization how these fuels respond under the specific experimental conditions. Firstly, permeability values and other relevant characterizations of fluid transport studied in the vertical wind tunnel (i.e. the permeameter) for *Pinus radiata* pine needles and wood elements are discussed. Afterwards, focus turns to the study on heat transfer, where the section continues with radiative absorption and absorption coefficients for different porosities and packing, providing insight into how electromagnetic waves have attenuation in this porous media, conversely, how these waves interact with the participating media due to the aforementioned radiative transport theory.

Furthermore, a more profound emphasis is given to the analysis dedicated specifically to pine needles and their thermal response, including the study of direct and diffuse transmissivity and reflectivity, followed by the characterization of key physical properties such as thermal conductivity and specific heat capacity. Finally, to conclude the experimental results, the in-depth temperature distributions and one dimensional heat transfer analyses and results are revealed to provide a better understanding not only of radiation, but also of its interactions with conduction and calorimetry behavior.

4.1 Specimen Characterization

The study of *Pinus radiata* and wood elements for the experiments conducted in this investigation were done for determining the density and the morphological geometry. First of all, the density of both specimens was obtained for dry samples, therefore, the drying process to determine the FMC had to be carried out with the procedure mentioned in Section 3.2.1. Once this procedure was conducted, the density could be obtained. For the case of dry wood elements, these were already characterized in the previous research of (Pessoa, 2019), the reported density was found to be of $427\,\mathrm{kg\,m^{-3}}$. For the dry pine needles, 100 density measurements performed for a highly accurate density value on *Pinus radiata*, Table 4.1 shows a random sample of 10 values as reference.

Table 4.1: Density values for 10 experiments of dry *Pinus radiata*.

Mass Sample (g)	ρ_f **(kg m^{-3})**
0,0784	573,81
0,1319	484,95
0,1142	579,07
0,0991	587,01
0,0426	540,33
0,0944	503,59
0,1795	529,60
0,0780	569,83
0,0697	531,02
0,1602	507,10

The result for the average of all measurements gave a value for the density of dry pine needles of $\rho_f = 540\,\mathrm{kg\,m^{-3}}$. For the case of the SVR of wood elements, this calculation is geometrically simple, while considering a length for every wood element of 25 cm and for both thicknesses of 2 and 3 mm the calculation is the following:

$$\sigma = \frac{4 \cdot 0{,}002\,\mathrm{m} \cdot 0{,}25\,\mathrm{m} + 2 \cdot (0{,}002\,\mathrm{m})^2}{(0{,}002\,\mathrm{m})^2 \cdot 0{,}25\,\mathrm{m}} = 2008\,\mathrm{m^{-1}} \tag{4.1}$$

$$\sigma = \frac{4 \cdot 0{,}003\,\mathrm{m} \cdot 0{,}25\,\mathrm{m} + 2 \cdot (0{,}003\,\mathrm{m})^2}{(0{,}003\,\mathrm{m})^2 \cdot 0{,}25\,\mathrm{m}} = 1341{,}33\,\mathrm{m^{-1}} \tag{4.2}$$

For pine needles, the approach is the same as in (Vaz et al., 2004), the cross section area of a single needle is studied to approximate the SVR value. Consequently, through an imaging process carried out using a microscope with a mounted camera, then the software environment ImageJ for the case of live pine needle cross-section was determined in Figure 4.1a, which enabled the extraction of relevant geometric parameters through image based pattern recognition techniques. The procedure needed a known vertical distance of 1 mm, and with this the software could be used with this scale. The steps for this method consisted of using the tool called *Straight* to define the known distance. Then, the option *Analyze* to *Set Scale* in *Known distance*. Afterwards, this must be in the correct units with the option called *Unit of length* and finally pressing *Global*. With these configurations, options *Image*, *Type*, and *16-bit* accompanied by *Image*, *Adjust*, and *Threshold* to conclusively just use *Wand* to select the area of interest to obtain the geometrical values so that with *Analyze* and *Measure* the results are printed in next to the colored illustration. This image study was thanks to Mr. Jorge Valdivia, PhD candidate from WPI.

Conversely, for dead and dried pine needles, the approach is roughly similar, where a Stereo microscope from Fisher Scientific device with 40× magnification of images was utilized. Here, four different samples were used and five cross-sections were obtained, one example of these images is seen in Figure 4.1b. The device is equipped with an internal camera with its own software, the images were simply exported to be studied from their geometrical properties. For this study of how the cross-section geometry changed, a simple Python program using the pattern recognition called cv2 can give the desired measurements, this code is shown in Appendix A.

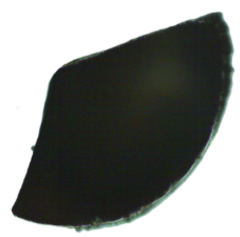

(a) Live pine needle cross-section perimeter and area.

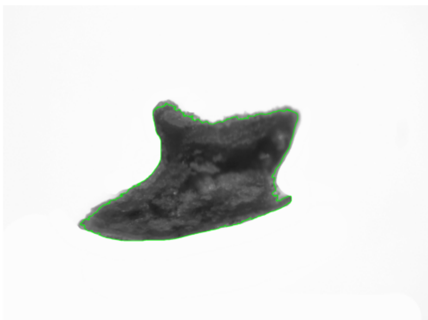

(b) Dead and dry pine needle cross-section perimeter and area.

Figure 4.1: Morphological differences for cross-section images of *Pinus radiata* between live and dead structure. (the other three pictures of dead specimens are in Appendix A)

The visual difference between both can be understood by how the two faces from below and the right of the cross-section of Figure 4.1a significantly shrinks when compared to dry and dead structure, leaving a notorious tapered section on top of the geometry as can be seen in Figure 4.1b, where the difference in cross-section follows the pattern of similar pine needles (Bouche et al., 2015). Based on the image analysis, in which only one representative image was used for live pine from the four images analyzed for dead pine, the geometrical quantities of perimeter and area of the cross-section were retrieved. Therefore, the calculation of SVR is now possible for live *Pinus radiata* and the specific values of perimeter and area in Figure 4.1a are 0,426 cm and 0,006 cm^2, respectively. With the previous information, the SVR for live pine needles is the following calculation and for dead pine needles these are in Table 4.2:

$$\sigma = \frac{0{,}00426\,\mathrm{m}}{6 \cdot 10^{-7}\,\mathrm{m}^2} = 7.100\,\mathrm{m}^{-1} \tag{4.3}$$

Table 4.2: SVR values for dry and dead *Pinus radiata* from image analysis with Python.

Sample	σ **(m^{-1})**
1	12.162
2	14.592
3	15.271
4	15.649

The average value for the SVR in this small group of samples in the previous table is 14.418 m^{-1}. As it can be seen, the difference between SVR for the condition of *Pinus radiata* is evident, where the value is more than double when the sample is dead and dried. Lastly, to account for the characteristic length, Equation 3.6 is used, where the perimeters and areas are of importance again. Considering that one specimen of *Pinus radiata* usually come in groups of 3 needles per fascicle, the physical characteristics are considered as such.

Table 4.3: Physical characteristics of the specimens.

Specimen	L_c **(m)**	ρ **($kg\,m^{-3}$)**	σ **(m^{-1})**
Live pine needle	0,00168	–	7.100
Dead pine needle	0,00084	540	14.418
Wood $2 \times 2\,mm^2$	0,002	427	2.008
Wood $3 \times 3\,mm^2$	0,003	427	1.341,33

4.2 Permeability

The permeability analysis conducted on the selected specimens of pine needles and wood elements carried out in the vertical wind tunnel successfully characterized the permeabilities and airflow for the given conditions and from known scientific literature results for the conditions encountered in wildland fire propagation. For the first set of experimental results for *Pinus radiata* the permeabilities and other parameters of relevance were obtained in these experiments. Pressure drops for the tests are mainly attributed to Darcy and Forchheimer regimes, which are differentiated from one another due to an approximated Reynolds number equivalent to unity, correlated by a dependency of characteristic lengths and the airflow conditions. This behaviors within the experimentally measured velocity range reveals the nature of how pine needles have the capacity of allowing fluids to pass through the porous matrix under very specific conditions. The permeability values obtained from the data are reported for each sample, allowing for a quantitative assessment of the porous medium capacity to transmit air under non-inertial and inertial conditions as described by the theory. Therefore, for dry pine needle fuel beds the characteristics of the geometries are known, from Table 4.3 the values of importance are of the characteristic length for an individual particle of 0,00168 m, a fuel density of 540 kg m^{-3}, and a SVR of 14.418 m^{-1}. As mentioned in the experimental work, the assessment of the permeability is for increasing masses for the fuel beds with high porosities due to the natural porosities that the specimen actually has (i.e. approximately 90%), hence, masses from $50 - 170$ g with intervals of 30 g were studied and characterized.

Figure 4.2: Example of fuel bed packing for pressure drop experiments to achieve permeability results.

Representation of the pressure gradients $-dp/dx$ with respect to Darcy velocity u_D for the different masses used are shown in the following figures, where the second degree slopes are adjusted for the points measured to retrieve permeabilities (K):

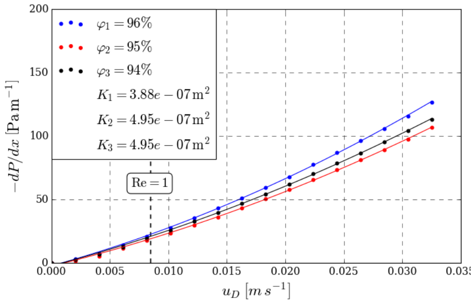

(a) 50g sample.

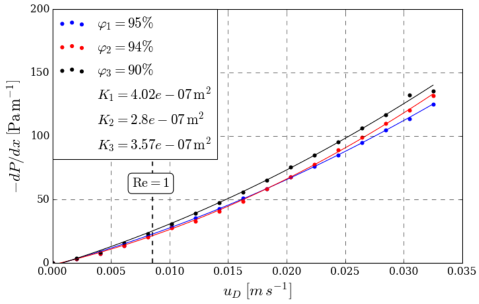

(b) 80g sample.

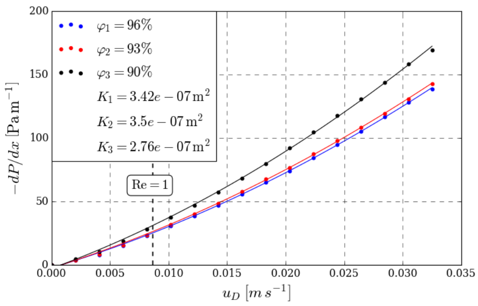

(c) 110g sample.

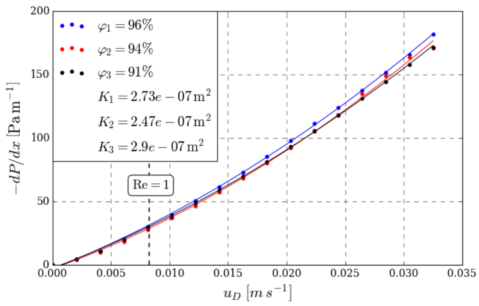

(d) 140g sample.

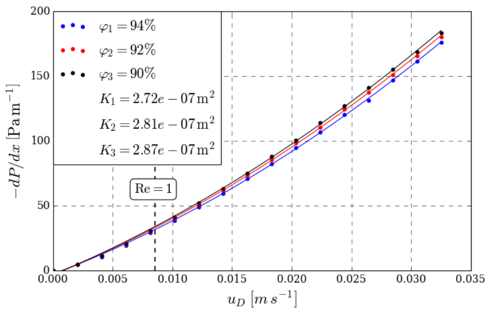

(e) 170g sample.

Figure 4.3: Pine needle fuel bed separated permeability results for all masses studied.

The transition from the Darcy to the Forchheimer flow regime can be clearly identified at the point where the Reynolds number reaches the mentioned value of one, which defines the approximated transition point for this porous medium. The polynomial fits are applied to the experimental data as in

Equation 3.2, to then extract the permeability coefficient as in Equation 3.3, meaning that these value depends highly on an accurate dynamic viscosity and of the adequate polynomial fit. These fits also captures the deviation from linearity, where the pressure gradient increases more sharply with velocity, indicating the onset of inertial effects as the velocity increases due to the airflow mass in the experimental apparatus. All experimental data for *Pinus radiata* pine needles are presented in the Table 4.4, where the measurements accompanying permeability from Section 3.2.2 are also present, such as temperature, porosity, FMC, dynamic viscosity, air density, and Darcy velocity.

Table 4.4: Permeameter Apparatus experimental results for dead and dried *Pinus radiata* pine needles.

Mass (g)	T (K)	φ (-)	M_f (-)	μ (Pa·s)	ρ (kg·m^{-3})	u_D (m·s^{-1})	K (m^2)
	290,02	96	3,0	$1{,}798 \cdot 10^{-5}$	1,259	0,00877	$3{,}88 \cdot 10^{-7}$
50	290,27	95	3,0	$1{,}799 \cdot 10^{-5}$	1,264	0,00871	$4{,}95 \cdot 10^{-7}$
	290,96	94	2,9	$1{,}803 \cdot 10^{-5}$	1,277	0,00850	$4{,}95 \cdot 10^{-7}$
	289,40	95	3,3	$1{,}795 \cdot 10^{-5}$	1,248	0,00889	$4{,}02 \cdot 10^{-7}$
80	290,97	94	3,3	$1{,}803 \cdot 10^{-5}$	1,277	0,00865	$2{,}80 \cdot 10^{-7}$
	290,73	90	3,3	$1{,}801 \cdot 10^{-5}$	1,272	0,00846	$3{,}57 \cdot 10^{-7}$
	288,75	96	2,9	$1{,}792 \cdot 10^{-5}$	1,236	0,00864	$3{,}42 \cdot 10^{-7}$
110	288,86	93	3,0	$1{,}792 \cdot 10^{-5}$	1,238	0,00819	$3{,}50 \cdot 10^{-7}$
	290,76	90	3,0	$1{,}802 \cdot 10^{-5}$	1,273	0,00879	$2{,}76 \cdot 10^{-7}$
	292,46	96	3,3	$1{,}810 \cdot 10^{-5}$	1,305	0,00845	$2{,}73 \cdot 10^{-7}$
140	290,22	94	3,2	$1{,}799 \cdot 10^{-5}$	1,263	0,00813	$2{,}47 \cdot 10^{-7}$
	288,58	91	3,1	$1{,}791 \cdot 10^{-5}$	1,233	0,00826	$2{,}90 \cdot 10^{-7}$
	289,39	94	2,8	$1{,}795 \cdot 10^{-5}$	1,248	0,00826	$2{,}72 \cdot 10^{-7}$
170	291,23	92	2,8	$1{,}804 \cdot 10^{-5}$	1,282	0,00848	$2{,}81 \cdot 10^{-7}$
	294,09	90	2,8	$1{,}818 \cdot 10^{-5}$	1,336	0,00850	$2{,}87 \cdot 10^{-7}$

As shown in Table 4.4, for high porosities in the vicinity of the natural porosity of these kind of fuel beds and at ambient temperatures roughly similar, permeability values for pine needles are in the range of 10^{-7} m^2, which is in accordance to already known values for the same species as reported by (Fehrmann et al., 2017). One important consideration when carrying out these experiments is when the values of u_D are small (e.g., between 0,001 and 0,03 m s^{-1}), and the quadratic term is much smaller than the linear one, the corresponding coefficients can differ by several orders of magnitude affecting the real value for permeability when using Equation 3.3. This leads to numerical instability in the least-squares fitting method implemented in `np.polyfit`, which is used in Python when analyzing these data. When `np.polyfit(`x_{vel}`, y, 2)` is used, the algorithm internally builds a Vandermonde matrix. If the abscissa values (in this case, the velocities) are small, then the squared terms x^2 become of order 10^{-4}, creating a strong imbalance between the magnitudes of the matrix columns. As a result, the polynomial fitting becomes ill-conditioned: the computed coefficients may be extremely large or small. To mitigate this issue, a simple scaling can be applied so that all inputs fall within the range $[0, 1]$. In this scaled form, higher powers such as x^2, x^3, etc., remain of comparable magnitude, which stabilizes the numerical conditioning of the problem. Consequently, `np.polyfit` yields more realistic coefficients that are not dominated by numerical errors.

Consequently, the plausible results in the mentioned order of 10^{-7}, where also a literary review article on permeability (Mueller et al., 2021) explained that the magnitudes of permeabilities for *Pinus rigida* are between $10^{-5} - 10^{-7}$ m^2 when compared to those by (Fehrmann et al., 2017). Other studies showed that for *Pinus laricio* the permeability also revolved in the order of 10^{-7} again (Santoni et al., 2014), where slight differences in the results can be attributed and traced to experimental design differences, such as the blower for the air, how airflow mass is determined, and so on. A comparative analysis can be made from all experiments performed, where the gradients shift upwards as mass is incremented:

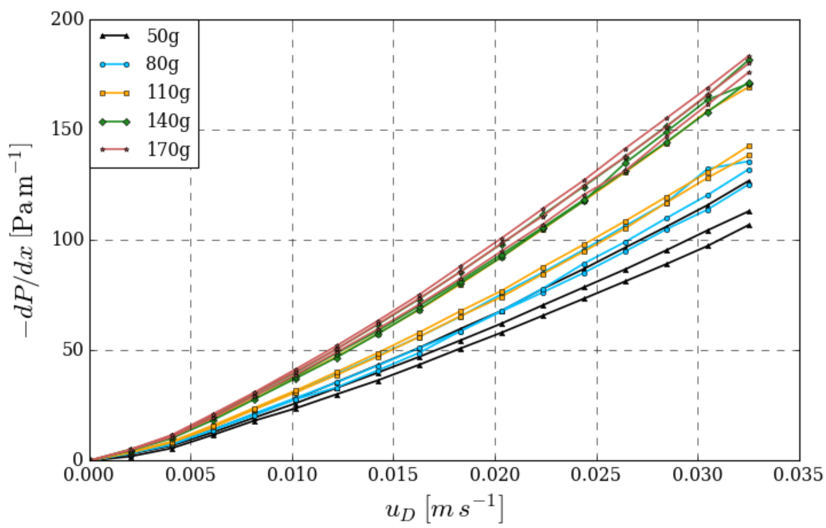

Figure 4.4: Example of fuel bed packing for pressure drop experiments to achieve permeability results in pine needles.

Following the results of pine needles, attention is now turned to wood elements, which represent a structurally denser and less porous vegetative material, these elements were selected due to their similar characteristics of being thin and elongated. This shift aims to explore how permeability behavior differs when the fibrous structure is more compact and anisotropic, as typically found in wildland floors. The comparison between these two types of samples is that it provides valuable insight into the role of material structure on airflow in porous media. For wood elements of square cross-section of $3 \times 3\,\text{mm}^2$ with characteristic length of 0,003 m is shown in the following plots:

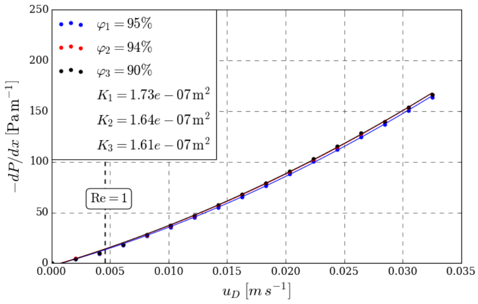

(a) 50g sample.

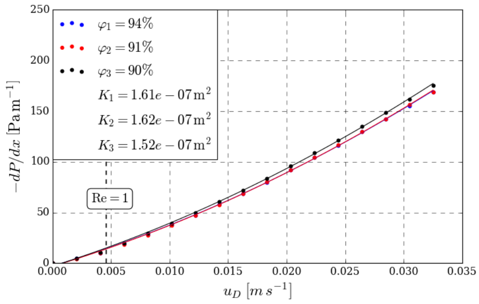

(b) 80g sample.

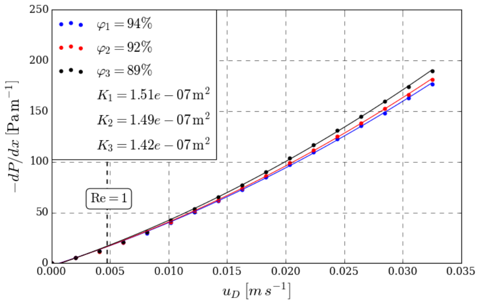

(c) 110g sample.

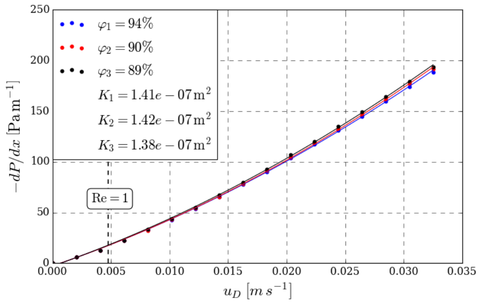

(d) 140g sample.

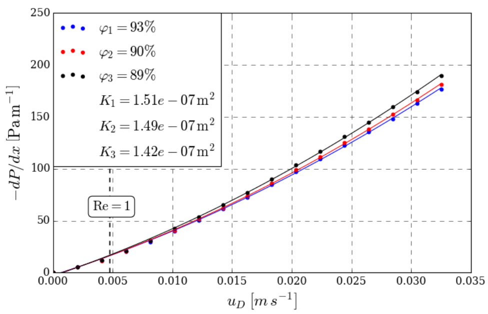

(e) 170g sample.

Figure 4.5: Wood elements with cross-section $3 \times 3\,\text{mm}^2$ fuel bed separated permeability results for all masses studied.

The permeability response for the $3 \times 3\,\mathrm{mm}^2$ wood elements shows a clear dependence of the pressure gradient on the Darcy velocity, as presented in Figure . The polynomial fits applied to the experimental measurements capture both the linear Darcy regime and the curvature associated with inertial effects, but the principal difference is that the magnitude of the y-axis is that now is far greater. Then, transition from Darcy to Forchheimer behavior occurs at much lower velocities compared to pine needles, reflecting the denser and more rigid structure of the wood elements with greater impact of area with airflow. This earlier onset of inertial effects suggests that the more compact arrangement and the bigger the specimens then the available pores within the fuel bed plays a dominant role in restricting airflow. The overview of these results are in the following table:

Table 4.5: Permeameter experimental results for $3 \times 3\,\mathrm{mm}^2$ cross-section wood elements.

Mass (g)	T (K)	φ (-)	M_f (-)	μ (Pa·s)	ρ (kg·m^{-3})	u_D (m·s^{-1})	K (m^2)
	292,61	95	4,1	$1{,}810 \cdot 10^{-5}$	1,308	0,00461	$1{,}73 \cdot 10^{-7}$
50	290,37	94	4,0	$1{,}800 \cdot 10^{-5}$	1,266	0,00474	$1{,}64 \cdot 10^{-7}$
	293,38	90	4,0	$1{,}814 \cdot 10^{-5}$	1,323	0,00457	$1{,}61 \cdot 10^{-7}$
	293,20	94	2,9	$1{,}813 \cdot 10^{-5}$	1,319	0,00458	$1{,}61 \cdot 10^{-7}$
80	293,51	91	2,8	$1{,}815 \cdot 10^{-5}$	1,325	0,00460	$1{,}62 \cdot 10^{-7}$
	291,21	90	2,8	$1{,}804 \cdot 10^{-5}$	1,281	0,00469	$1{,}52 \cdot 10^{-7}$
	289,79	94	2,8	$1{,}797 \cdot 10^{-5}$	1,255	0,00477	$1{,}51 \cdot 10^{-7}$
110	291,28	92	2,8	$1{,}804 \cdot 10^{-5}$	1,283	0,00469	$1{,}49 \cdot 10^{-7}$
	291,53	89	2,8	$1{,}805 \cdot 10^{-5}$	1,287	0,00467	$1{,}42 \cdot 10^{-7}$
	290,32	94	2,9	$1{,}799 \cdot 10^{-5}$	1,265	0,00474	$1{,}45 \cdot 10^{-7}$
140	291,75	90	2,9	$1{,}806 \cdot 10^{-5}$	1,292	0,00466	$1{,}42 \cdot 10^{-7}$
	293,60	89	2,9	$1{,}815 \cdot 10^{-5}$	1,327	0,00456	$1{,}38 \cdot 10^{-7}$
	290,33	93	2,8	$1{,}799 \cdot 10^{-5}$	1,265	0,00474	$1{,}51 \cdot 10^{-7}$
170	292,12	90	2,8	$1{,}808 \cdot 10^{-5}$	1,298	0,00464	$1{,}49 \cdot 10^{-7}$
	294,84	89	2,8	$1{,}821 \cdot 10^{-5}$	1,351	0,00449	$1{,}42 \cdot 10^{-7}$

Table 4.5 reveals permeability values in the same order as before, of $10^{-7}\,\mathrm{m}^2$, this implies that the permeabilities for artificial objects with a higher surface and more uniform structure, but at same masses and porosities maintain this trend. Nevertheless, the first difference that can be spotted is regarding a more closed variability of permeabilities, since for pine needles the minimum and maximum values for permeability were $2{,}47 - 4{,}95 \cdot 10^{-7}\,\mathrm{m}^2$, whereas for these wood elements the average value revolved around $1{,}52 \cdot 10^{-7}\,\mathrm{m}^2$,

with a range of $1{,}42 - 1{,}73 \cdot 10^{-7}\,\mathrm{m}^2$, therefore, not the same variability. Subsequently, the transition regime is far behind for wood elements due to the greater characteristic length, signifying a transition point towards Forchheimer regime right after the second pressure drop, also due to the bigger surface which provides more resistance and inertial effects for this phenomenon. With respect to known measured values, the previous study done at UAI revealed permeability values in the order of $10^{-7} - 10^{-9}\,\mathrm{m}^2$, where these results revealed how porosity affects the permeability for these kind of fuel beds:

Table 4.6: Previous permeability results for wood elements (Pessoa, 2019).

φ **(-)**	K **(m^2)**
24	10^{-9}
35	10^{-9}
48	10^{-8}
53	10^{-8}
61	10^{-8}
74	10^{-7}
87	10^{-7}

As a complement to the information of Table 4.6, when porosity is low (i.e. densely packed) it tends to behave more as a solid with a permeability of $10^{-9}\,\mathrm{m}^2$, but as porosity increases it reaches the order of $10^{-7}\,\mathrm{m}^2$, therefore, from porosities beyond this value up to 90% it is the same order, but closer to $10^{-6}\,\mathrm{m}^2$. The trend is arguably explained by the less amount of resistance that the porous medium offers, through this logic, the different permeability values are more predictable since the fuel bed can be arranged with an artificial specimen such as this one. As a matter of fact, the same author indicates that values beyond the limits that were tested can be extrapolated with a trend of error of $R^2 = 0{,}9908$, then again, for these artificial fuel bed arrangements. The question could be posed for a randomly arranged fuel bed with these wood elements that may vary the tortuosity, which is a far more difficult parameter to characterize.

The same comparative analysis as the one presented in Figure 4.4, aims to show how all pressure drops differ for all experiments. In this sense, in Figure 4.6 it can be seen how the difference, as the results of Table 4.5 hint, are much closer to one another, nevertheless, the difference for the mass increment is noticeable. The gradients shift upwards again, and pressure gradient reach a maximum of roughly $200\ -dp/dx$ as in comparison to the limit of roughly $175\ -dp/dx$ from pine needles, due to greater inertia offered from larger particles.

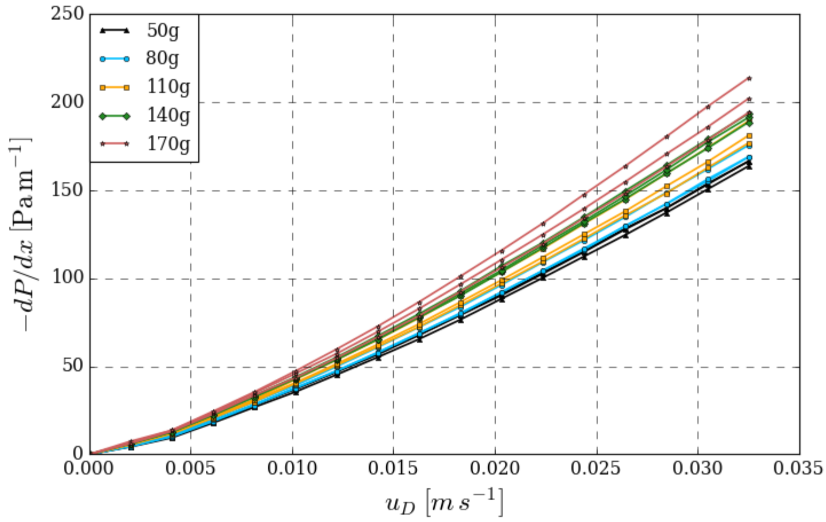

Figure 4.6: Example of fuel bed packing for pressure drop experiments to achieve permeability results in wood elements with a cross-section $3 \times 3\,\mathrm{mm}^2$.

Similarly, for wood elements of cross-section $2 \times 2\,\mathrm{mm}^2$, what should be expected based on the previous results with $3 \times 3\,\mathrm{mm}^2$ cross-section wood elements is that changes should not be that significant due to a small difference for the cross section. Therefore, the same masses should be quantified with more wood elements due to them being smaller, ergo, requiring more specimens to accommodate the same conditions of porosity and mass. Hence, these values are shown in the following plots of Figure 4.7, where again the similarities of pressure drops for each mass is roughly the same (with the exception of the 140g sample with a distinct separation for the pressure drops) meaning that permeability values are very close together for each mass. Another aspect is that transition of regime changed again, due to the evident change of characteristic length 1 mm smaller than with respect to the previous wood element, with 0,002 m, which is represented as a higher transition, after the third pressure drop measured. The permeabilities for this case are again in the order of $10^{-7}\,\mathrm{m}^2$, and when compared to pine needles, the wood samples exhibit higher permeability values and earlier transition to inertial flow, characteristics that are consistent with their denser, less deformable structure. This comparison highlights the necessity of accounting for material anisotropy and packing ratio configuration in the modeling of airflow through natural porous media relevant to wildland fire propagation and other environmental transport phenomena. All plots are in the following figures:

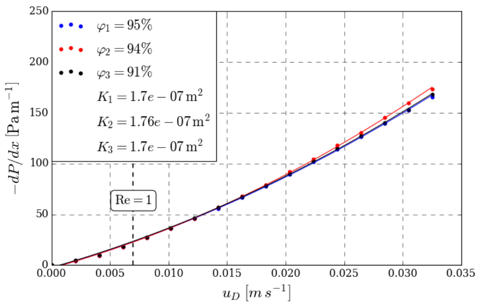

(a) 50g sample.

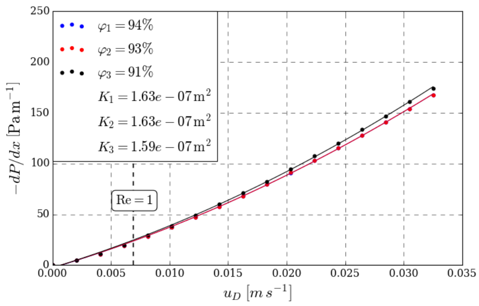

(b) 80g sample.

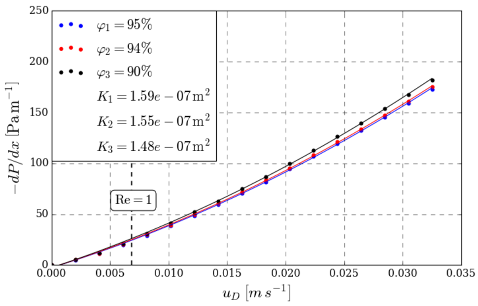

(c) 110g sample.

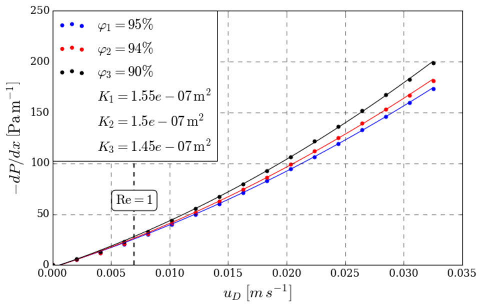

(d) 140g sample.

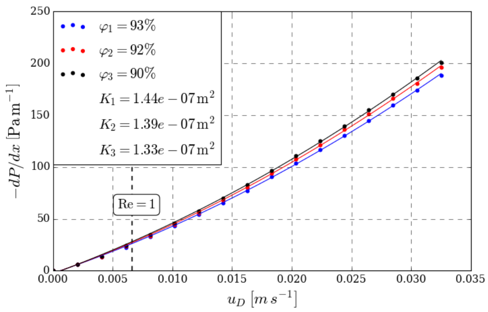

(e) 170g sample.

Figure 4.7: Wood elements with cross-section $2 \times 2\,\mathrm{mm}^2$ fuel bed separated permeability results for all masses studied.

Here the different configuration with respect to the other specimens analyzed before exhibits similar trends as before. This implies that a smaller cross sectional surface allows a nearly negligible difference in interconnection of pores to follow uniform air flow, even when the number of elements per unit volume is higher.

A comparison between the two types of wood elements, while considering all results in Table 4.7, reveals that for $2 \times 2\,\mathrm{mm}^2$ configuration this has some higher permeabilities and other lower, showing how small the differences are, at a small scale, where the maximum value was $1{,}76 \cdot 10^{-7}\,\mathrm{m}^2$. This could be directly attributed to the reduction of characteristic length which directly influences the regimes of flow and permeability determination. All the parameters from these results are in the following table:

Table 4.7: Permeameter experimental results for $2 \times 2\,\mathrm{mm}^2$ cross-section wood elements.

Mass (g)	T (K)	φ (-)	M_f (-)	μ (Pa·s)	ρ (kg·m^{-3})	u_D (m·s^{-1})	K (m^2)
	291,89	95	3,3	$1{,}807 \cdot 10^{-5}$	1,294	0,00698	$1{,}70 \cdot 10^{-7}$
50	295,56	94	3,3	$1{,}825 \cdot 10^{-5}$	1,365	0,00668	$1{,}76 \cdot 10^{-7}$
	291,65	91	3,2	$1{,}806 \cdot 10^{-5}$	1,290	0,00700	$1{,}70 \cdot 10^{-7}$
	292,84	94	3,1	$1{,}812 \cdot 10^{-5}$	1,312	0,00690	$1{,}63 \cdot 10^{-7}$
80	291,70	93	3,0	$1{,}806 \cdot 10^{-5}$	1,291	0,00700	$1{,}63 \cdot 10^{-7}$
	294,50	91	3,0	$1{,}819 \cdot 10^{-5}$	1,344	0,00677	$1{,}59 \cdot 10^{-7}$
	293,25	95	2,9	$1{,}813 \cdot 10^{-5}$	1,320	0,00687	$1{,}59 \cdot 10^{-7}$
110	294,38	94	2,9	$1{,}819 \cdot 10^{-5}$	1,342	0,00678	$1{,}55 \cdot 10^{-7}$
	293,61	90	2,9	$1{,}815 \cdot 10^{-5}$	1,327	0,00684	$1{,}48 \cdot 10^{-7}$
	292,44	94	2,9	$1{,}810 \cdot 10^{-5}$	1,304	0,00694	$1{,}55 \cdot 10^{-7}$
140	294,22	91	2,9	$1{,}818 \cdot 10^{-5}$	1,339	0,00679	$1{,}50 \cdot 10^{-7}$
	295,45	89	2,9	$1{,}824 \cdot 10^{-5}$	1,363	0,00669	$1{,}45 \cdot 10^{-7}$
	296,13	93	2,8	$1{,}827 \cdot 10^{-5}$	1,376	0,00664	$1{,}44 \cdot 10^{-7}$
170	296,75	92	2,7	$1{,}830 \cdot 10^{-5}$	1,388	0,00659	$1{,}39 \cdot 10^{-7}$
	295,32	90	2,7	$1{,}823 \cdot 10^{-5}$	1,360	0,00670	$1{,}33 \cdot 10^{-7}$

As shown in Table 4.7, permeability values for these samples range between $1{,}33 \cdot 10^{-7}\,\mathrm{m}^2$ and $1{,}76 \cdot 10^{-7}\,\mathrm{m}^2$, therefore, these values also reveal small variability between one another, this also occurred with the other specimens of wood. A clear distinction to how much the permeability changed with slightly smaller wood elements is not for a substantial amount, this implies that this change did not produce great change in the permeability. The difference between all slopes for these fuel beds with their measured values of pressure drops is shown in Figure 4.8, where when compared to both Figures 4.4 and 4.6, this plot reveals the most compactness for all pressure drops across all masses.

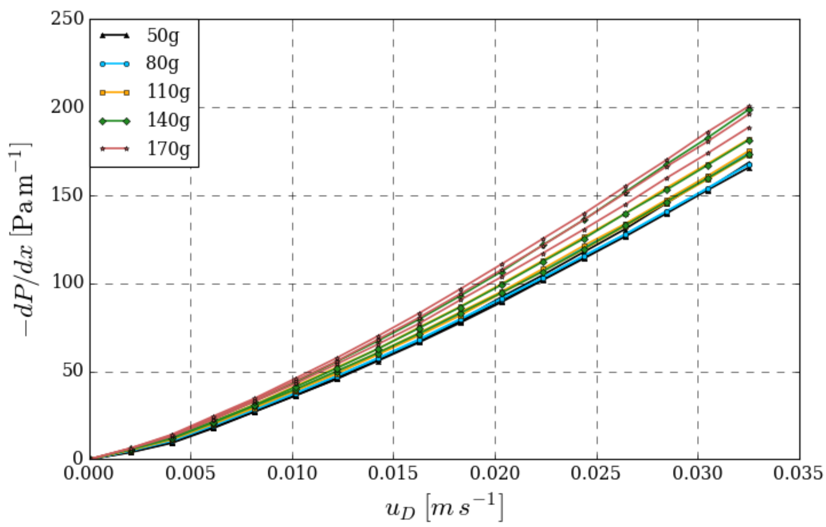

Figure 4.8: Example of fuel bed packing for pressure drop experiments to achieve permeability results in wood elements with a cross-section $2 \times 2\,\text{mm}^2$.

As a final takeaway from the study regarding permeability, it resulted in all values in the same order of $10^{-7}\,\text{m}^2$, which has a correct physical meaning when compared to the same pine needles studied by (Fehrmann et al., 2017) and also for wood elements studied by (Pessoa, 2019). The principal differences can be attributed to the fuels being at a very dry state with respect to the FMC, implying a different SVR, higher porosities, and a highly accurate measurement of dynamic viscosity and air density with the fluid mechanics formulae used in this study, which consider ISA reference values and better mathematical descriptions, since permeability is calculated with the polynomial fit with respect to dynamic viscosity. These findings underline the necessity of considering material anisotropy, particle size, and packing configuration when modeling airflow in fuel beds, as they directly affect the mechanisms of fluid transport in natural and artificial porous media relevant to wildland fire spread. The validation of permeability from previous studies is validated.

4.3 Optical Responses

Transmissivity results and absorption coefficients were obtained for pine needles, while reflectivity was analyzed only for these samples. All measurements for pine needles covered the spectral range from the visible to the far infrared. In addition, absorption coefficients were determined for pine needles and wood elements at several packing ratios. The analysis was performed using geometric optics and the Bouguer–Beer–Lambert Law, allowing for a comparative evaluation of the results for visible and near infrared spectrum only.

4.3.1 Reflectance and Transmittance

Regarding transmission and reflection of pine needles, the focus in understanding how these two physical properties across a broad infrared range is key to fully describing the phenomena associated with the RTE problem for this biomass. Data for reflectivity can be seen in Figure 4.9 for the three thicknesses used: 3, 5, and 10 mm. The results reveal that reflection highly depends on wavelength, reaching the maximum values of 35 % between the 5000 $-$ 8000 cm^{-1} range, meanwhile, the response towards the visible spectrum decreases below 20 % in the range of 15 $-$ 10 % until 18000 cm^{-1}, whereas for the far infrared the reflectance is at the lowest with values values below 10 % in the range of 9 $-$ 2 % under 2000 cm^{-1} reaching 450 cm^{-1}.

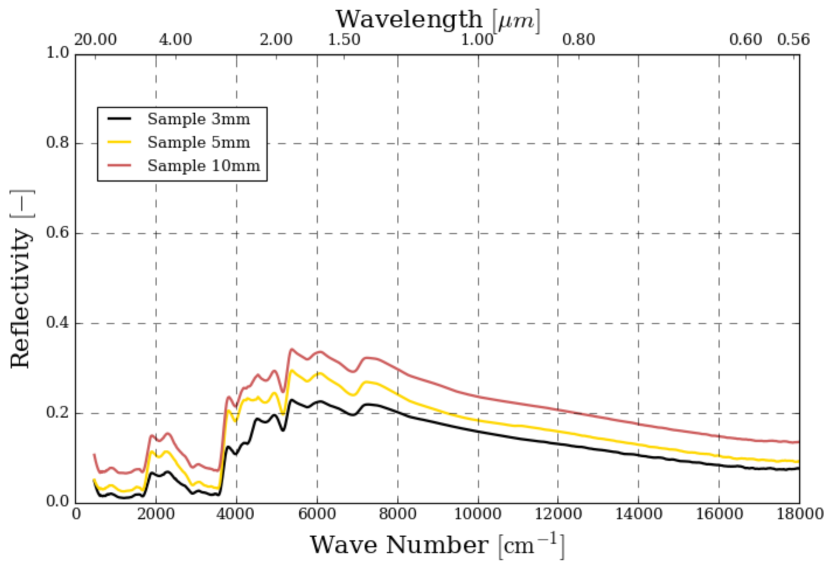

Figure 4.9: Reflectivity of pine needles with different thicknesses.

As expected, thicker pine needle samples tend to reflect more light, however, the relatively small differences in reflectivity among the three cases suggests the existence of a saturation threshold, beyond which increasing thickness no longer leads to more reflection, as it should be. This is consistent with the physical meaning of the reflectivity increase in the plot, where electromagnetic waves and porous material interaction only have a portion of this radiation reflected regardless of thickness. Although the overall trend is particularly similar for all three thicknesses, their absolute reflectivity levels differ.

Subsequently, to analyze the transmissivity of pine needles, it is important to distinguish between two types of measurements: direct and diffuse transmissivity. In the case of diffuse transmission, scattering phenomena are taken into account. As a result, this type of optical response is expected to yield higher transmissivity values compared to direct transmission. Therefore, this transmissivity response is shown in Figure 4.10, the most evident attribute of this behaviour is that for all samples these values are very flat, where small fluctuations can be seen in the far infrared range. The data clearly demonstrates that thickness plays a major role in the amount of light transmitted through the porous material. Thinner samples exhibit significantly higher diffuse transmissivity, where the 3 mm sample reaches values up to 50 % and above 40 % across all the spectrum, then again maintaining a relatively flat behavior in the visible. In contrast, the other two thicker samples of 5 mm and 10 mm reduces significantly their transmissivity, with values that remain below 21 % and 10 %, respectively. Another interesting trend is that with thickness increase the optical response becomes even more flat for all the spectrum.

The general trend for these diffuse transmissions suggests that there is a consistency for a flat response for all three thicknesses, moreover scattering and absorption phenomena limit drastically the amount of light that can pass through the medium once their thickness is slightly increased a few millimeters.

In addition to the information of diffuse behaviour, the direct or specular radiation for the pine needles is examined following the same logic as before. As it was mentioned, this radiative transmission should be smaller than diffuse transmission, this is evidenced in Figure 4.11. The plot again indicates another flat behaviour for the visible and near infrared spectrum. However, the most significant difference compared with Figure 4.10 is that far infrared region exhibits slightly higher transmissivity values in the spectrum. In this perspective, the 3 mm sample is slightly above 30 % for all wavelengths reaching maximums near the 40 % threshold in far infrared, whereas both 5 mm and 10 mm samples drop below 20 %. For 5 mm sample it is roughly 20 % in far infrared, then it remains constant at 12 % until 18000 cm^{-1}, lastly for 10 mm it drops from 9 % to $5 - 1$ % for near infrared and visible. Notably,

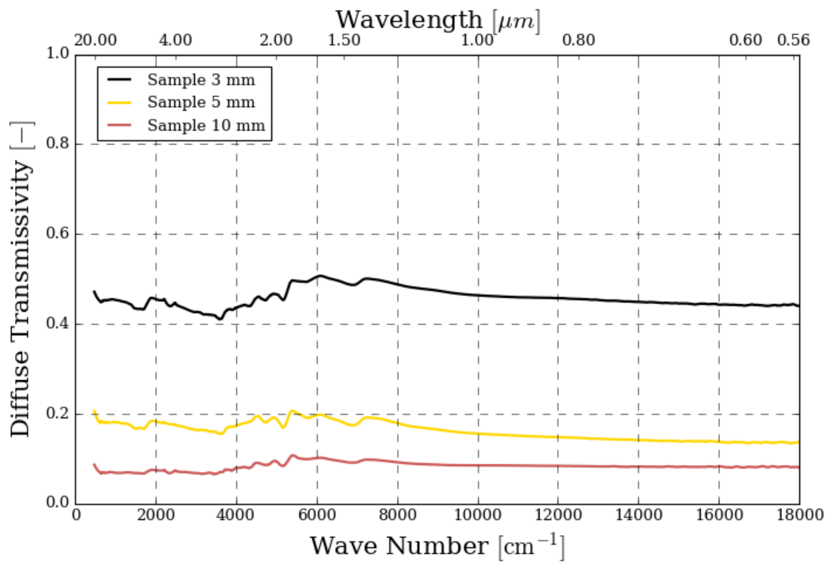

Figure 4.10: Diffuse transmissivity of pine needles with different thicknesses.

the peaks of transmissivity for all samples occurs in the far infrared. It is normal that this responses are much smaller and stable since only undisturbed electromagnetic waves are being detected, neglecting the ones that diffuse transmission detected.

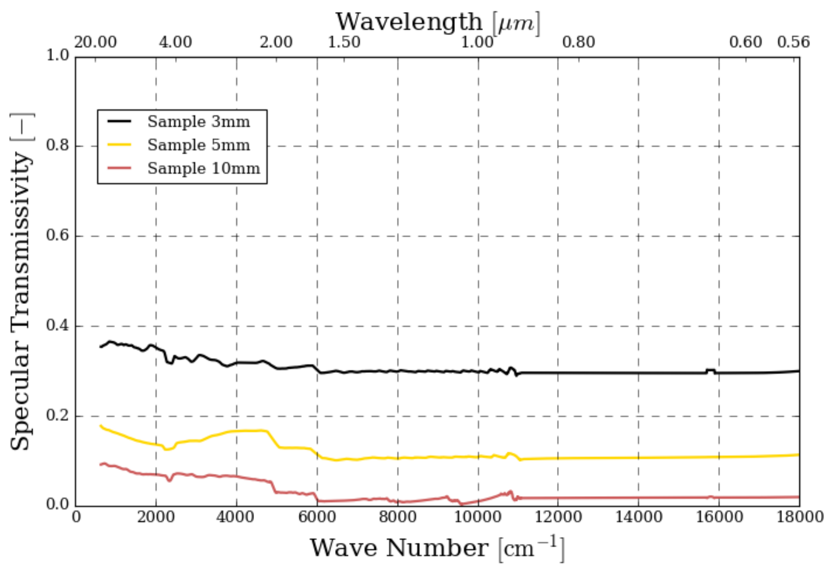

Figure 4.11: Specular transmissivity of pine needles with different thicknesses.

Finally, when comparing both diffuse and direct transmissivity, it becomes evident that the optical response of pine needles is strongly governed by thickness, but also by the intrinsic nature of the transmission process itself through this porous medium of *Pinus radiata*. Diffuse transmissivity dominates across the spectrum due to scattering within the porous samples, whereas direct transmissivity remains consistently lower as it only accounts for undisturbed radiation. Despite these differences, both behaviors show a characteristic flattening trend as thickness increases, highlighting the combined influence of absorption and scattering mechanisms in limiting radiation transfer through the medium. To emphasize this last remark, a contrast between both direct and diffuse transmissivity is seen in Figure 4.12, which illustrates the two types of transmissivity on a common basis, enabling a direct comparison of their magnitude and spectral features.

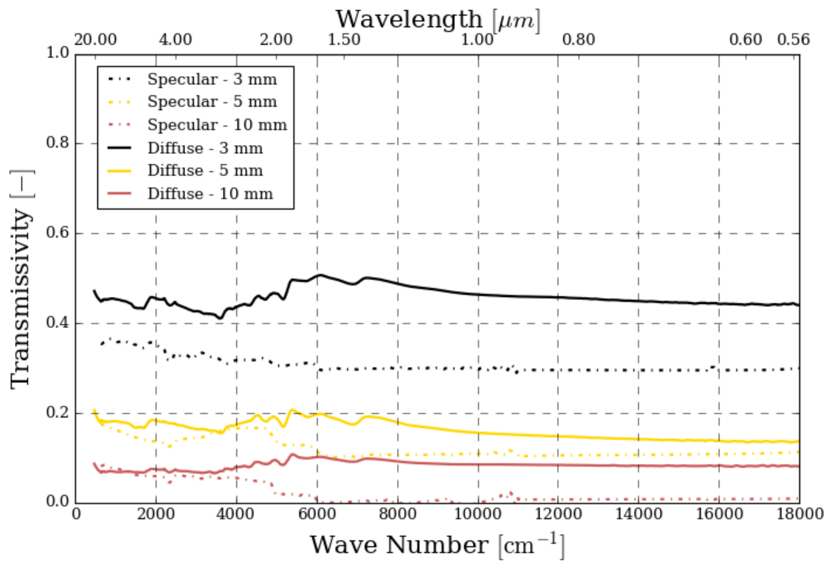

Figure 4.12: Specular and diffuse transmissivity of pine needles with different thicknesses.

Based on the previous information, absorption coefficients can be determined from the BBL Law and are only applicable for specular transmissivity, since diffuse transmissivity contemplates scattering. With this, the average value of transmission for the three thicknesses along with the absorption coefficient and the mean free path of radiation in these specific configurations is found in Table 4.8. As it can be appreciated, the lower transmission with the slight increase of thickness influences a decrease of absorption and an increase in the mean free path.

Table 4.8: Average transmissivities, absorption and mean free path of specular experiments with thickness variation.

Thickness	τ **(-)**	κ_λ **(m^{-1})**	δ **(m)**
3 mm	0,3119	388,35	0,0026
5 mm	0,1938	328,19	0,0031
10 mm	0,0498	299,97	0,0033

4.3.2 Absorption Coefficient: BBL Law and Geometric Optics

Intuitively, it could be argued that there is a clear difference between the BBL Law and the geometrical optics approach, since both intend to describe the same phenomena from two seemingly different properties. Regarding the optical properties, transmission of the fuel bed follows the exponential behavior from Equation 2.24, whereas for geometric optics it assumes the completely different behavior of a linear function from Equation 2.29. Thereafter, starting from this assumption of a clear dichotomy from the mathematical standpoint, it is put up to question how different both results describing this response are. For the case of wood elements, the analysis comes with ease since the structure of the fuel bed can be organized manually without much complication due to the geometry of the specimens. Therefore, a wide range of packing ratios could be analyzed, and the wide coverage of this response must clearly reveal the true behavior of the attenuation. Hence, for fuel beds with wood elements with a cross-sectional area of $2 \times 2\,\text{mm}^2$ can be seen in the following figure:

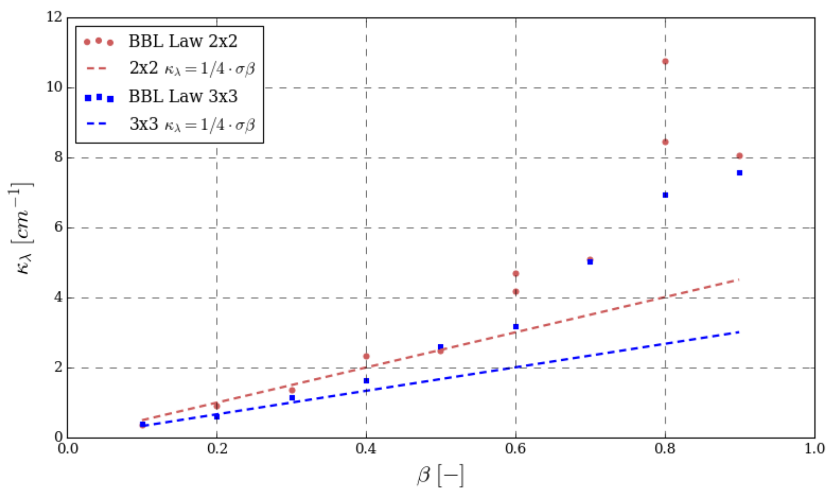

Figure 4.13: Optical response for 2×2 and $3 \times 3\,\text{mm}^2$ for BBL Law and Hottel Equation with respect to packing ratio.

For this case, the aforementioned differences between both responses is evident, meaning that for some packing ratio values the responses are extremely similar and for other values it is not. As packing increases, results from $\beta = 0{,}1 - 0{,}5$ are practically the same, this hints to an agreement between geometrical and radiative properties of the fuel bed. For the rest of the packing ratios, results become clearly different and the divergence becomes increasingly separated as β changes from 0,6 up to the limit value of study of 0,9. This result is interesting due to the two regions that appear in this tendency, where for low packing ratios, it is of no importance to choose between BBL Law or the geometric optics equation (i.e. $0 - 0{,}5$), but the other region for a high compactness of the fuel bed geometric optics fails completely. On the other case, for wood elements with a cross-sectional area of $3 \times 3\,\mathrm{mm}^2$, the responses must behave in a similar same manner, since the geometry is basically the same with the unique difference of the size of this cross-section. Consequently, with this change and, as a direct consequence, the smaller SVR from $2008\,\mathrm{m}^{-1}$ to $1341{,}33\,\mathrm{m}^{-1}$, the response for this fuel bed is different. The values of absorption coefficient are decreased in magnitude in comparison to the other response in the complete range of values. Then, the previous divergence seen in Figure 4.13 is then again present, but interestingly this shifted towards two new regions, where agreement between both is practically the same for $0{,}1 - 0{,}3$ packing ratios and arguably also for 0,4, where it becomes widely different starting from 0,5.

For both previous experimental results, these fuel beds were considered isotropic due to the configurations of with the wood elements, but with pine needles anisotropy in the assembly of the fuel beds is now considerable, because of the random positioning of the fuel. With this taken into consideration, the results show for pine needles the packing ratios are smaller, since the natural porosity of fuel beds composed of this type of pine is usually very high, around 90%. Therefore, increasing the packing ratio is physically meaningful only up to values of about 0,5. Beyond this point, further compaction would imply structural destruction of the needles themselves, and hence such values are not physically attainable in this context. Results for this specimens are shown in Figure 4.14, as it can be seen, for this case, the Hottel Equation greatly overestimates the measured values for this behavior due to its anisotropy and randomness. These effects of the fuel bed and of the much higher SVR value yield a result with no physical meaning for the geometrical approach. Therefore, in this case there is basically no similarity and the only point close to the other is just at $\beta = 0{,}1$, which represents the natural porosity of pine needle fuel beds.

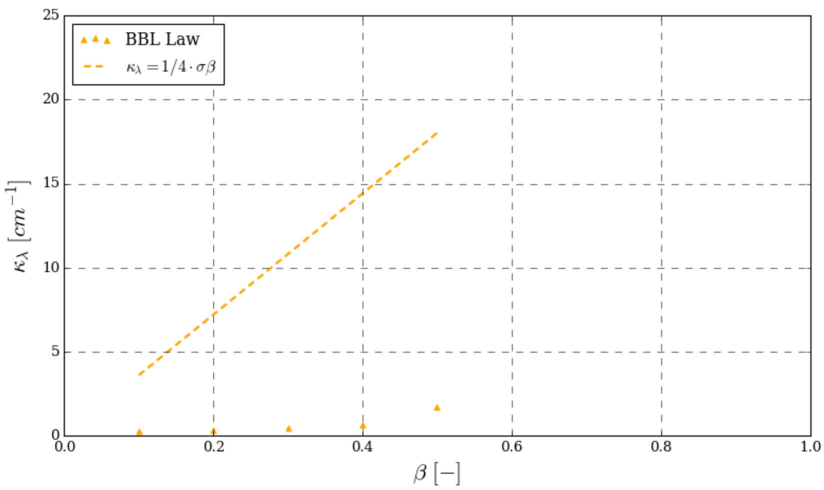

Figure 4.14: Optical response for *Pinus radiata* for BBL Law and Hottel Equation with respect to packing ratio.

Finally, a representation for all three behaviors is found by rearranging in the abscissa the product of SVR and packing ratio, revealing common trends for how the divergence of measured values with respect to $1/4 \cdot \sigma\beta$.

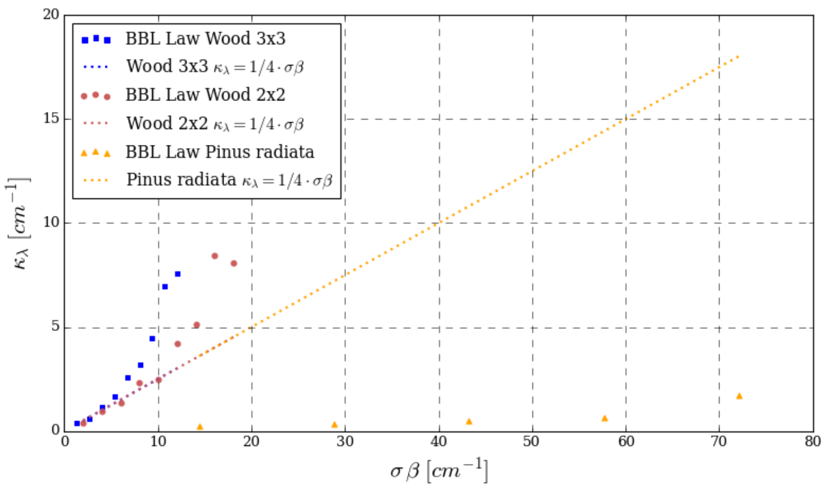

Figure 4.15: Optical response for *Pinus radiata* and both wood elements for BBL Law and Hottel Equation with respect to SVR and packing ratio.

4.4 Thermal Analysis

In order to determine the thermal conductivity of the pine needle sample, the thermal inertia model was employed. As a first result of this process for determining the conductivity, the specific heat capacity of *Pinus radiata* had to be estimated to complete one part of the thermal inertia from Equation 2.15 and quantify this key property. From the simple experimentation done with the microcalorimeter, Table 4.9 shows the specific heat capacity of dry pine needles of *Pinus radiata* (with $0-3\%$ moisture due to the vacuum drying process it went through), where, as a function of temperatures it shows how it fluctuates as the temperature rises gradually from 20 °C up to the threshold of 60 °C.

Table 4.9: Specific heat capacity of *Pinus radiata*.

Temperature (°C)	c_p **(kJ kg^{-1} K^{-1})**
20	1,550
30	1,654
40	1,737
50	1,851
60	2,014

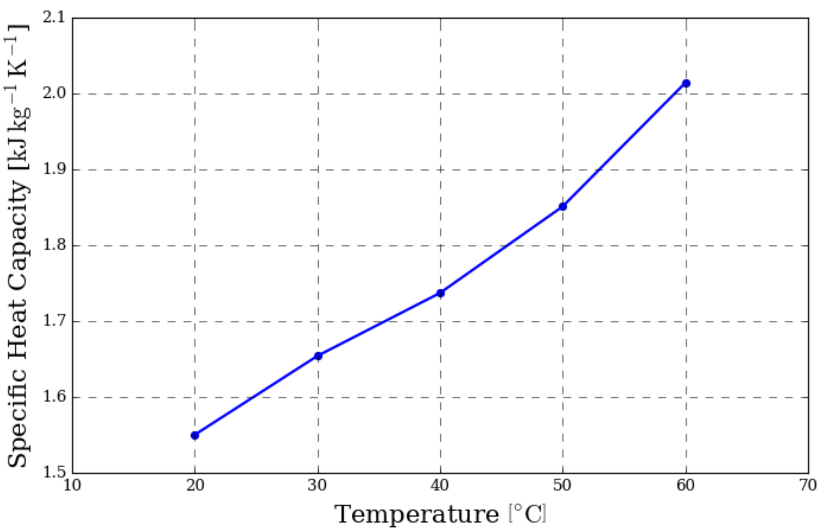

Figure 4.16: Evolution of c_p of dry pine needles with respect to temperature.

From the previous figure, in cases where a fuel does not reach pyrolysis, it can be correctly assumed that the specific heat fluctuates roughly uniformly

(Finney et al., 2021), in other words, an average value can be used and it is representative of this physical property of this specimen. In this case, an average value for the specific heats in this range between these temperatures yields a value of $c_p = 1{,}761\,\mathrm{kJ\,kg^{-1}\,K^{-1}}$, whereas from the scientific literature, for three different pine needle species share similar values. *Pinus strobus* regarded as white pine has a specific heat of $2{,}090\,\mathrm{kJ\,kg^{-1}\,K^{-1}}$, *Pinus resinosa* known as red pine has $1{,}702\,\mathrm{kJ\,kg^{-1}\,K^{-1}}$, and pitch pine *Pinus rigida* with $2{,}069\,\mathrm{kJ\,kg^{-1}\,K^{-1}}$ (from Thomas et al., 2017, partially based from an unpublished WPI report).

With the now known behavior of heat capacity, solving for the thermal conductivity k in the aforementioned thermal inertia equation only requires determining the value of E with the straight forward calculation of the bulk density of the pine needle sample used in this experiment. Therefore, both experimental and model temperatures were obtained with the MatLab code so that the semi-infinite medium and the residue can be determined accurately. The results of the thermal model and experimental temperatures from a rise of ambient temperature from 20 °C are shown with its residue in the next figure:

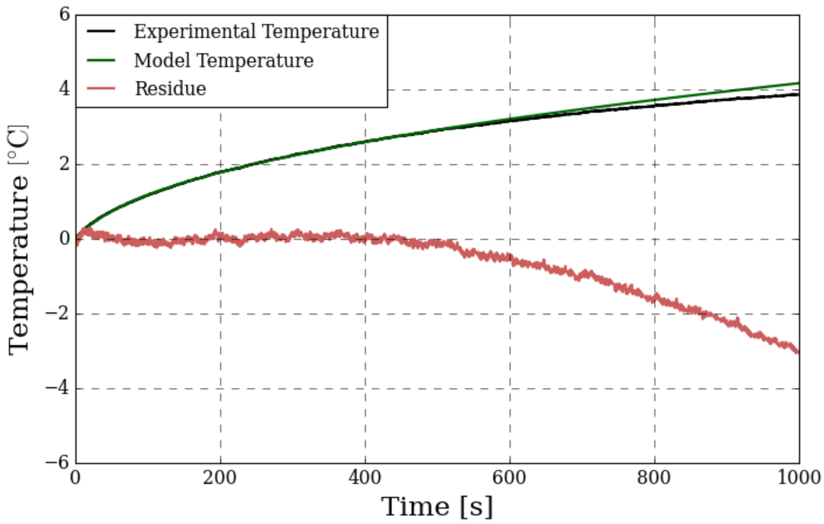

Figure 4.17: Thermal inertia result, experimental and model temperatures, and residue.

The thermal inertia experiment successfully confirmed that the semi-infinite medium condition held adequately for 500 seconds in this case, indicating that the heat exchange between the pine needles and the ambient environment was determined with high precision up to a rise of 4 °C. This resulted in a measured thermal inertia value of $\sqrt{k\rho_b c_p} = 88{,}11 \pm 0{,}84\,\mathrm{W\,K^{-1}\,m^{-2}\,s^{1/2}}$.

This result makes physical sense, since measured values with the same method for similar vegetal porous materials yielded values in the range of $31 - 145\,\mathrm{W\,K^{-1}\,m^{-2}\,s^{1/2}}$ (Damfeu et al., 2016). Hence, the only remaining parameter needed to compute the thermal conductivity is the bulk density of the sample used, which was $\rho_b = 67{,}240\,\mathrm{kg\,m^{-3}}$. With all variables known except for the conductivity, the thermal inertia equation is rearranged to solve for k, this is the following simple rearrangement:

$$k = \frac{E^2}{\rho_b c_p} \tag{4.4}$$

With this in consideration, then a conductivity value for the given context (i.e., the ability of pine needles to exchange heat with the surrounding ambient temperature, with a rise of just 4 degrees Celsius throughout the experiment), then the heat conduction is determined at $0{,}074\,\mathrm{W\,m^{-1}\,K^{-1}}$. Known values with published data show that for different wood specimens the conductivity is $0{,}105\,\mathrm{W\,m^{-1}\,K^{-1}}$ for wood from *Pinus sylvestris* (Reszka and Torero, 2008), $0{,}119\,\mathrm{W\,m^{-1}\,K^{-1}}$ in wood of *Erica arborea* (Tihay et al., 2009), meanwhile for more common species such as oak and maple woods it is $0{,}16\,\mathrm{W\,m^{-1}\,K^{-1}}$ (Incropera et al., 1996). For ten different Mediterranean wood species, the transversal conductivity of these wood samples were in the range of $0{,}07 - 0{,}21\,\mathrm{W\,m^{-1}\,K^{-1}}$ (Flity, 2023). Conversely, it should be expected that for pine needle fuel beds their thermal conductivity should be evidently smaller due to the higher porosity which supports a more insulating behavior due to this different solid matrix containing air in its pores. Accordingly, for four different fiber vegetal materials, conductivities resulted in the range of $0{,}04 - 0{,}09\,\mathrm{W\,m^{-1}\,K^{-1}}$ for the corresponding models used to estimate these values (Damfeu et al., 2016).

With this analysis, the specific heat and thermal conductivity of Pinus radiata were determined, yielding values consistent with physical expectations. The results highlight the importance of considering thermal inertia when analyzing these two properties simultaneously, as it strongly influences the overall thermal response of Pinus radiata. The thermal model employed provided a reliable framework for interpreting the experimental observations.

4.5 One Dimensional Temperature Profile Results

Data processing utilized over the heat fluxes towards the insulated box holding the pine needle samples was carried out over the designated time interval for the low heat flux condition of $4\,\mathrm{kW\,m^{-2}}$ across the three repetitions. Data acquisition from the first experiment under this flux, over a period of two and a half hours, revealed the trend illustrated in Figure 4.18, where a transient phase occurred during the initial stage of the test. As radiation penetrated deeper into the sample, reaching the lowest thermocouple positioned at a depth of 50 mm, the transient behavior became increasingly difficult to observe (note that these depths refer to all depths established in Figure 3.17a).

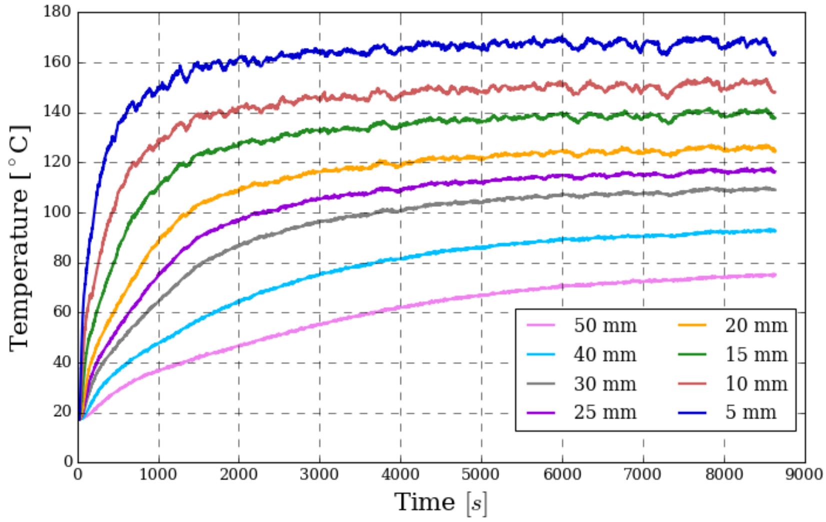

Figure 4.18: Cone calorimeter effect on temperature evolution, experiment one.

Moreover, very good repeatability was observed in the following two experiments, showing consistent trends with only slight deviations due to ambient fluctuations and induced destabilization. Nevertheless, the overall behavior across all acquisitions is notably stable, exhibiting minimal fluctuation as Figures 4.19 and 4.20 reveal. In this context, it is logical to define a one-dimensional analysis of the temperature profile that does not account for the time variable, focusing solely on position, in this case, depth. This approach is particularly suitable here, as the transient and stationary state phases allows for a straightforward evaluation of the influence of vertical distance on radiative penetration. For this model, transient behavior is defined in the first 3000 seconds, whereas the steady state segment of radiative heat transfer from the cone to the box corresponds to the time interval for the three experiments beyond the mentioned time, but more accurately of

Time = [7000, 9000] seconds for all eight thermocouples.

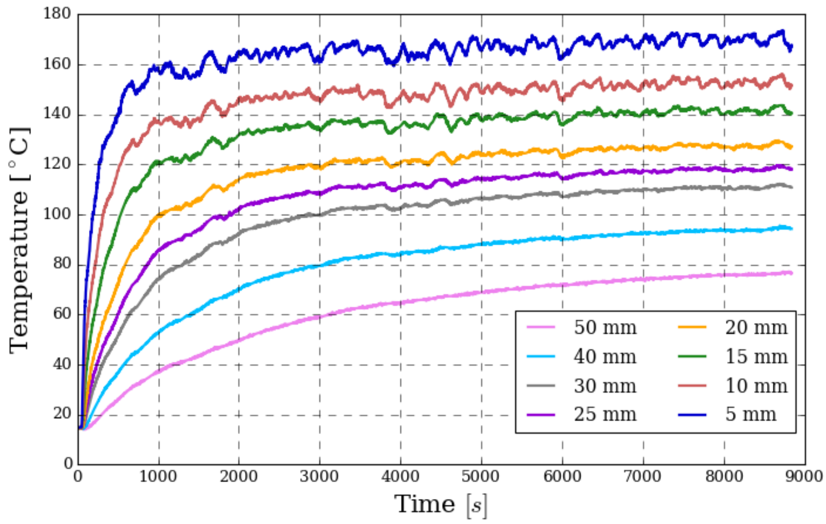

Figure 4.19: Cone calorimeter effect on temperature evolution, experiment two.

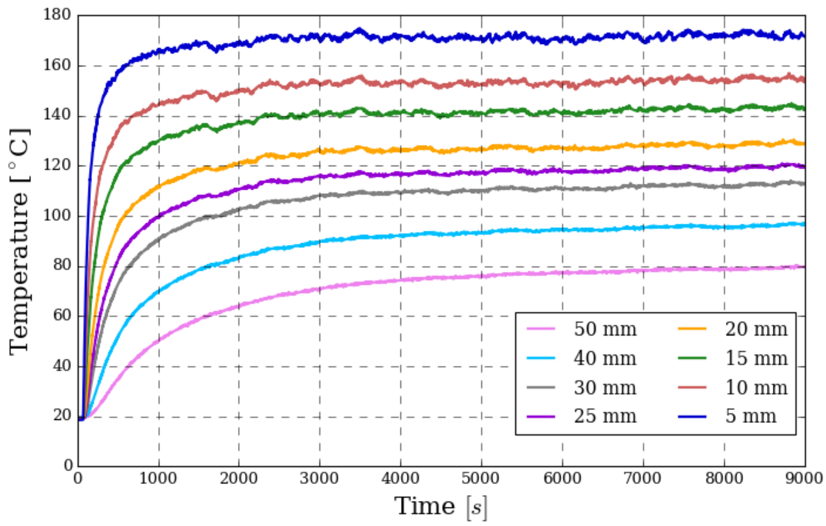

Figure 4.20: Cone calorimeter effect on temperature evolution, experiment three.

All three previous plots exhibit similar trends in how temperature fluctuates compared to wood samples tested under the same setup and heat flux of $4\,\mathrm{kW\,m^{-2}}$, except for the innermost thermocouples, likely due to porosity differences with pine needle fuel beds (Flity et al., 2025). Subsequently, the temperature distribution with respect to the specific depth for each thermocouple is shown for each state. Firstly, for the transient state of the temperature distribution for the first 1000 seconds in Figure 4.21, and in Figure 4.22 the steady state is established for all thermocouples in the last 2000 seconds with negligible variability between all three experiments

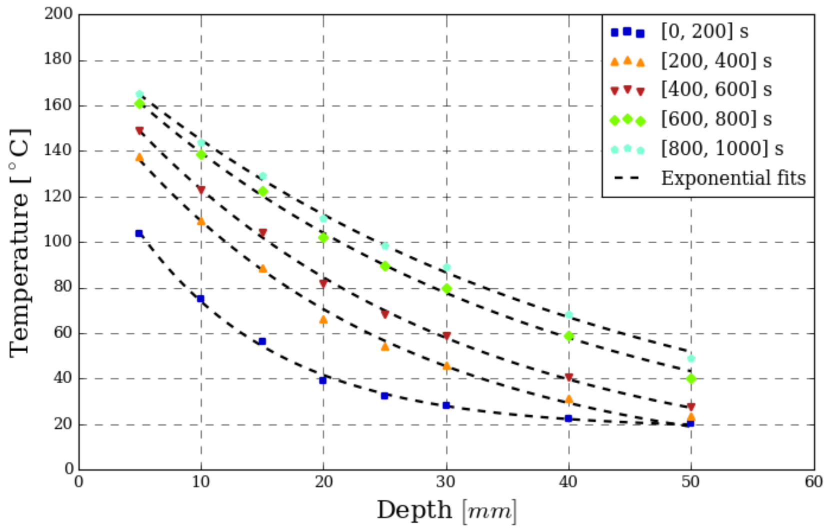

Figure 4.21: Transient state temperature distribution with respect to depth for five different time intervals in the first 1000 seconds.

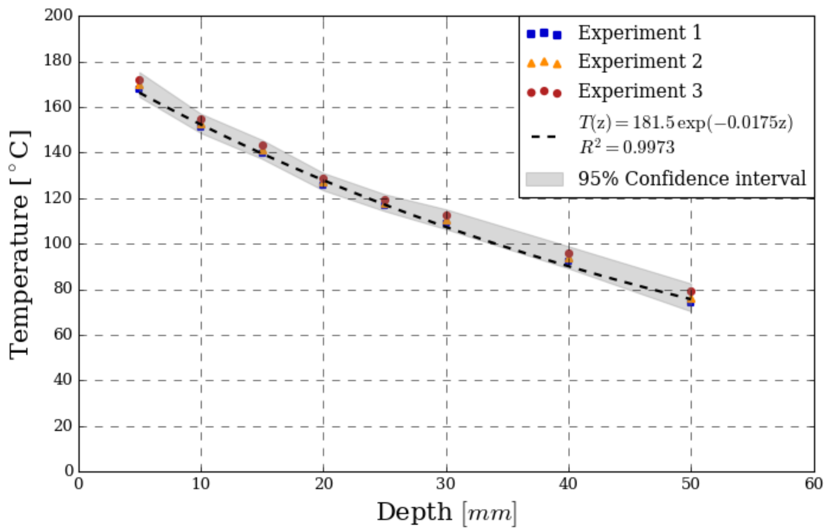

Figure 4.22: Steady state temperature distribution with respect to depth for the last 2000 seconds with t-distribution associated.

This filtered data compounds a clearer understanding of how temperature decreases with respect to vertical in-depth distance. In this way, for the first state the temperature distribution shifts upwards since the closer thermocouples to the cone calorimeter heat up quickly whereas for the last thermocouples is a more moderate change. For steady state, an average for each depth was calculated and a confidence interval determined for this behavior. By defining a 95% confidence interval and by following the simple t-distribution or Student's law, then the more detailed temperature distribution from Figure 4.22 with this statistical filter represents no more fluctuations. This is directly calculated by using Python's library "scipy.stats" and obtaining this t-distribution for this analysis. With this, the now visible threshold for this defined interval with respect to the average reveals with more specificity how clearly the temperature decreases for all thermocouples after more than two hours of the beginning of the experiment.

With regard to the data processing for the high heat flux case of 40 kW m^{-2}, where pyrolysis and ignition occurred, reveals a markedly different temperature evolution compared to the low heat flux experiment. This ignition experiment was conducted over a significantly shorter period of time due to the material being consumed by the fire, and the thermal and radiation penetration to the sample fluctuated considerably as the material suffered degradation of the pine needle sample. Figure 4.23 shows the temperature evolution within the sample with respect to time for the flammability test with the cone calorimeter.

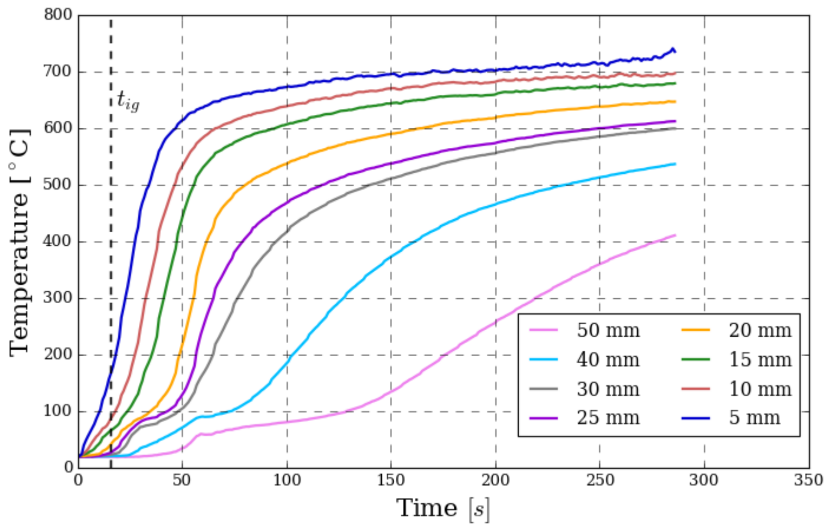

Figure 4.23: Temperature evolution for flammability test.

Ignition was visually identified while executing the experiment exactly at

$t_{ig} = 16$ seconds after the setup was exposed to the intense radiant heat flux of the cone, at a temperature of ignition of $T_{ig} = 168\,°C$. As seen in the figure, the ignition leads to a sharp temperature rise across all thermocouples, especially near the surface at 5 mm, where values exceed 700 °C towards the end of the experiment. This behavior evidently contrasts with the smoother and slower increase observed in the low heat flux case. Additionally, the temperature fluctuations after ignition, most notable at shallower depths, are associated with combustion instabilities and the heterogeneous degradation of the porous fuel bed occurring during the experiment. Deeper regions exhibit a delayed and damped thermal response due to slower heat propagation and shielding from the flame front.

Lastly, in the flammability experiment, the Mass Loss Rate (MLR) was analyzed to assess the degradation behaviour of the pine needle sample during combustion. The MLR was determined by computing the time derivative of the mass signal, measured by the load cell positioned beneath the sample holder. This method captures the instantaneous rate at which mass is lost due to pyrolysis, combustion, and char oxidation processes.

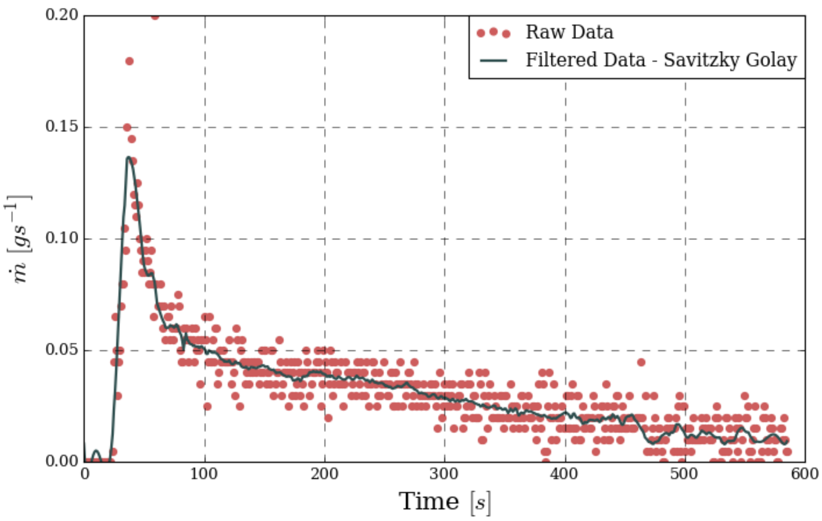

Figure 4.24: MLR evolution for flammability test.

As shown in Figure 4.24, the MLR reaches a sharp peak shortly after ignition, indicating intense devolatilization and burning of the volatile components. This is followed by a progressive decline as the available fuel decreases and the combustion front penetrates deeper into the porous matrix. The long tail in the curve suggests sustained smoldering or slow char consumption beyond the flaming phase.

4.5.1 Fuel Properties: Transient State

From the previous one dimensional analysis, information can be retrieved to complement de thermal analysis from thermal inertia. Hence, two states of the problem can be studied, transient state where heat changes are variant with respect to time and steady state for a linear temperature distribution. Transient state from the ignition experiment can reveal important information based on the heat equation that can be applied to this scenario. As it was done in the previous section, if the problem is considered in one dimension, then this simplification allows for applicable theory for this kind of problem based on radiant heat, t_{ig} and T_{ig}. Therefore, if the one dimensional heat transfer scenario is represented by Equation 2.14. Then, assuming a the same semi-infinite model, an inert material until pyrolysis, this implies a convenient elimination of reactive and convective terms in the differential equation. The governing equation without convection and radiation is then given in the following form (Long et al., 1999; Quintiere, 1974; Reszka and Torero, 2016):

$$(\rho c_p)\frac{\partial T}{\partial t} = k\frac{\partial^2 T}{\partial z^2} \quad \text{Boundary conditions :} \tag{4.5}$$

$$z = 0, \quad -k\frac{\partial T}{\partial z} = \dot{q}''_{rad}(0,t)$$

$$t = 0 \text{ and } z = \infty, \quad T = T_\infty$$

Where conductivity, density and specific heat capacity are represented here as global properties that are representative of the entire heating period. Thereafter, the solution to Equation 4.5 for the temperature distribution in the porous sample as a function of location z and time, the final solution is in the form of:

$$\frac{1}{\sqrt{t_{ig}}} = \frac{2}{\sqrt{\pi}}\frac{\dot{q}''_{rad}}{\sqrt{k\rho c_p}(T_{ig} - T_\infty)} \tag{4.6}$$

As it can be seen, thermal inertia is explicitly present in Equation 4.6, meaning that by knowing the rest of the data, the term $k\rho c_p$ for this ignition scenario can be determined. Before determining this value, an important distinction is made, since there is a dichotomy between fast and long ignition times. For the present case, fast ignition is what occurred, this means that by obtaining a small value for t_{ig} under a high heat flux, the obtained values will be independent of the environmental conditions (Long et al., 1999).

Subsequently, utilizing the known data for the aforementioned equation, ignition time and temperature were 16 seconds and 168 °C respectively, a radiant heat flux of 40.000 $\mathrm{W\,m^{-2}}$, and an ambient temperature of 20 °C. These values for Equation 4.6 indicate that thermal inertia is retrieved as $\sqrt{k\rho c_p} = 428{,}84\,\mathrm{W\,K^{-1}\,m^{-2}\,s^{1/2}}$.

Table 4.10: Thermal inertia comparison from two different approaches and scenarios for *Pinus radiata*.

Approach	$E = \sqrt{k\rho c_p}$ **(W K^{-1} m^{-2} s$^{1/2}$)**
Thermal inertia model	88,11
Ignition energy equation	428,84

As it can be seen in Table 4.10, the comparison between the two values, one for a stable semi-infinite model for small heating intervals (i.e. thermal inertia model) and the other for ignition and pyrolysis, the second value is 4,87 times higher.

4.5.2 Fuel Properties: Steady State

Following the previous analysis, an important examination can be made now with steady state heat transfer for the same problem. Conversely, now for steady state, this implies that the change temperature with respect to time is constant, $\partial T/\partial t = 0$, reducing the energy Equation 2.14 without convection to the following:

$$0 = k\frac{\partial^2 T}{\partial z^2} + \frac{\partial \dot{q}''_{rad}}{\partial z} \tag{4.7}$$

With this equation describing the steady state, there is no need to solve mathematically the temperature distribution, since this function was found experimentally as Figure 4.22 suggests, where the agreement is almost exact with $R^2 = 0{,}9973$. This function is in millimeters, but for meters it is quite simply $T(z) = 181{,}5\exp(-17{,}5z)$.

Now, the divergence of the radiative heat flux is required to solve Equation 2.14 and 4.7, where, then again, for one dimension it is the rate of change with respect to in-depth distance. Therefore, with the Schuster-Schwarzschild approximation, radiation can be split into two directions (i.e. towards and outwards the porous medium) and neglecting reradiation, the RTE yields the incident radiative heat flux coupled with an exponential decay (Mindykowski et al., 2011; Parot et al., 2022) in the form of (note, here σ refers to Stefan-Boltzmann constant):

$$\frac{\partial \dot{q}''_{rad}}{\partial z} \sim \frac{\partial((\dot{q}''_{rad} - \sigma T^4)\,e^{-2\kappa z})}{\partial z} \tag{4.8}$$

While the experimental temperature distribution is now known, the temperature distribution from the mathematical solution stemmed from Equation 4.7 coupled with the approximation of the divergence of the radiative heat flux can also be obtained. This results in the temperature distribution with $R^2 = 0{,}9988$ as follows:

$$T(z) = 155{,}2 - 1515 \cdot z + 40{,}76 \cdot \exp(-109z) \tag{4.9}$$

With the last equation and approximation, where the exponential decay of Equation 4.8 can be assumed in the same form as in Equation 4.9 (i.e., e^{-109z}), serve for understanding and interpreting this exponential decay for the absorption coefficient with in-depth distance z. Hence, κ results in $54{,}5\,\mathrm{m}^{-1}$, when compared to the value obtained experimentally, it is double the value measured.

Table 4.11: Absorption coefficients comparison from two different approaches and scenarios for *Pinus radiata*.

Approach	**κ ($\mathbf{m^{-1}}$)**
Absorption Coefficient Setup	24,9
Steady state energy equation	54,5

Chapter 5

Conclusions

The presented study provided an experimental and analytical investigation of fluid mechanics and heat transfer transfer in natural porous media composed of *Pinus radiata* pine needle fuel beds and two different elongated wood element fuel beds. The study combined controlled laboratory experiments with theoretical modeling to determine the appropriate characterization of the thermophysical properties governing the aforementioned transport processes in these fuel beds. The findings suggest that these methodologies used in this research yielded plausible results for the aim of understanding how these specimens in this contexts responded under different physical scenarios, which can be used in diverse studies regarding wildfire science for flame spread experiments, mathematical analysis and computational simulations.

Permeability for pine and wood yielded values that validate known data and provides further insight into the capacity of porous materials to allow the passage of air, where specific values in the order of $10^{-7}\,\mathrm{m}^2$ were attained. Darcy and Forchheimer regimes were demonstrated, where the inertial regime dominated the analysis and the results for permeability, with distinct transitions from one regime to the other and specific pressure drops.

Reflectivity and transmissivity were two fundamental aspects for radiative behavior of pine needles, since naturally highly porous fuel beds indicated the responses for visible to far infrared spectrum to be considerable or negligible depending on which wavelength is it measured. For reflectivity it was shown how the considerable part is visible and near infrared light, where most radiative heat transfer occurs, whereas for transmissivity it decayed rapidly with small increments of thickness of the fuel beds, but with near negligible difference throughout the mentioned spectrum, facilitating the assumption that most transmission of light is nearly flat for direct transmissivity but near flat for diffuse.

In the case of absorption coefficients with respect to the BBL Law and the geometric optics approach, high porosities revealed near perfect adequacy for wood elements, meanwhile for randomly distributed pine needle fuel beds it diverges rapidly. Nevertheless, these results provide insight into absorption coefficients that can be used truthfully to represent real scenarios.

For conductivity and specific heats based on thermal inertia yielded values well adjusted to other several pine needles, resulted in parameters that are feasible for porous mediums like the fuel beds studied with pine needles in the order of $0{,}04 - 0{,}09\,\mathrm{W\,m^{-1}\,K^{-1}}$ with a value of $0{,}074\,\mathrm{W\,m^{-1}\,K^{-1}}$ and in the ranges from $1 - 2\,\mathrm{kJ\,kg^{-1}\,K}$ for a heat capacity of $1{,}761\,\mathrm{kJ\,kg^{-1}\,K}$.

Lastly, temperature distributions revealed important information for the heat equation describing the one dimensional phenomena of the scenario, since temperature gradients with respect to depth are known at non pyrolysis context but also for flammability tests. Therefore, through transient ans steady states, validations of experimentally determined physical parameters such as the thermal inertia, the absorption coefficient and the conductivity were obtained.

In synthesis, permeability results reaffirm and allow this parameter for accurate ignition analyses and more profound studies of convective heat transfer as it implicates further characterization of other parameters regarding fluid phase heat transfer; reflectivity, direct and diffuse transmissivity along with absorption coefficients can be used in models such as the Monte Carlo approach or for inverse radiative transfer problems for seeking to solve the RTE; conductivity and specific heat with known temperature gradients and approximations for the divergence of the radiative flux can be used for modeling and attempting the complete solution of the energy equation with the convective heat transfer; the possibility to assess manageable systematic changes in fuel beds with now known properties that directly affect burning rates in ignition experiments; more intricate forms for mathematical modeling such as utilizing Green functions with the available thermophysical data to ascertain ignition delay times.

Bibliography

Acem, Z., Lamorlette, A., Collin, A., & Boulet, P. (2009). Analytical determination and numerical computation of extinction coefficients for vegetation with given leaf distribution. *International Journal of Thermal Sciences*, *48*(8), 1501–1509.

Acem, Z., Parent, G., Monod, B., Jeandel, G., & Boulet, P. (2010). Experimental study in the infrared of the radiative properties of pine needles. *Experimental Thermal and Fluid Science*, *34*(7), 893–899.

Ager, A. A., Evers, C. R., Day, M. A., Alcasena, F., & Houtman, R. (2021). Planning for future fire: Scenario analysis of an accelerated fuel reduction plan for the Western United States. *Landscape and Urban Planning*, *215*, 104212.

Anderson, J. D. (2016). *Introduction to flight* (8th ed.). McGraw-Hill Education.

Baillis, D., & Randrianalisoa, J. (1996). Improved inverse method for radiative characteristics of closed-cell absorbing porous media. *Journal of Heat Transfer*, *118*(1), 79–87.

Bal, H., Jannot, Y., Gaye, S., & Demeurie, F. (2013). Measurement and modelisation of the thermal conductivity of a wet composite porous medium: Laterite based bricks with millet waste additive. *Construction and Building Materials*, *41*, 586–593.

Bal, H., Jannot, Y., Quenette, N., Chenu, A., & Gaye, S. (2012). Water content dependence of the porosity, density and thermal capacity of laterite based bricks with millet waste additive. *Construction and Building Materials*, *31*, 144–150.

Bartoli, P., Simeoni, A., Biteau, H., Torero, J., & Santoni, P. (2011). Determination of the main parameters influencing forest fuel combustion dynamics [Forest Fires]. *Fire Safety Journal*, *46*(1), 27–33.

Bear, J. (2018). *Modeling phenomena of flow and transport in porous media* (Vol. 31). Cham, Switzerland, Springer.

Beck, J. V., Blackwell, B., & St. Clair Jr., C. R. (1985). *Inverse heat conduction: Ill-posed problems*. Wiley-Interscience.

Bouche, P. S., Delzon, S., Choat, B., Badel, E., Brodribb, T., Burlett, R., Cochard, H., Charra-Vaskou, K., Lavigne, B., Li, S., Mayr, S., Morris, H., Torres-Ruiz, J. M., Zufferey, V., & Jansen, S. (2015). Are needles of Pinus pinaster more vulnerable to xylem embolism than branches? new insights from x-ray computed tomography. *Plant, Cell & Environment*, *39*.

Brace, W., Walsh, J., & Frangos, W. (1968). Permeability of granite under high pressure. *Journal of Geophysical Research*, *73*(6), 2225–2236.

Committee on Fire Research. (1961). *A study of fire problems* (Technical Report). U.S. National Academy of Sciences.

Damfeu, J., Meukam, P., & Jannot, Y. (2016). Modeling and measuring of the thermal properties of insulating vegetable fibers by the asymmetrical hot plate method and the radial flux method: Kapok, coconut, groundnut shell fiber and rattan. *Thermochimica Acta*, *630*, 64–77.

Darcy, H. (1856). Les fontaines publiques de la ville de dijon: Distribution d'eau et filtrage des eaux. *Victor Dalmont, Paris*.

de Mestre, N. J., Catchpole, E. A., Anderson, D. H., & Rothermel, R. C. (1989). Uniform propagation of a planar fire front without wind. *Combustion Science and Technology*, *65*, 231–244.

Di Virgilio, G., Evans, J. P., Blake, S. A. P., Armstrong, M., Dowdy, A. J., Sharples, J., & McRae, R. (2019). Climate change increases the potential for extreme wildfires. *Geophysical Research Letters*.

Dombrovsky, L., Henry, J. F., Lorreyte, C., Pron, H., & Randrianalisoa, J. (2018). Optical properties of oakwood in the near-infrared range of semi-transparency. *Appl. Opt.*, *57*(23), 6657–6663.

Egermann, P., Lenormand, R., Longeron, D., & Zarcone, C. (2003). A fast and direct method of permeability measurement on drill cuttings. *Petrophysics*, *44*(4), 243–252.

Ergun, S. (1952). Fluid flow through packed columns. *Chemical Engineering Progress*, *48*(2), 89–94.

Fehrmann, S., Jahn, W., & Rivera, J. d. D. (2017). Permeability comparison of natural and artificial *Pinus Radiata* forest litters. *Fire Technology*, *53*, 1291–1308.

Fernandes, P. M., & Rego, F. C. (1998). A new method to estimate fuel surface area-to-volume ratio using water immersion. *International Journal of Wildland Fire*, *8*(2), 59–66.

Fernandez-Pello, C. (1994). The solid phase. In G. Cox (Ed.), *Combustion fundamentals of fire* (pp. 31–100). Academic Press Limited.

Finney, M. A., McAllister, S. S., Grumstrup, T. P., & Forthofer, J. M. (2021). *Wildland fire behaviour*. CSIRO.

Flity, H. (2023). *Modélisation de la dégradation et combustion du bois de construction* (Ph.D. thesis). Université de Lorraine.

Flity, H., Terrei, L., Acem, Z., & Parent, G. (2025). Study of heat transfer in wood before the onset of pyrolysis at the cone calorimeter scale. *International Journal of Thermal Sciences*, *210*, 109545.

Fu, K., & Hsu, P. F. (2008). New regime map of the geometric optics approximation for scattering from random rough surfaces. *Journal of Quantitative Spectroscopy and Radiative Transfer*, *109*(2), 180–188.

Green, L. J., & Duwez, P. (1951). Fluid flow through porous metals. *Journal of Applied Mechanics*, 39–45.

Grishin, A. M. (1997). *Mathematical modeling of forest fires and new methods for fighting them*. Tomsk, Russia, Publishing House of Tomsk University.

Hendricks, T. J., & Howell, J. R. (2006). Absorption/scattering coefficients and scattering phase functions in reticulated porous ceramics. *Journal of Thermophysics and Heat Transfer*, *20*(4), 871–883.

Hernández, N., Fuentes, A., Reszka, P., & Fernández-Pello, A. (2019). Piloted ignition delay times on optically thin PMMA cylinders. *Proceedings of the Combustion Institute*, *37*(3), 3993–4000.

Hottel, H. C. (1954). Radiant-heat transmission, In *Heat transmission*. McGraw-Hill Series in Chemical Engineering.

Hottel, H. C., & Sarofim, A. F. (1967). Radiant transfer in an absorbing-scattering medium, In *Radiative transfer*. McGraw-Hill Book Company.

Howell, J. R., Mengüç, M. P., & Siegel, R. (2015). *Thermal radiation heat transfer* (6th). Boca Raton, FL, CRC Press.

Huang, Z., Yao, J., Li, Y., Wang, C., & Lv, X. (2011). Numerical calculation of equivalent permeability tensor for fractured vuggy porous media based on homogenization theory. *Communications in Computational Physics*, *9*(1), 180–204.

IAFSS. (2023). *History of IAFSS*. https://iafss.org/history/

Incropera, F. P., DeWitt, D. P., Bergman, T. L., Lavine, A. S., Et al. (1996). *Fundamentals of heat and mass transfer* (Vol. 6). Wiley New York.

Jain, A. (2023). The role of thermal effusivity in heat exchange between finite-sized bodies. *International Journal of Heat and Mass Transfer*, *202*, 123721.

Jannot, Y., & Lasseux, D. (2012). A new method to measure gas permeability of weakly permeable porous media. *Review of Scientific Instruments*, *83*(1), 015113.

Jannot, Y., Lasseux, D., Vizé, G., & Hamon, G. (2007). A detailed analysis of permeability and klinkenberg coefficient estimation from unsteady-state pulse-decay or draw-down experiments, In *Proceedings of the sca international symposium*, Calgary, Canada. Society of Core Analysts.

Jannot, Y., Zoubir, A., & Kanmogne, A. (2005). Transient hot plate method with two temperature measurements for thermal characterization of metals. *Measurement Science and Technology*, *17*, 69.

Kaviany, M. (1995). *Principles of heat transfer in porous media*. Springer-Verlag.

Koebel, M., Rigacci, A., & Achard, P. (2012). Aerogel-based thermal superinsulation: An overview. *Journal of Sol-Gel Science and Technology*, *63*, 315–339.

Lai, W. M., Rubin, D., & Krempl, E. (2010). The reynolds transport theorem and applications, In *Introduction to continuum mechanics (fourth edition)*. Butterworth-Heinemann.

Leal, L. G. (2007). *Advanced transport phenomena: Fluid mechanics and convective transport processes*. Cambridge, Cambridge University Press.

Liu, I.-S. (1990). On Fourier's law of heat conduction. *Continuum mechanics and Thermodynamics*, *2*, 301–305.

Liu, P., & Chen, G. (2014). Chapter one - general introduction to porous materials (P. Liu & G. Chen, Eds.). In P. Liu & G. Chen (Eds.), *Porous materials*. Boston, Butterworth-Heinemann.

Long, R. T., Torero, J. L., Quintiere, J. G., & Fernandez-Pello, A. C. (1999). Considerations on piloted ignition of PMMA. *Fire Safety Science*, *6*, 567–578.

Macini, P., Mesini, E., & Viola, R. (2011). Laboratory measurements of non-darcy flow coefficients in natural and artificial unconsolidated porous media. *Journal of Petroleum Science and Engineering*, *77*(3-4), 365–374.

Mayerhöfer, T. G., Pahlow, S., & Popp, J. (2020). The bouguer-beer-lambert law: Shining light on the obscure. *ChemPhysChem*, *21*(18), 2029–2046.

McNamee, M. (2019). IAFSS agenda 2030 for a fire safe world. *Fire Safety Journal*, *110*, 102889.

Mindykowski, P., Fuentes, A., Consalvi, J., & Porterie, B. (2011). Piloted ignition of wildland fuels. *Fire Safety Journal*, *46*(1), 34–40.

Modest, M., & Mazumder, S. (2022). *Radiative heat transfer* (4th ed.). Academic Press.

Monod, B., Collin, A., Parent, G., & Boulet, P. (2009). Infrared radiative properties of vegetation involved in forest fires. *Fire Safety Journal*, *44*(1), 88–95.

Moritz, M. A. (2014). Learning to coexist with wildfire. *Nature*, *515*, 58–66.

Mueller, E. V., Gallagher, M. R., Skowronski, N., & Hadden, R. M. (2021). Approaches to modeling bed drag in pine forest litter for wildland fire applications. *Transport in Porous Media*, *138*(3), 637–660.

Nealson, K. H., & Conrad, P. G. (1999). Life: Past, present and future. *Philosophical Transactions of the Royal Society B: Biological Sciences*, *354*(1392), 1923–1939.

Nield, D. A., & Bejan, A. (2013). *Convection in porous media*. Springer.

Niioka, T., Takahashi, M., & Izumikawa, M. (1981). Gas-phase ignition of a solid fuel in a hot stagnation-point flow, In *Eighteenth symposium (international) on combustion*, The Combustion Institute.

Nolan, R. H., Blackman, C. J., Resco de Dios, V., Brendan, C., Medlyn, B. E., Li, X., Bradstock, R. A., & Boer, M. M. (2020). Linking forest flammability and plant vulnerability to drought, In *Forests*.

Özisik, M. N. (1973). *Radiative transfer and interactions with conduction and convection*. Wiley-Interscience.

Parot, R., Rivera, J. I., Reszka, P., Torero, J. L., & Fuentes, A. (2022). A simplified analytical model for radiation dominated ignition of solid fuels exposed to multiple non-steady heat fluxes. *Combustion and Flame*, *237*, 111866.

Pessoa, L. (2019). *Experimental investigation of the influence of bulk properties on the ignition of surrogate porous fuel beds* (Master's thesis). Universidad Adolfo Ibáñez.

Peters, B., & Raupenstrauch, H. (2010). Modeling moving and fixed bed combustion, In *Handbook of combustion, vol. 4: Solid fuels*. Wiley-VCH Verlag GmbH & Co.

Pinto, P., Valdivia, J., Singh, A., Xi, X., Cuevas, J., & Urban, J. (2025). Investigating radiation heat transfer from the cone calorimeter heater: A new view factor model and uncertainty quantification. *International Journal of Heat and Mass Transfer*, *245*, 126976.

Prichard, S. J., Hessburg, P. F., Hagmann, R. K., Povak, N. A., Dobrowski, S. Z., Hurteau, M. D., Kane, V. R., Keane, R. E., Kobziar, L. N., Kolden, C. A., North, M., Parks, S. A., Safford, H. D., Stevens, J. T., Yocom, L. L., Churchill, D. J., Gray, R. W., Huffman, D. W., Lake, F. K., & Khatri-Chhetri, P. (2021). Adapting Western North American forests to climate change and wildfires: 10 common questions. *Ecological Applications*, *31*(8).

Qiu, J., Khalloufi, S., Martynenko, A., Van Dalen, G., Schutyser, M., & Almeida-Rivera, C. (2015). Porosity, bulk density, and volume reduction during drying: Review of measurement methods and coefficient determinations. *Drying Technology*, *33*(14), 1681–1699.

Quintiere, J. G. (1974). Theory for generalizing results from a radiant panel flame spread apparatus. *Journal of Fire and Materials*, *5*, 85.

Reszka, P., & Torero, J. L. (2016). Fire behavior of timber and lignocellulose. *Lignocellulosic Fibers and Wood Handbook*, 553–581.

Reszka, P., & Torero, J. (2008). In-depth temperature measurements in wood exposed to intense radiant energy. *Experimental Thermal and Fluid Science*, *32*(7), 1405–1411.

Rothermel, R. (1972). *A mathematical model for predicting fire spread in wildland fuels* (Research Paper INT-115). USDA Forest Service.

Santoni, P. A., Bartoli, P., Simeoni, A., & Torero, J. L. (2014). Bulk and particle properties of pine needle fuel beds-influence on combustion. *International Journal of Wildland Fire*, *23*(8), 1076–1086.

Scheidegger, A. (1974). *The physics of flow through porous media* (Third Edition). Toronto, University of Toronto Press.

Simeoni, A., Thomas, J., Bartoli, P., Borowieck, P., Reszka, P., Colella, F., Santoni, P., & Torero, J. (2012). Flammability studies for wildland

and wildland–urban interface fires applied to pine needles and solid polymers. *Fire Safety Journal*, *54*, 203–217.

Staggs, J. (2005). Savitzky–golay smoothing and numerical differentiation of cone calorimeter mass data. *Fire Safety Journal*, *40*(6), 493–505.

Tang, K., Dimenna, R. A., & Buckius, R. O. (1996). Regions of validity of the geometric optics approximation for angular scattering from very rough surfaces. *International Journal of Heat and Mass Transfer*, *40*(1), 49–59.

Thomas, J. C. (2017). *Improving the understanding of fundamental mechanisms that influence ignition and burning behavior of porous wildland fuel beds* (Doctoral dissertation) [PQDT - UK & Ireland]. The University of Edinburgh. PQDT - UK & Ireland.

Thomas, J. C., Hadden, R. M., & Simeoni, A. (2017). Experimental investigation of the impact of oxygen flux on the burning dynamics of forest fuel beds. *Fire Safety Journal*, *91*, 855–863.

Tihay, V., Simeoni, A., Santoni, P.-A., Rossi, L., Garo, J.-P., & Vantelon, J.-P. (2009). Experimental study of laminar flames obtained by the homogenization of three forest fuels. *International Journal of Thermal Sciences*, *48*(3), 488–501.

Torero, J. L. (2016). Flaming ignition of solid fuels (M. J. Hurley Et al., Eds.; Fifth). In M. J. Hurley Et al. (Eds.), *SFPE handbook of fire protection engineering* (Fifth). Springer New York.

Torero, J. L., & Simeoni, A. (2010). Heat and mass transfer in fires: Scaling laws, ignition of solid fuels and application to forest fires. *The Open Thermodynamics Journal*, *4*, 145–155.

Vadasz, P. (2005). Explicit conditions for local thermal equilibrium in porous media heat conduction. *Transport Porous Media*, *59*, 341–355.

Vaz, G. C., André, J. C. S., & Viegas, D. X. (2004). Estimation of the radiation extinction coefficient of natural fuel beds. *International Journal of Wildland Fire*, *13*, 65–71.

Walker, X. J., Rogers, B. M., Veraverbeke, S., & et al. (2020). Fuel availability not fire weather controls boreal wildfire severity and carbon emissions. *Nature Climate Change*, *10*, 1130–1136.

Wang, S., Dai, G., Yang, H., & Luo, Z. (2017). Lignocellulosic biomass pyrolysis mechanism: A state-of-the-art review. *Progress in Energy and Combustion Science*, *62*, 33–86.

Wang, Y., & Knabe, R. (2010). Permeability characterization on tight gas samples using pore pressure oscillation method, In *Proceedings of the sca international symposium*, Halifax, Nova Scotia, Canada. Society of Core Analysts.

Whitaker, S. (1996). The forchheimer equation: A theoretical development. *Transport in Porous media*, *25*(1), 27–61.

White, F. M. (2016). *Fluid mechanics* (8th ed.). McGraw-Hill Education.

Yang, Y., Ryu, C., Khora, A., Yates, N., Sharifi, V., & Swithenbank, J. (2005). Effect of fuel properties on biomass combustion. part ii. modelling approach—identification of the controlling factors. *Fuel*, *84*, 2116–2130.

Yu, X., & Williams, C. T. (2022). Recent advances in the applications of mesoporous silica in heterogeneous catalysis. *Catalysis Science Technology*, *12*(19), 5765–5794.

Zeng, Z., & Grigg, R. (2006). A criterion for non-Darcy flow in porous media. *Transport in Porous Media*, *63*(1), 57–69.

Zhang, X. W., & Liu, W. (2008). New criterion for local thermal equilibrium in porous media. *Thermophysics and Heat Transfer*, *22*, 649–653.

Appendix A

Cross-Section Images and Analysis Code

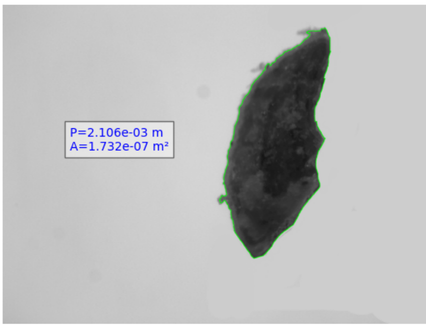

(a) Sample two.

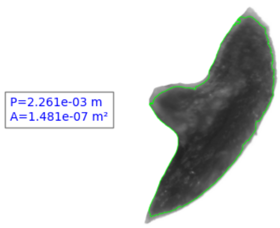

(b) Sample three.

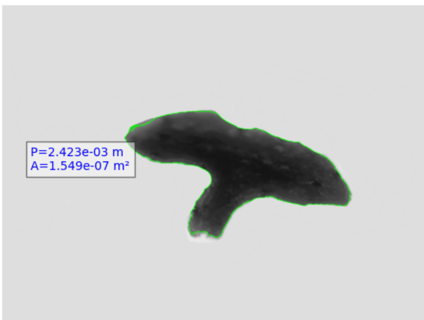

(c) Sample four.

Figure A.1: All images of the analysis for SVR ratio for dead and dry pine needles of *Pinus radiata*.

```python
import cv2 #For pattern recognition analysis
import matplotlib.pyplot as plt
import numpy as np

#Scale
#microns/px a 40x
microns_per_pixel = 0.7

#Conversion cm to m
cm_per_pixel = microns_per_pixel * 1e-4   #(1 micron
    = 1e-4 cm)
m_per_pixel  = microns_per_pixel * 1e-6   #(1 micron
    = 1e-6 m)

#Gray scales for reading image
im = cv2.imread('image4.png', cv2.IMREAD_GRAYSCALE)

#Binarization of image
bw = (im < 128).astype('uint8')

#Find contours
contours, _ = cv2.findContours(bw, cv2.RETR_EXTERNAL,
     cv2.CHAIN_APPROX_SIMPLE)

#Use correct contour (assuming only one geometry in
    the image (no differentiation in the code))
contour = max(contours, key=cv2.contourArea)

#Perimeter in pixels
perimetro_px = cv2.arcLength(contour, True)
perimetro_cm = perimetro_px * cm_per_pixel
perimetro_m  = perimetro_px * m_per_pixel

#Area in pixels
area_px = cv2.contourArea(contour)
area_cm2 = area_px * (cm_per_pixel**2)
area_m2  = area_px * (m_per_pixel**2)

#Colors
im_color = cv2.cvtColor(im, cv2.COLOR_GRAY2BGR)
cv2.drawContours(im_color, [contour], -1, (0, 255, 0)
    , 2)

#Centroid
```

```python
M = cv2.moments(contour)
cX = int(M["m10"] / M["m00"])
cY = int(M["m01"] / M["m00"])

#Results
plt.imshow(im_color)
plt.text(cX-1000, cY+20,
         f"P={perimetro_m:.3e} m\nA={area_m2:.3e} m^2",
         color='blue', fontsize=10, bbox=dict(facecolor='white', alpha=0.5))
plt.axis('off')
plt.show()
print("Results:")
print(f"Perimeter = {perimetro_cm:.2f} cm  ({perimetro_m:.3e} m)")
print(f"Area = {area_cm2:.4f} cm^2  ({area_m2:.3e} m^2)")
print(perimetro_m/area_m2)
print((4*area_m2)/perimetro_m)
```

Listing A.1: Pattern recognition of area and perimeter of the cross-section image of dry pine needles.